Magnetic Flux-Based Nondestructive Evaluation Technologies for Assessing Corrosion Damage in External and Internal Post-Tensioned Tendons: Development Efforts and Evaluation Results

PUBLICATION NO. FHWA-HRT-23-005

DECEMBER 2022

U.S. Department of Transportation
Federal Highway Administration

Research, Development, and Technology
Turner-Fairbank Highway Research Center
6300 Georgetown Pike
McLean, VA 22101-2296

FOREWORD

This report documents research efforts to develop and validate three types of magnetic flux-based nondestructive evaluation (NDE) technologies for external and internal post-tensioned (PT) tendons.

This study provides bridge program personnel from Federal, State, and local transportation departments with information on the advantages and limitations of magnetic-based NDE technologies. Bridge design engineers, specification writers, consultants, and manufacturers/suppliers of PT tendon-related systems, products, and materials may find this report to be of interest.

Jean A. Nehme, Ph.D., P.E.
Director, Office of Infrastructure
Research and Development

Recommended citation: Federal Highway Administration, *Magnetic Flux-Based Nondestructive Evaluation Technologies for Assessing Corrosion Damage in External and Internal Post-Tensioned Tendons: Development Efforts and Evaluation Results* (Washington, DC: 2022) https://doi.org/10.21949/1521948.

TECHNICAL REPORT DOCUMENTATION PAGE

1. Report No. FHWA-HRT-23-005	2. Government Accession No.	3. Recipient's Catalog No.
4. Title and Subtitle Magnetic Flux-Based Nondestructive Evaluation Technologies for Assessing Corrosion Damage in External and Internal Post-Tensioned Tendons: Development Efforts and Evaluation Results		5. Report Date December 2022 6. Performing Organization Code:
7. Author(s) Seung-Kyoung Lee (ORCID: 0000-0001-7367-5197), Toshiyuki Moriya, Hiroaki Itoi, Masamichi Sugawara, and Hironori Kanemaru		8. Performing Organization Report No.
9. Performing Organization Name and Address SK Lee & Associates, Inc. 10813 Fieldwood Dr. Fairfax, VA 22030 Tokyo Rope Mfg. Co., Ltd. 3-6-2 Nihonbashi, Chuo-Ku, Tokyo 103-8306, Japan		10. Work Unit No. 11. Contract or Grant No. DTFH61-14-D-00011
12. Sponsoring Agency Name and Address Office of Infrastructure Research and Development Turner-Fairbank Highway Research Center Federal Highway Administration 6300 Georgetown Pike McLean, VA 22101-2296		13. Type of Report and Period Covered Final report, September 2008–December 2019 14. Sponsoring Agency Code HRDI-20
15. Supplementary Notes The Technical Contact was Hoda Azari (HRDI-20), and the Contracting Officer's Representative was Cara Fitzgerald (HRDI-1).		

16. Abstract

This report presents research work related to developing and evaluating magnetic flux-based nondestructive evaluation (NDE) technologies for detecting corrosion damage in external and internal post-tensioned (PT) tendons. For the external tendons, two types of magnetic main flux method (MMFM) systems—a solenoid type and a permanent magnet type—were developed and validated in the laboratory and in the field. The solenoid-type MMFM system was the most accurate NDE method. Its lowest damage detection limit would be 0.4-percent section loss for the point measurement method and 1.0-percent section loss for the scan measurement method. The permanent-type MMFM system is suitable for locating potential problem areas containing more than 3.0-percent section loss in external PT tendons. It has more versatile applications in the field because of its simpler hardware and speedy operation. Ideally, both MMFM systems can be employed in sequence during the field investigations: the permanent magnet type identifies potentially problematic areas by quickly scanning all suspected tendons, followed by the point measurements in the suspicious areas with the solenoid type. A return flux method prototype was developed for the internal tendons. It reached the immediate goal of detecting relatively small section losses hidden in internal tendons in laboratory environments and proved its concept successfully. It could detect a section loss larger than 15.3-percent in internal mockup tendons surrounded by vertical rebars at 6.0-inch or wider spacing when the clear concrete cover was less than 7.5 inches for metal ducts and 6.5 inches for polyethylene ducts. Without interference from the vertical rebars, as little as 9.0-percent section loss could be identified at the 6.0-inch cover. However, poor results were obtained in the anchorage zone in the box girder specimen. It is recommended that the present prototype be further improved to make it a field-deployable NDE system.

17. Key Words	18. Distribution Statement
Corrosion, post-tensioned tendon, nondestructive evaluation, grout void, seven-wire strand, magnetic main flux method, return flux method, magnetic flux, magnetic field, section loss, Hall effect sensor	No restrictions. This document is available to the public through the National Technical Information Service, Springfield, VA 22161.

19. Security Classif. (of this report)	20. Security Classif. (of this page)	21. No. of Pages	22. Price
Unclassified	Unclassified	98	N/A

SI* (MODERN METRIC) CONVERSION FACTORS

APPROXIMATE CONVERSIONS TO SI UNITS

Symbol	When You Know	Multiply By	To Find	Symbol
		LENGTH		
in	inches	25.4	millimeters	mm
ft	feet	0.305	meters	m
yd	yards	0.914	meters	m
mi	miles	1.61	kilometers	km
		AREA		
in^2	square inches	645.2	square millimeters	mm^2
ft^2	square feet	0.093	square meters	m^2
yd^2	square yard	0.836	square meters	m^2
ac	acres	0.405	hectares	ha
mi^2	square miles	2.59	square kilometers	km^2
		VOLUME		
fl oz	fluid ounces	29.57	milliliters	mL
gal	gallons	3.785	liters	L
ft^3	cubic feet	0.028	cubic meters	m^3
yd^3	cubic yards	0.765	cubic meters	m^3
	NOTE: volumes greater than 1,000 L shall be shown in m^3			
		MASS		
oz	ounces	28.35	grams	g
lb	pounds	0.454	kilograms	kg
T	short tons (2,000 lb)	0.907	megagrams (or "metric ton")	Mg (or "t")
		TEMPERATURE (exact degrees)		
°F	Fahrenheit	5 (F-32)/9 or (F-32)/1.8	Celsius	°C
		ILLUMINATION		
fc	foot-candles	10.76	lux	lx
fl	foot-Lamberts	3.426	$candela/m^2$	cd/m^2
		FORCE and PRESSURE or STRESS		
lbf	poundforce	4.45	newtons	N
lbf/in^2	poundforce per square inch	6.89	kilopascals	kPa

APPROXIMATE CONVERSIONS FROM SI UNITS

Symbol	When You Know	Multiply By	To Find	Symbol
		LENGTH		
mm	millimeters	0.039	inches	in
m	meters	3.28	feet	ft
m	meters	1.09	yards	yd
km	kilometers	0.621	miles	mi
		AREA		
mm^2	square millimeters	0.0016	square inches	in^2
m^2	square meters	10.764	square feet	ft^2
m^2	square meters	1.195	square yards	yd^2
ha	hectares	2.47	acres	ac
km^2	square kilometers	0.386	square miles	mi^2
		VOLUME		
mL	milliliters	0.034	fluid ounces	fl oz
L	liters	0.264	gallons	gal
m^3	cubic meters	35.314	cubic feet	ft^3
m^3	cubic meters	1.307	cubic yards	yd^3
		MASS		
g	grams	0.035	ounces	oz
kg	kilograms	2.202	pounds	lb
Mg (or "t")	megagrams (or "metric ton")	1.103	short tons (2,000 lb)	T
		TEMPERATURE (exact degrees)		
°C	Celsius	1.8C+32	Fahrenheit	°F
		ILLUMINATION		
lx	lux	0.0929	foot-candles	fc
cd/m^2	candela/m2	0.2919	foot-Lamberts	fl
		FORCE and PRESSURE or STRESS		
N	newtons	2.225	poundforce	lbf
kPa	kilopascals	0.145	poundforce per square inch	lbf/in^2

*SI is the symbol for International System of Units. Appropriate rounding should be made to comply with Section 4 of ASTM E380. (Revised March 2003)

TABLE OF CONTENTS

LIST OF FIGURES

LIST OF TABLES

LIST OF ABBREVIATIONS

Abbreviations

AC	alternating current
AE	acoustic emission
AT	ampere-turn
DC	direct current
EIS	electrochemical impedance spectroscopy
FDOT	Florida Department of Transportation
FHWA	Federal Highway Administration
FIU	Florida International University
GPR	ground penetrating radar
HCP	half-cell potential
HDPE	high-density polyethylene
IE	impact echo
IMFD	induced magnetic field detection
IR	impulse response
IRT	infrared thermography
MFL	magnetic flux leakage
MsS	magnetostrictive sensor
MMFM	magnetic main flux method
NDE	nondestructive evaluation
NDT	nondestructive test
PE	polyethylene
PSC	prestressed concrete
PT	post-tensioned

PVC	polyvinyl chloride
RFM	return flux method
RM	remanent magnetism
TFHRC	Turner-Fairbank Highway Research Center
TRM	Tokyo Rope Manufacturing
SE	sonic echo
USE	ultrasonic echo
VDOT	Virginia Department of Transportation

Measurements

ϕ	magnetic flux
$\Delta\phi$	difference in magnetic flux
H	magnetic field or magnetic flux density
B_s	saturated magnetic field
H_{Gx}	axial Hall effect sensor
H_{Gy}	radial Hall effect sensor

CHAPTER 1. INTRODUCTION

The prestressed concrete (PSC) bridge structures in the United States have incorporated high-strength steel as economic and efficient structural components for more than five decades. The PSC bridge's structural integrity relies on the high-strength prestressing steel, for example, wires, seven-wire strands, and bars that have a smaller cross-sectional area than ordinary reinforcing steel. Post-tensioned (PT) tendons are a good example of their use.

The corrosion-induced section loss of prestressing steel is usually localized and, thus, more critical than the equivalent loss of reinforcing steel. Compounding the situation, the prestressing steel is embedded in concrete and enclosures such as ducts and anchorages. No apparent external signs of structural deficiencies appear until it is too late to intervene, or, at best, the damage level of the highly stressed steel becomes critical.[1] Since 1999, corrosion-induced tendon failures have been reported in the United States. Figure 1 shows photographs of four tendon failure cases.

Figure 1-A shows a corroded anchor head recovered from the Niles Channel Bridge in Florida in 1999. It failed after 13-yr of service. Figure 1-B shows a failed tendon section on the Varina-Enon Bridge in Virginia in 2007. The tendon in question failed prematurely after 17-yr of service due to severe corrosion of 19 0.6-inch seven-wire strands. As a result, the Virginia Department of Transportation (VDOT) replaced the fractured tendon and another one exhibiting severe corrosion. Figure 1-C shows the first failed tendon in the Ringling Causeway Bridge in Florida in January 2011 after fewer than 8-yr of service. Another tendon also failed in the same year (July 2011). Figure 1-D shows the Roosevelt Bridge in Florida, which was temporarily braced during the emergency repair of the corroded internal tendons in 2020. Similar PT corrosion problems have been observed in other countries, including the United Kingdom, France, Italy, South Korea, and Hong Kong. Two recent synthesis reports compiled many more corrosion problems, including the cases cited in this paragraph.[3,6]

© 2002 FDOT.

A. Niles Channel Bridge.[2]

Source: FHWA.

B. Varina-Enon Bridge.[3]

© 2011 FDOT.

C. Ringling Bridge.[4]

© 2020 FDOT.

D. Roosevelt Bridge.[5]

Figure 1. Photos. Examples of corrosion-induced tendon failures.

Assessing the tendon conditions at randomly selected locations can be unreliable, destructive, and even impossible in many cases. Moreover, a full-scale inspection of any large PT bridge can be time consuming and cost prohibitive in reality. Therefore, bridge owners tend to rely on limited inspection data to determine the current state of the bridge. This kind of maintenance practice can lead to a false sense of security and run the risk of underestimating corrosion damage that may be occurring somewhere in the bridge.[1] Once a PT bridge has corrosion issues, it is very difficult or even impossible to replace the affected tendons, and corrective actions can be expensive. For instance, the Florida Department of Transportation (FDOT) spent an estimated $55 million on repairing 11 PT bridges.[7]

A web document published in 1998 recommended additional research and field trials on nondestructive evaluation (NDE) and nondestructive testing (NDT) techniques designed for grouted PT tendons.[8] In 2007, the Federal Highway Administration (FHWA), partnering with the American Association of State Highway and Transportation Officials and Transportation System Preservation Technical Services Program, organized a national workshop to identify bridge preservation and corrosion mitigation research needs. This preservation workshop produced a comprehensive report entitled Transportation System Preservation Research, Development, and Implementation Roadmap.[9] The workshop participants chose “improved inspection techniques for steel prestressing strands, cables, and ropes” as the most urgent and important issue for bridge

preservation. Their recommendation can be justified because corroding high-strength materials can be more critical than the corrosion of ordinary reinforcing steel and steel members.

When the PT bridges need to be inspected, visual inspections are still primarily depended on to observe external signs of concrete deterioration, such as cracks, delaminations, spalling, rust stains, deflections, and so on. In certain situations, limited duct drilling and borescope inspection can be implemented. The ineffectiveness of the current inspection methodologies can be recognized from recent PT tendon failures observed in two U.S. PT bridges. The Wando River Bridge had been rated satisfactory in three biannual inspections performed in 2012, 2014, and 2016, despite the ongoing hidden corrosion problems. The inspectors could not identify the insidious corrosion problems due to the inability to inspect inside the ducts, diaphragms, and anchors. Even after a thorough condition assessment after the first tendon failed in 2016, the second tendon failed in 2018, although both failed tendons were situated very close to each other. The Mid-Bay Bridge also experienced tendon failures in 2000 and 2018. These cases highlight how critical it is to develop reliable NDE technologies for detecting corrosion damage in PT tendons before it is too late.[3]

Several published reports included the literature review of the NDT/NDE technologies applicable to PT tendons. The most comprehensive literature review can be found in a 2015 research report entitled Designing and Detailing Post Tensioned Bridges to Accommodate Nondestructive Evaluation and its summary version in an FHWA TechBrief in 2018.[10,11] Each of the following methods was discussed in terms of applications, methodology, limitations, the viability in PT applications, and references:

1. Acoustic emission (AE).
2. Electrically isolated tendon.
3. Ground penetrating radar (GPR).
4. Half-cell potential (HCP).
5. Impact echo (IE).
6. Infrared thermography (IRT).
7. Magnetic flux leakage (MFL).
8. Radiography.
9. Time domain reflectometry.
10. Ultrasonic testing.
11. Visual inspection.

The information provided in the reports should be helpful for ordinary engineers to grasp the fundamentals of individual methods.

A National Cooperative Highway Research Program research report published in 2014 also briefly discussed the capabilities and limitations of the following 14 NDE methods for PT tendons and stay cables in terms of accuracy, precision, ease of use, inspection requirements, and cost:[12]

1. Electromagnetic methods: GPR, IRT, and electrical capacitance tomography.
2. Magnetic methods: MFL, magnetic main flux method (MMFM)-permanent magnet type, and MMFM-solenoid type.

3. Mechanical wave and vibration methods: IE, ultrasonic tomography, ultrasonic echo (USE), sonic/ultrasonic pulse velocity, low-frequency ultrasound, and sounding.
4. Electrochemical method: electrochemical impedance spectroscopy (EIS).
5. Combinations of methods: GPR/USE, GPR/IE, MFL/sounding, MFL/IE, and IRT/USE.
6. Visual inspection.

The researchers' short literature review may not be sufficient to understand the state of the practice fully, but the researchers' own extensive laboratory evaluations using realistic mockup specimens led to useful conclusions: None of the NDE technologies they investigated was capable of identifying grout defects (compromised grout/void/water infiltration) and strand defects with high accuracy for the ducts buried in the concrete (webs, flanges, deviators, and anchorage regions of the PT system) and the deck and pylon anchorages of the stay cable system. However, it was noted that two NDE methods, namely, USE and IE, could identify grout defects in internal ducts with low to medium accuracy.

FDOT sponsored two NDE/NDT studies focused on PT tendons and published two reports in 2003.[13,14] The first report contained the assessment results of four NDT methods: impulse radar, IE, MFL, and high-powered x-ray imagining. These methods were applied onto internal PT tendons installed in Ramp D, which was located in the Fort Lauderdale-Hollywood International Airport interchange before it was demolished.[13] The second report was related to developing and validating an NDE method used in the field to detect voids and cracks in the grouted internal tendons among three techniques: scanning IE, spectral analysis of surface waves, and ultrasonic imaging tomography.[14]

Florida International University (FIU) performed additional laboratory and field investigations sponsored by FDOT. As a result, two reports were published in 2012 and 2017.[15,16] The 2012 report contained a general description and some exemplary data of the following NDE methods classified in seven groups:

1. Visual methods: direct visual inspection, long-term video monitoring.
2. Magnetic method: MFL.
3. Mechanical wave and vibration methods: sounding, AE, IE, impulse response (IR), ultrasonic imaging tomography, ultrasonic guided wave testing, global vibration response.
4. Electromagnetic wave propagation methods: IRT, impulse radar/GPR.
5. Electrochemical methods: HCP, linear polarization resistance, EIS, electrochemical noise.
6. Penetrating radiation methods: radiography, x-ray diffraction.
7. Direct prestress measurement technique.

As part of the 2012 study, a survey of State DOTs was also conducted to collect information regarding the need for major corrosion-related problems and challenges for the States. According to State DOT responses, 23 of 27 State DOTs needed corrosion inspection of steel strands or stay cables: Ten DOTs had major corrosion problems and challenges; seven DOTs had carried out research projects to develop the corrosion detection methodology; and five DOTs had used NDE tools for inspecting pretensioned strands, PT strands, or stay cables.

The 2017 report identified practical and effective NDT technologies that could be used for the in situ condition assessment of internal PT tendons before, during, and after the demolition of Ramp D at the Fort Lauderdale-Hollywood International Airport and laboratory testing: IR, IRT, AE, MFL, interferometric phase radar, and inductance measurement. Some results included in the 2017 report will be discussed further in chapter 4.

Although some bridge deck evaluations have used GPR, IE, electrical resistivity, and other NDE/NDT techniques, applying them to PSC bridges has been remained largely uncommon. After witnessing the Varina-Enon Bridge tendon failure in 2007, FHWA launched an in-house study in the following year to investigate the effectiveness of several NDE technologies for assessing insidious corrosion damage in external PT tendons and stay cables. As a result, the MMFM—a magnetic-based NDE technology—was identified as the most accurate NDE system, and it was chosen for further research. In 2016, FHWA initiated another research study to develop a proof-of-concept prototype for internal PT tendons using a similar magnetic flux-based system called the return flux method (RFM).

This report presents the experimental details and outcomes of two in-house research studies related to developing and evaluating magnetic flux-based NDE technologies for locating hidden corrosion damage in external and internal PT tendons.

CHAPTER 2. PRELIMINARY EVALUATION OF SIX NDE METHODS

This chapter describes how preliminary evaluations of six NDE methods were conducted to identify the promising method(s) before the main research study was launched.

TEST SPECIMENS

For the first in-house study, VDOT donated seven grouted external PT tendon segments retrieved from the Varina-Enon Bridge. They were 4.0 inches in diameter and 7–10-ft in length. Each tendon segment contained 19 0.6-inch, 270-ksi seven-wire strands. Among them, three segments were selected for laboratory testing and labeled as tendons A, B, and C. Different levels of artificial damage were introduced to them at Turner-Fairbank Highway Research Center (TFHRC) of FHWA. A saw equipped with a diamond blade (and an impressed current method (figure 2-A) and an impressed current method (figure 2-B) were employed to make the predetermined damage in the tendon specimens.

Source: FHWA.

A. Saw-cut method.

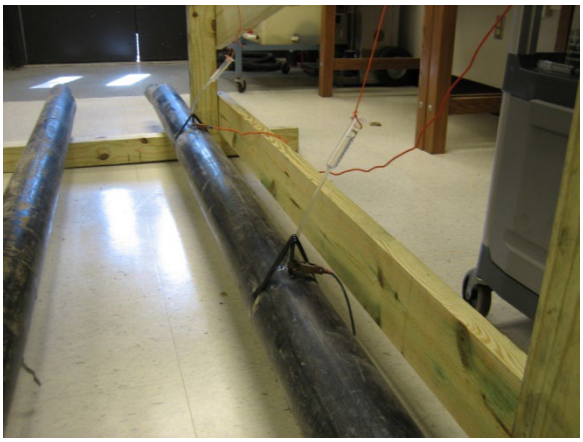

Source: FHWA.

B. Impressed current method.

Figure 2. Photos. Introduction of artificial damage into field tendon specimens.

The latter employed a potentiostat as a direct current (DC) power source, one of the strands in tendon A as a working electrode, a 3/8-inch diameter graphite rod as a counter electrode, and a 3.5-percent sodium chloride solution (by weight) as an electrolyte. First, a 0.5-inch hole was made through the high-density polyethylene (HDPE) duct to penetrate 1/4-inch deep into the grout (no bare strand exposed). Next, a small piece of sponge and the graphite rod were inserted into the hole. Finally, approximately 1 mA current was impressed from the strand (anode) to the graphite rod (cathode) while dispensing the saltwater into the sponge/grout periodically. The impressed current was maintained for 7 d without interruptions. This method was intended to introduce more realistic corrosion damage to a strand than the mechanical saw cuts.

In addition to the field specimens, two types of laboratory mockups were fabricated. The first type used eight concrete test slabs, to simulate a reinforced concrete bridge deck containing internal PT tendons, and longitudinal and transverse rebars. Each slab had overall dimensions of

7-ft long by 1.5-ft wide by 8-inches thick. These slabs were intended for two concurrent studies: corrosion resistance of next-generation reinforcing bars and evaluation of existing NDE methods for internal PT tendons.[17] For the latter, each slab contained a 1.5-inch galvanized metal duct and a 2.0-inch plastic duct in the middepth. The ducts contained unstressed seven-wire strands having different damage conditions without grout. Figure 3 shows some of the assembled molds before concrete pouring.

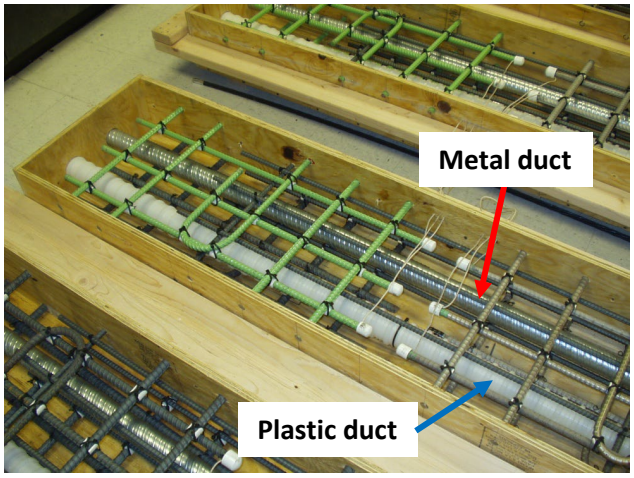

Source: FHWA.

Figure 3. Photo. Fully assembled test slabs ready for concrete casting.

The second type was a bundle of three 25-ft-long, 0.6-inch, seven-wire strands containing various levels of artificial damage along the strand length. After the strands were bundled on the ground (figure 4-A), the strands were inserted into a 2-inch polyvinyl chloride (PVC) pipe. As the final step, the pipe was filled with a commercially available prepackaged grout (figure 4-B).

Source: FHWA.

A. A bundle of seven-wire strands.

Source: FHWA.

B. Grout filling in the mockup tendon.

Figure 4. Photos. Preparation of a 25-ft long mockup tendon.

PRELIMINARY LABORATORY TESTS

At the beginning of this study, six NDE methods were identified as potentially viable techniques to detect insidious corrosion in the external PT tendons. Individual technology owners voluntarily participated in trying their systems on identical specimens. The participants tested the following NDE methods:

1. Ultrasonic flaw detection.
2. Sonic echo (SE)/ IR methods.
3. Magnetostrictive sensor (MsS) method.
4. Remanent magnetism (RM) method.
5. Thermography with induction heating method.
6. MMFM.

The following section briefly introduces each of the NDE methods and summarizes their test results, except for the MMFM, which will be fully discussed in the next chapter.

Ultrasonic Flaw Detection and SE/IR Methods

The ultrasonic flaw detection method uses the sound wave that travels through the interior of a material at a certain velocity until the wave is reflected at a boundary created by a different material or different physical conditions, such as internal cracks or voids. Travel speed depends on the material's properties, such as density and elastic properties.

Figure 5 shows ultrasonic measurements on one end of a seven-wire strand placed in an empty plastic internal duct (figure 5-A) and one end of a seven-wire strand in a grouted tendon specimen retrieved from the Varina-Enon Bridge (figure 5-B).

Source: FHWA.

A. An ungrouted plastic duct.

Source: FHWA.

B. A grouted external tendon.

Figure 5. Photos. Ultrasonic measurements.

The SE method is usually conducted with the IR as the SE/IR method to check foundation structures. The generated wave from an impulse hammer travels down in a shaft or a pile until an impedance change is encountered by a defect. Then, the reflected wave is measured by a receiver placed next to the impact point. The SE method analyzes the data in the time domain, whereas the IR method analyzes the data in the frequency domain. The two analysis methods complement each other to allow the most accurate foundation length and defect analysis possible.[18] The SE/IR method was tried on one end of an ungrouted seven-wire strand that had saw cuts inside an internal plastic duct (figure 6-A) and one end of another Varina-Enon Bridge tendon specimen (figure 6-B).

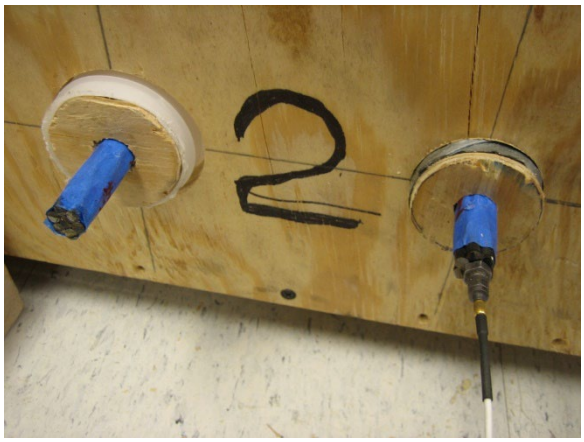

Source: FHWA.

A. An ungrouted plastic duct.

Source: FHWA.

B. A grouted external tendon.

Figure 6. Photos. SE/IR measurements.

At the end of the laboratory tests, it was clear that none of these NDE methods would work for the grouted PT tendons due to significant signal attenuation in the grout. Therefore, no further testing was pursued.

Guided Long-Range Wave MsS Method

The MsS is a type of transducer that can generate and detect time-varying stresses or strains in ferromagnetic materials. Magnetostriction is a property of ferromagnetic materials that causes them to change their shape or dimensions during magnetization. The operating frequency of the MsS ranges from a few hertz to several hundred kilohertz (kHz). The sensor has a broad frequency response and can be used over the entire operating frequency range. The sensor can transmit and detect elastic waves in a ferromagnetic material and thus perform the functions of a piezoelectric-type ultrasonic transducer. Since the signal in the receiving sensor is caused by time-varying strain or stress, the MsS can also perform the functions of a strain gauge, vibration sensor, accelerometer, and piezoelectric AE sensor.[19] For the laboratory tests, the longitudinal wave mode with a 10–30 kHz frequency was employed. The wave velocity was approximately 1.8×10^5 inches/s.

Figure 7 shows close-up views of MsS setup on a grouted 2-inch diameter and 25-ft long mockup (figure 7-A) and a grouted Varina-Enon Bridge tendon specimen (figure 7-B).

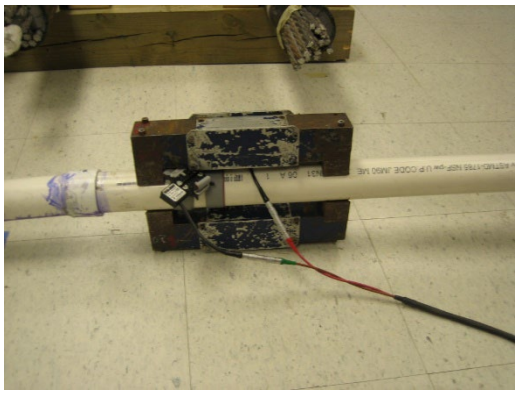

Source: FHWA.

A. A grouted 25-ft-long mockup.

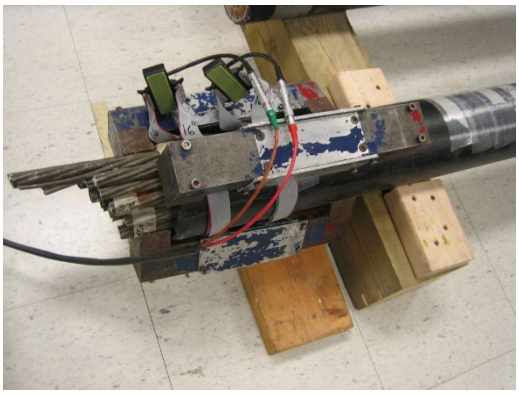

Source: FHWA.

B. A grouted external tendon.

Figure 7. Photos. MsS measurements.

Figure 8 and Figure 9 show examples of the MsS data from the 25-ft-long mockup and the field tendon sample, respectively.

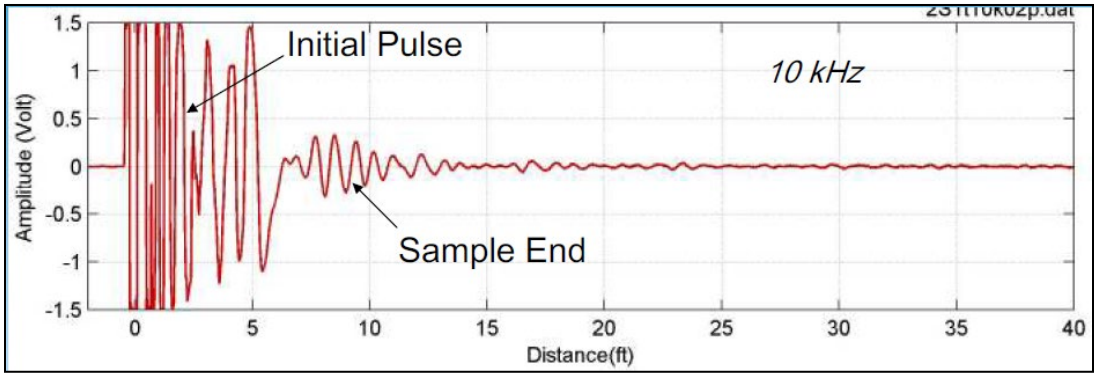

Source: FHWA.

Figure 8. Graph. MsS data from the 25-ft mockup.

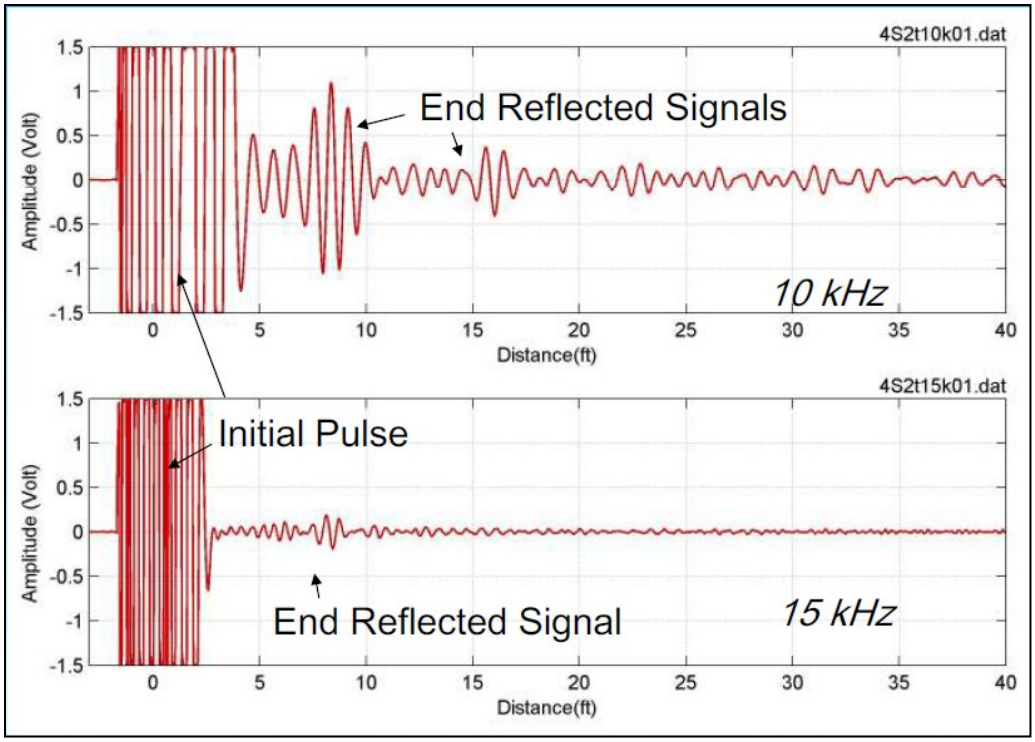

Source: FHWA.

Figure 9. Graph. MsS data from the grouted tendon specimen.

The MsS could not identify the locations of the artificial damage in the specimens. It was concluded that cementitious grout and no tension in the specimens contributed to very high wave attenuation. Consequently, no further testing was performed.

RM Method

The RM Method can detect potentially unsafe conditions in pretensioned and PT concrete structures by locating wire fractures in the prestressing steel. The residual magnetic field of the tendons is measured at the concrete surface once the tendons have been premagnetized with an electromagnet. Wire fractures produce characteristic magnetic leakage fields that can be measured with appropriate sensors at the concrete surface. The parameters associated with fractured wires have been quantitatively identified in the laboratory and confirmed in the field. The knowledge of these parameters can estimate the reduction of the cross-sectional area or the number of fractured wires in a tendon. After the multilevel process of measuring data related to certain concrete units' magnetic states, clear signals can be seen at the fracture locations.[(20)]

The RM method was tried on several Varina-Enon Bridge tendon specimens containing various artificial saw-cut damages and ungrouted internal tendon mockups. Figure 10 shows the electromagnet carriage of the RM method on a Varina-Enon Bridge tendon specimen (figure 10-A) and an internal tendon mockup (figure 10-B).

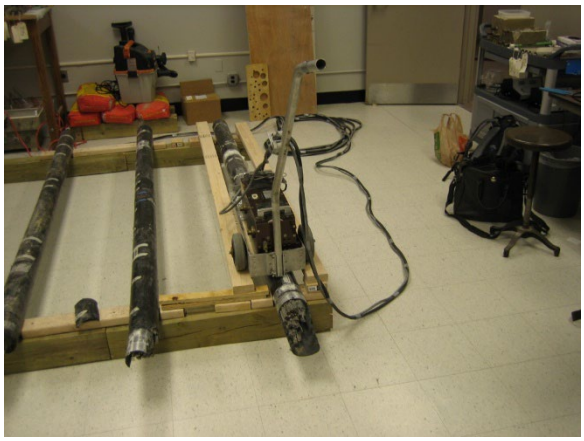

Source: FHWA.

A. Grouted external tendon.

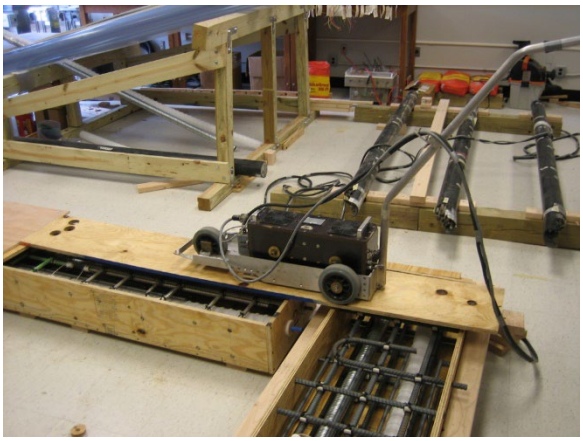

Source: FHWA.

B. Internal tendon mockup.

Figure 10. Photos. RM measurements.

Figure 11 shows an example of RM method data collected from a Varina-Enon Bridge tendon specimen containing multiple saw cuts. The arrows in the graph indicate possible damage locations determined by using the RM method.

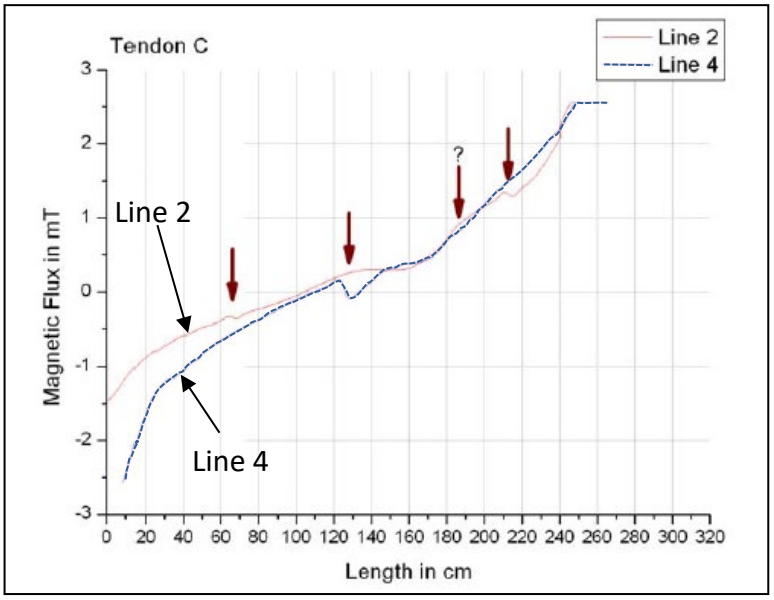

Source: FHWA.

Figure 11. Graph. Example of RM measurement data.

After comparing actual damage locations in the specimens and the RM method data, it was determined that the RM method identified only some of the damage locations, and section losses at the identified damage locations could not be quantitatively estimated. It also failed to detect artificial damages in the internal tendon mockups. Therefore, no further testing was performed.

Thermography With Induction Heating Method

Thermography for detecting corrosion of reinforcement in concrete was developed based on the principle that a corrosion layer surrounding a rebar serves as a thermal insulator. Since corroded rebars cool more slowly than uncorroded ones upon heating, the corrosion can be detected by measuring the difference in cooling rate. This method does not rely on direct solar heating of flat surfaces.[21]

The employed thermography system consisted of an infrared camera, an induction heater, and a power generator. The induction heater raised the temperature of the specimens to about 110 °F.

Figure 12 shows an experimental setup being tested on three Varina-Enon Bridge tendon specimens (figure 12-A) and a thermal image of a specimen with an infrared camera (figure 12-B).

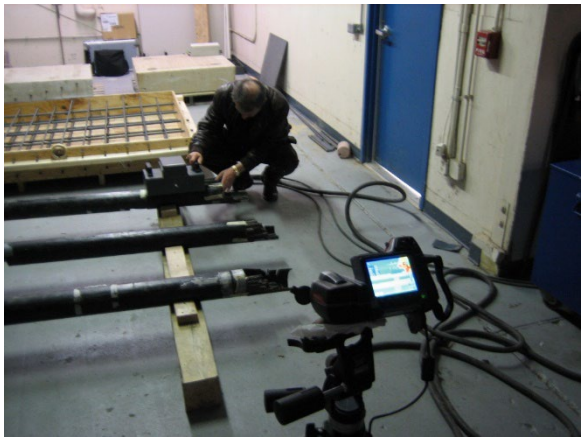

Source: FHWA.

A. Measurement setup.

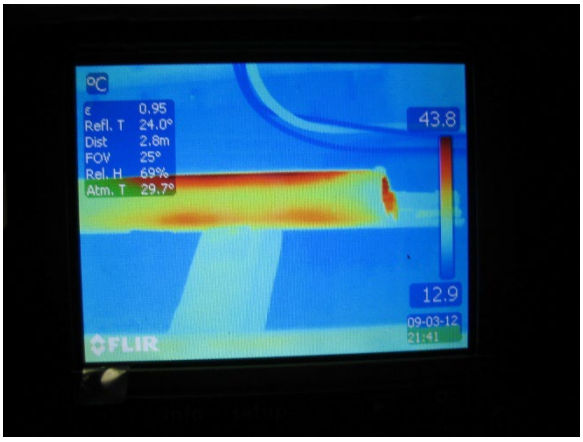

Source: FHWA.

B. Thermal image.

Figure 12. Photos. Induction thermography.

Although thermography could generate differential thermal images of the tendons, it was concluded that this technology was not useful to locate hidden corrosion damage in the grouted tendons, especially in the field. Therefore, no further testing was performed.

MMFM

The MMFM relies on a fundamental principle that when a ferromagnetic material, such as a steel strand, is magnetized to saturation, the magnitude of the magnetic flux flowing in the material is proportional to its cross-sectional area. Therefore, if there is a reduction of the cross-sectional area (i.e., a corrosion-induced section loss), a change of magnetic flux occurs accordingly.

FHWA learned about the MMFM system being tested at the Carlton Laboratory of Columbia University by a research team from the Tokyo Rope Manufacturing (TRM) Company in Japan. As part of another FHWA study, they were testing a full-scale mockup of the Manhattan Bridge's main suspension cable.[22] After exchanging several emails, FHWA and TRM agreed to conduct a laboratory trial of the MMFM system. In preparation for the trial, the TRM designed

and manufactured a solenoid-type magnetizer for the 4-inch-diameter external tendons, and FHWA brought three Varina-Enon Bridge tendon specimens to the Carlton Laboratory in September 2008. After observing the promising performance of the MMFM system, the second round of laboratory testing was carried out with an improved (the second-generation) solenoid-type MMFM system at TFHRC in June 2009.

The preliminary laboratory tests determined that MMFM was the most accurate among the NDE methods evaluated during the voluntary participation. Therefore, the subsequent research effort was focused only on the MMFM systems. The next chapter describes the details of multiple-phase testing and improvements of MMFM systems designed for the external PT tendons.

CHAPTER 3. MMFM FOR EXTERNAL TENDONS

Based on the preliminary laboratory test results of six NDE methods, MMFM was chosen for the full laboratory study as a potentially viable method for detecting insidious corrosion damage in the external PT tendons. This chapter presents details of the MMFM systems.

INTRODUCTION TO MMFM

This NDE technology relies on a fundamental principle that when a ferromagnetic material, such as a steel strand, is magnetized to saturation, the magnitude of the magnetic flux going into the material is proportional to its cross-sectional area. Therefore, if corrosion damage reduces the cross-sectional area, then the magnetic flux decreases accordingly. Figure 13 depicts this phenomenon.

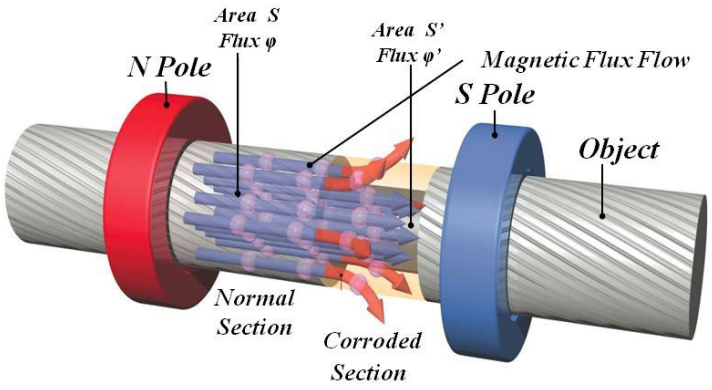

Figure 13. Illustration. Flow of magnetic flux in a metal object.[23]

When a magnetizer and a search coil are installed on a metal object and current flows through the wrapped electrical cable around the magnetizer, magnetic flux (ϕ) flows inside the object. The flux can be measured by a flux meter connected to the search coil, as shown in figure 14.

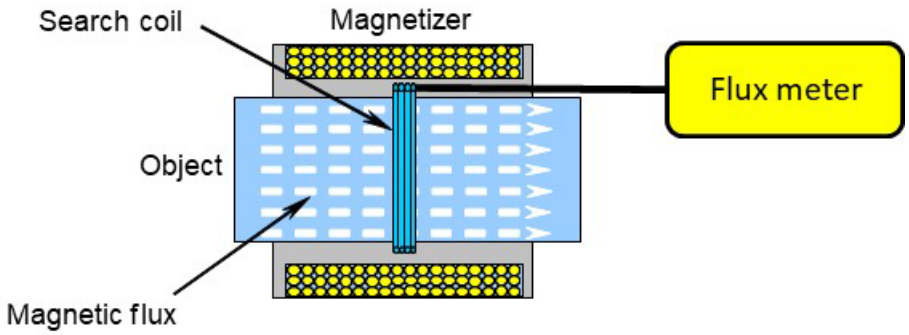

Figure 14. Illustration. Schematic of a magnetic flux measurement.[23]

The induced voltage in the search coil is proportional to the rate at which the magnetic flux changes. Therefore, the total change in magnetic flux ($\Delta\phi$) is calculated by integrating the induced voltage over time, according to the equation embedded in figure 14.

There are two types of MMFM systems specifically designed for external PT tendons (and stay cables): the solenoid type, using alternating current (AC), and the permanent magnet type, using permanent magnets. Both are equipped with unique features to accommodate PT tendons in the field, as discussed in the following section.

Solenoid-Type MMFM System

Figure 15 shows a schematic of a solenoid-type MMFM system, which consists of the magnetizing unit, measuring unit, and computing unit.

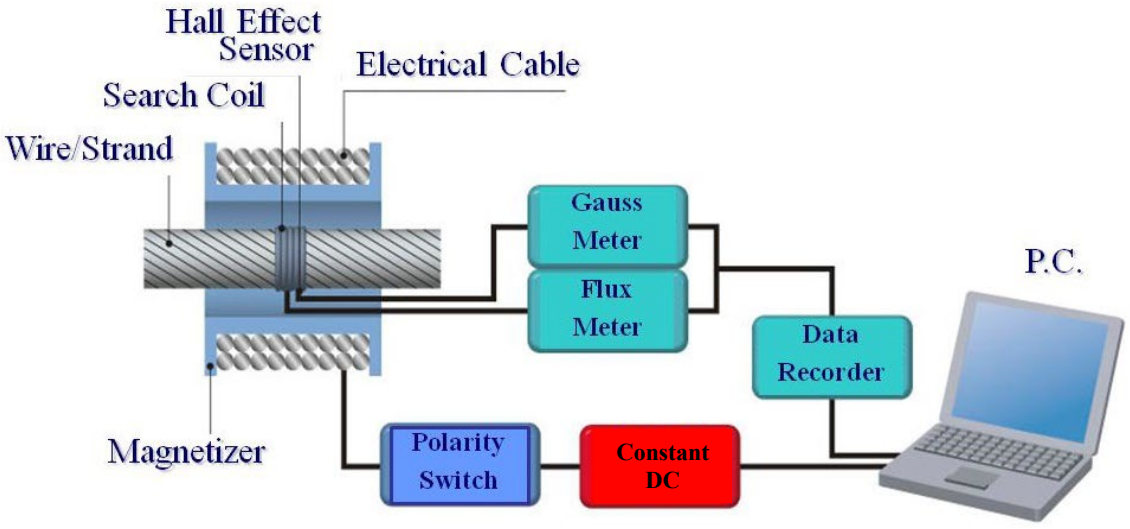

PC = personal computer.

Figure 15. Illustration. Schematic of the solenoid-type MMFM system.[23]

This MMFM system can function only when the following units work in sequence:

1. The magnetizing unit magnetizes the object: a magnetizer (an assembly of an aluminum bobbin and electrical wire wrapped around the bobbin), rolling wheels, electrical cable, polarity switch, and DC supply.
2. The measuring unit measures the magnetic field and the magnetic flux: a search coil, a flux meter, Hall effect sensor(s), and a gauss meter. A Hall effect sensor produces the voltage proportionally to the intensity of the magnetic field that passes through the sensor, and a gauss meter measures the changes in the magnetic field.
3. The computing unit stores the experimental data and performs data analysis by using proprietary software: a data recorder and a laptop computer.

The magnetizer can magnetize the metal object up to saturation level, depending on the magnitude of the electrical current. The solenoid-type MMFM system operates in two

measurement methods: scan measurement and point measurement. Each method has unique application features, and, depending on the objective of a particular testing program, any one or both methods can be chosen. Each measurement method is described in the following sections.

Scan Measurement

Scan measurements are made by moving the magnetizer and search coil at a constant speed along the object's length. When a constant current maintains a constant magnetic field, constant magnetic flux flows into the cross-sectional area of the object. As previously discussed in conjunction with figure 13, magnetic flux decreases where the cross-sectional area decreases (the magnetic flux also depends on the magnetic history of the material). Figure 16 illustrates the scan measurement method schematically.

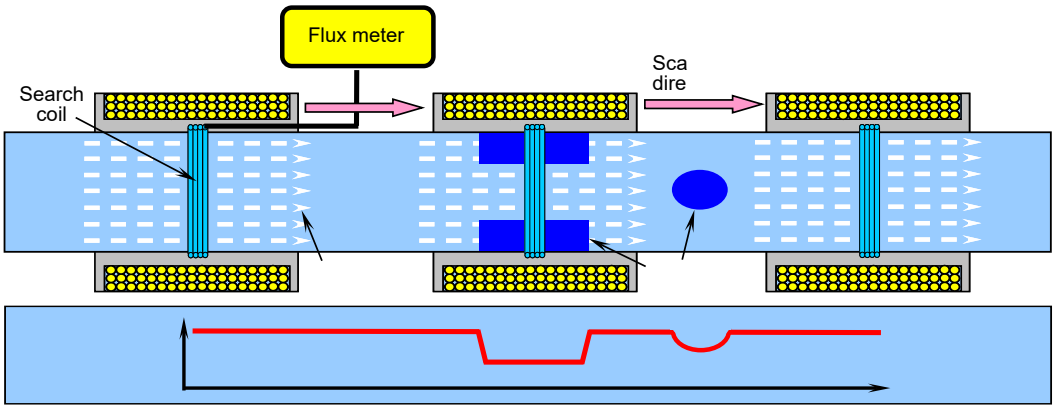

Figure 16. Illustration. Schematic of scan measurement.[23]

The schematic depicts the magnetizer scanning three locations while it is being moved from left to right. The reduced magnetic flux data are also illustrated at two locations having corrosion damage. The difference in magnetic flux ($\Delta\phi$) measured between two arbitrary points at 0 and x along the object can be calculated as a function of time (t) using induced voltage, according to figure 17.

$$\Delta\phi = \int_0^t \frac{\partial\phi}{\partial t} dt = \int_o^x \frac{\partial\phi(x)}{\partial x} \frac{dx}{dt} dt = \phi(x) - \phi(0)$$

Figure 17. Equation. Determination of magnetic flux change in scan measurement.[23]

$\Delta\phi$ serves as a proxy for the relative section loss between the two points. This qualitative information is useful for quickly scanning the physical condition of the entire metal object and allows the user to identify suspected areas for performing an indepth evaluation with the point measurement method.

Point Measurement

The point measurement is performed by parking the magnetizer at a target point. Figure 18 illustrates a point measurement method schematically.

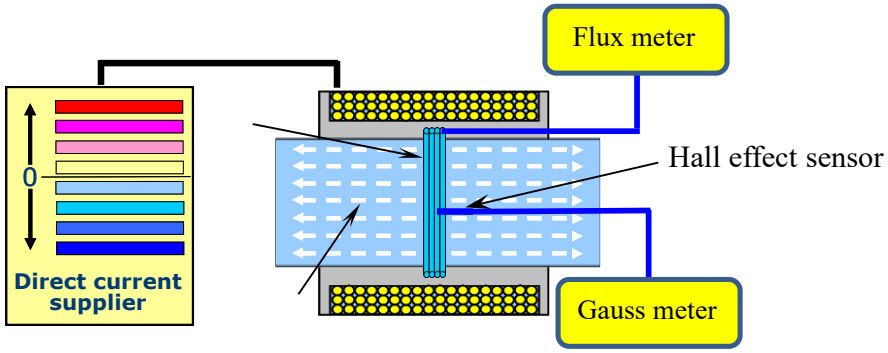

Figure 18. Illustration. Schematic of point measurement.[23]

By varying bipolar magnetization electrical current, a gauss meter can measure the changes in the magnetic field (*H*, or magnetic flux density) via the Hall effect sensor. The direction of the electrical current can be reversed by using a polarity switch. When the magnetic field changes, a flux meter connected to the search coil can measure the corresponding change in magnetic flux.

A point measurement produces a unique magnetic hysteresis loop, which shows the relationship between *H* and ϕ in the particular experimental setup. To produce any hysteresis loop, an electrical current needs to energize the magnetizer to full saturation level. Then, the current direction is reversed, which energizes the magnetizer again to the other saturation level in the opposite direction. Figure 19 shows two examples of hysteresis loop: One is generated under higher stress than the other.

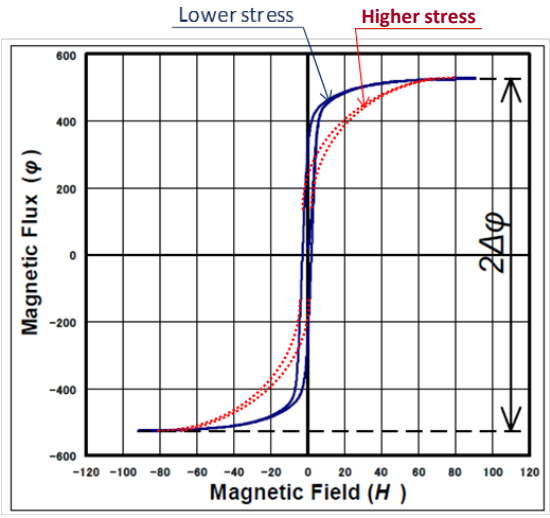

Figure 19. Illustration. Examples of the magnetic hysteresis loop.[23]

This figure illustrates that metallic objects under higher stress tend to exhibit a more gradual bending toward the saturation level than those under lower stress do. An operator can determine B_s (the magnetic field at the saturation level) and $2\Delta\phi$ (the total change in magnetic flux) under a very strong bipolar magnetic field by reviewing the hysteresis loop. The equation in figure 20 shows a proportional relationship among $2\Delta\phi$, B_s, and the cross-sectional area (A) of the metal object, which can estimate the absolute cross-sectional area at the measurement spot.

$$2\Delta\varphi = \int_{-H_m}^{H_m} \frac{\partial\varphi(H)}{\partial H}\frac{dH}{dt}\,dt = \varphi(H_m) - \varphi(-H_m) = 2B_S \cdot A$$

Figure 20. Equation. Determination of magnetic flux change in point measurement.[23]

Where:

H = magnetic field.
m = arbitrary measurement spot.
B_s is the saturated magnetic field.
A is the cross-section area at the measurement spot.

Figure 21 shows four actual magnetic hysteresis loops of wire ropes having different cross-sectional areas.

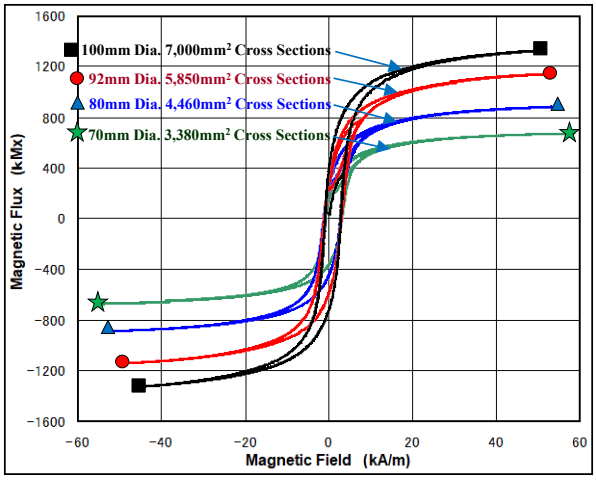

1 mm^2 = 0.00155 cm^2; kA/m = kiloamperes per meter.

Figure 21. Graph. Magnetic hysteresis loops for wire ropes having different cross sections.

The preceding examples are useful for visualizing the effect of cross-sectional area on magnetic flux: Wire ropes with larger cross-sectional areas require more magnetic flux to reach saturation level than ones with smaller cross-sectional areas.

These magnetic characteristics suggest that magnetic flux is sensitive to subtle changes in stress and cross-sectional area. Therefore, periodic point measurements at fixed locations can monitor changes in stress in the tendons and stay cables, or the development of new corrosion damage in the monitoring locations.

Permanent Magnet-Type MMFM System

This system was developed to eliminate an AC power requirement and tedious wire winding work in the field. Thus, it improves the field applicability with significantly reduced field preparation time, but it also reduces detection accuracy due to insufficient magnetism compared with the solenoid type. It works only with the scan measurement method over a metal object. Several upgrades have been made over 6 yr to improve its performance in the field.

As shown in figure 22, the permanent magnet-type magnetizer consists of a half-split bobbin, eight permanent magnets, a sensor unit, rolling wheels, and two spring-loaded clamps to lock the bobbin. The sensor unit contains one or two search coils, axial Hall effect sensors (H_{Gx}), and radial Hall effect sensors (H_{Gy}).

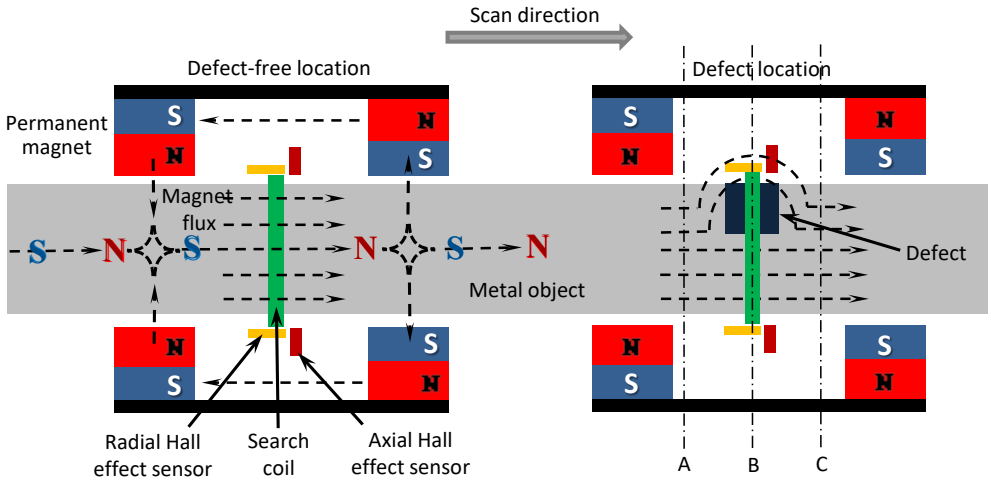

Source: FHWA.
N = north pole; S = south pole.

Figure 22. Illustration. Schematic of scan measurement by the permanent magnet type.

To ensure detecting a change of the magnetic flux wherever a defect exists in the metal object, the latest permanent magnet type has 16 Hall effect sensors around the metal object: eight radial sensors facing the center of the object and eight axial sensors in the longitudinal direction. Figure 23 shows the Hall effect sensor arrangement.

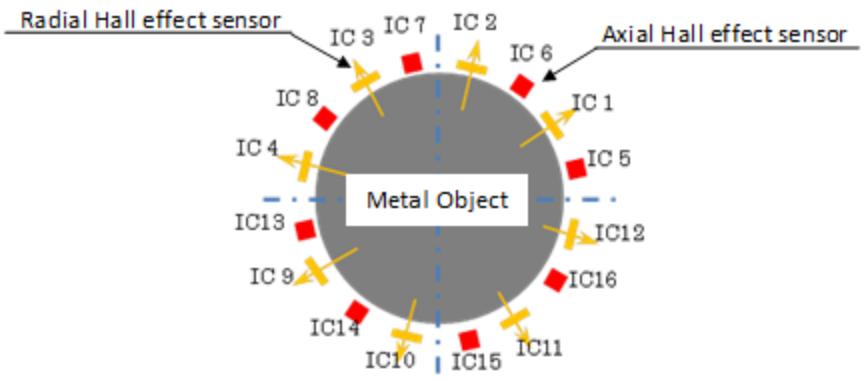

© 2016 Tokyo Rope Manufacturing Co.
IC = integrated circuit.

Figure 23. Illustration. Arrangement of 16 Hall effect sensors.

Figure 24, in conjunction with an imaginary defect in figure 22, describes how individual sensors respond when the magnetizer moves through defect-free locations (point A and point C in figure 22) and a defect containing the location (point B in figure 22) during a scan measurement.

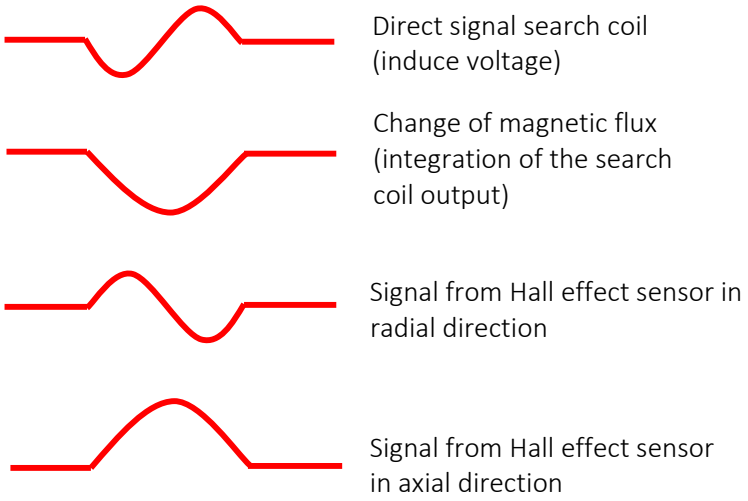

Source: FHWA.

Figure 24. Illustration. Schematic representation of MMFM data signals.

As magnetic flux leaks at the defect (point B in figure 22), the leaked magnetic flux is divided into a vertical component (radial) and a horizontal component (axial). During this transition from defect-free to defect to defect-free conditions, change of magnetic flux influences the sensors in the following ways:

- Search coils: Direct voltage signals from two search coils are automatically integrated by the change of magnetic flux. These integrated voltages begin to decrease beyond point A, become the lowest at point B, and return to the normal value at point C and onward.

- H_{Gy} in the upper region: After passing point A, magnet flux starts leaking. The vertical (i.e., perpendicular to the metal object) component of the leaked magnetic flux increases and then decreases until it becomes the normal value at point B. After passing point B, the vertical component of the leaked magnetic flux increases again in the opposite direction and then decreases until it becomes the normal value again at point C and onward.

- H_{Gx} in the upper region: After passing point A, magnet flux starts leaking. The horizontal (i.e., parallel to the metal object) component of the leaked magnetic flux increases until it becomes the highest at point B. After passing point B, the horizontal component of the leaked magnetic flux decreases until it becomes the normal value at point C and onward.

- H_{Gy} and H_{Gx} sensors in the bottom region: Because these Hall effect sensors are situated far away from the defect located in the upper region, the effect of the magnetic flux fluctuations is minimal.

EXPERIMENTAL PROCEDURE

Laboratory Specimens

As described in chapter 2, three tendon specimens retrieved from the Varina-Enon Bridge, labeled tendons A, B, and C, were employed to evaluate the solenoid-type MMFM system. The specimens contained different levels of artificial damage: saw cuts for large physical damage and impressed current damage for realistically small pit damage.

Figure 25 shows examples of damage from three saw cuts (figure 25-A) and minor impressed current damage of approximately 0.2-percent section loss (figure 25-B).

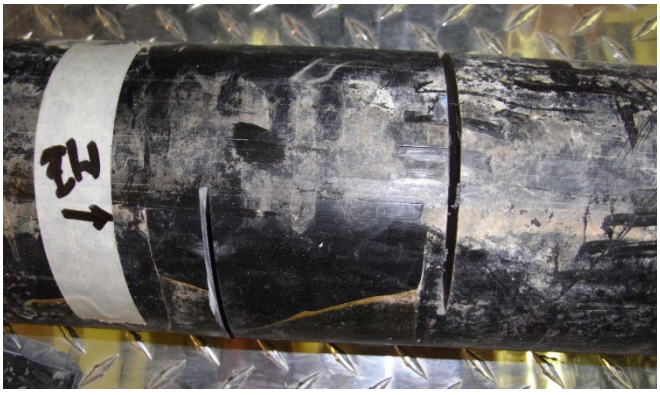

Source: FHWA.

A. Damage from three saw cuts.

Source: FHWA.

B. Impressed current corrosion damage.

Figure 25. Photos. Examples of artificial damage.

Table 1 summarizes the initial damage conditions of the specimens introduced by saw cuts and the impressed current method.

Table 1. Summary of initial damage introduced in the laboratory specimens.

Specimen ID	Damage ID (degree of damage)
Tendon A	R1 (minor corrosion by impressed current)
Tendon A	R2 (3 saw cuts)
Tendon A	R3 (minor corrosion by impressed current)
Tendon B	R1 (1 saw cut)
Tendon B	R2 (2 saw cuts)
Tendon B	R3 (1 saw cut)
Tendon C	R1 (1 saw cut)
Tendon C	R2 (1 saw cut)
Tendon C	R3 (2 saw cuts)
Tendon C	R3' (5 wires removed from R3)

ID = identifier; R = damage identifier.

In order to evaluate the accuracy of the permanent magnet-type MMFM system, a blind test was performed using a tendon D specimen from the Varina-Enon Bridge. Figure 26 shows two artificial section losses of 0.4-percent (figure 26-A) and 1.4-percent (figure 26-B).

Source: FHWA.

A. Damage number 1 (0.4-percent section loss).

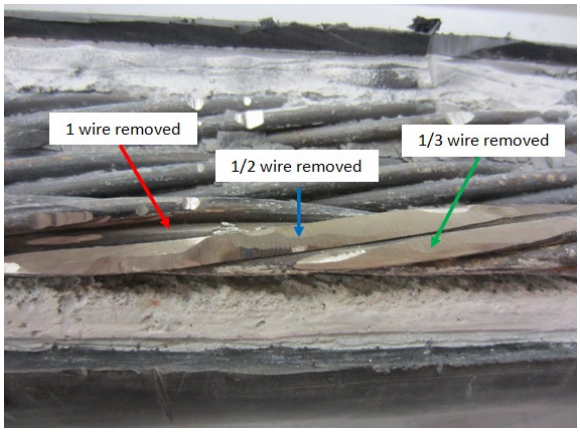

Source: FHWA.

B. Damage number 2 (1.4-percent section loss).

Figure 26. Photos. Damage conditions in tendon D specimen.

Development of Solenoid-Type MMFM System

During the study's early stage, researchers designed and fabricated two solenoid-type magnetizers, labeled the first generation and the second generation.

Figure 27 shows the first-generation solenoid-type testing at Columbia University's Carleton Laboratory (figure 27-A) and the second-generation solenoid-type testing at TFHRC (figure 27-B).

Source: FHWA.

A. First-generation magnetizer.

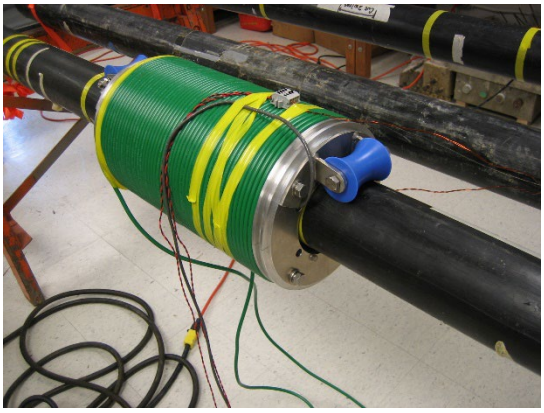

Source: FHWA.

B. Second-generation magnetizer.

Figure 27. Photos. Solenoid-type magnetizers.

The first-generation solenoid-type magnetizer was specifically designed for the external PT tendon specimens. A 6-inch diameter plastic casing (sensor holder) was the inner part of the magnetizer, and the casing grooves housed a Hall effect sensor and a search coil. The sensor holder was inserted into an aluminum alloy bobbin to form the core of the magnetizer. Then, the electrical cable was wrapped around the bobbin in several layers to complete the magnetizer assembly. The magnetizer was pushed and pulled along the tendon length to perform scan measurements. An overhead crane suspended the magnetizer due to its heavy weight. During the first trial, the operators realized that the first-generation solenoid-type magnetizer was difficult to maneuver. The inconsistent moving speed and frequent jerky motions during scanning also reduced the quality of the MMFM data. Despite the unexpected obstacles, the MMFM system was able to detect many damage locations (not section loss).

Based on experience gained from the first MMFM testing, the second-generation solenoid-type magnetizer was developed for the 4-inch tendons. It had improved features regarding size, weight, magnetomotive force, and ease of operation. For example, the second-generation magnetizer was 65-percent lighter (from 220 to 77 lb) and 37-percent smaller in overall diameter (from 15.7 to 10 inches) than the first-generation magnetizer. The magnetomotive force was also 31-percent reduced (from 40,000 to 27,500 ampere-turn (AT)). The improved magnetizer was equipped with plastic wheels to slide the magnetizer over an external PT tendon without a crane. As a result, the magnetizer's mobility was significantly improved while providing smooth and continuous manual operation. Other components, such as power supplies and switch boxes, became more compact as well. For both solenoid types, the minimum power requirements remained the same at three-phase AC, 240-V and 30 A.

Development of Permanent Magnet-Type MMFM System

The permanent magnet-type magnetizer can be separated into two halves so that operators can mount the partially opened magnetizer onto external PT tendons and stay cables.

Figure 28-A shows the opened permanent magnet-type magnetizer: half-split inner casing, a sensor unit containing a search coil and Hall effect sensors, four sets of half-split permanent magnets, half-split outer body shell, and four rollers on each end of the magnetizer. Figure 28-B shows the fully assembled permanent magnet-type magnetizer on a 4-inch external tendon.

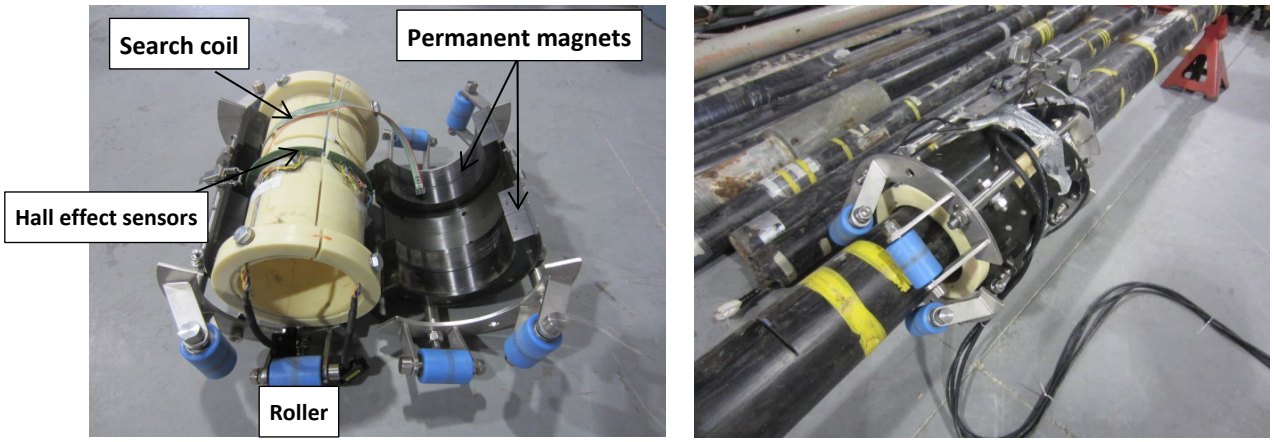

Source: FHWA.

A. Opened condition.

Source: FHWA.

B. Assembled condition.

Figure 28. Photos. Permanent magnet-type magnetizer.

A dedicated controller was also developed for the permanent magnet-type MMFM system. Powered by a 9-V battery, the controller transmits the driving voltage to the Hall effect sensors, receives a signal from each of the sensors, and integrates the signal from the search coil. The collected signals are saved on a memory card for subsequent data analysis with a laptop computer equipped with MMFM software.

Comparison of Two MMFM Systems

The solenoid type and the permanent magnet type have their pros and cons from physical and operational standpoints. Table 2 provides a comparison chart of the two systems.

Table 2. Comparison of solenoid-type and permanent magnet-type MMFM systems.

Category	Solenoid-Type (second-generation)	Permanent Magnet Type
Major capability	Locate corrosion damage areas	Locate corrosion damage areas
Estimation of section loss	Quantify actual section loss accurately	Estimate section loss qualitatively
Magnetic strength	Ability to change magnetic strength by changing the magnetizing current	Limited magnetic strength
Magnetizer polarity	Can change current polarity	Cannot change magnet polarity

Category	Solenoid-Type (second-generation)	Permanent Magnet Type
Additional capabilities	Monitor stress in the object and development of new corrosion damage	—
Magnetizer weight	77 lb (from first-generation 220 lb)	56 lb
Measurement Method	Point measurement; scan measurement	Scan measurement
Magnetizer exterior	Aluminum bobbin	External shell casing
Introduction of magnetism	Wrapped electrical wire	4 semicircular-shaped permanent magnet sets
Sensor holder	Cylindrical plastic casing	Half-split plastic casting
Search coil	1 search coil	1 search coil
Hall effect sensor	1 Hall effect sensor	16 Hall effect sensors
Number of rollers	2 each	4 each
Encoder type	Separate wire encoder	One built-in digital encoder
Components	Flux meter	Battery-powered one-unit controller
Components	Gauss meter	Signal cable
Components	DC supplier; polarity switch; data reader; power cables	—
Data type	Magnetic field; magnetic flux hysteresis (point); magnetic flux chart (scan)	Induced voltage signal of search coil; change of magnetic flux; signal of Hall effect sensors
Power requirement	Generator for three-phase AC 240-V/30-A	None
Auxiliary equipment	Electrical wire wrapping machine	None
Required number of operators and time	4–5; 60~90 min	2–3; 10~20 min

—No data.

The number and orientation of Hall effect sensors are the major differences between the solenoid type and the permanent magnet type. While the solenoid type has a single Hall effect sensor at the center of the sensor holder, the permanent magnet type has evenly distributed eight Hall effect sensors in the radial direction and eight Hall effect sensors in the longitudinal direction, as shown in figure 23.

The solenoid type produces a nearly flat magnetic flux line in a defect-free metallic object, but the permanent magnet type exhibits a curved magnetic flux line for the same condition. As a result, a reduction of magnetic flux is not proportional to a reduction in the object's cross-sectional area. Also, different magnetic field patterns cause different patterns of the magnetic flux line.

The solenoid-type MMFM system produces two types of data based on the measurement method. A point measurement gives an absolute magnetic flux value associated with a hysteresis loop between the magnetic flux and the magnetic field at each measurement location. Therefore, this method can estimate accurate and quantifiable section loss compared with other NDE methods. A scan measurement yields a magnetic flux chart that shows relative flux values along the specimen length with respect to absolute magnetic flux. This method provides an overall superior corrosion damage detection capability for considering both speed and accuracy. However, during the field trials, the solenoid type required considerable preparation time (60~90 min per tendon), and at least four people were needed for each measurement. These requirements were a significant drawback in the field.

The permanent magnet-type MMFM system produces three types of data: an induced voltage signal from the search coil, relative changes in magnetic flux by integrating the induced voltage, and voltage signals from the Hall effect sensors. Although the permanent magnet type needs minimal preparation and measurement time (10–20 min per tendon) and two to three people, it cannot change the magnet's north-south polarity and has limited magnet strength. Therefore, the permanent magnet type can only run for scan measurements and detect relatively larger section losses than the solenoid type.

Based on the strengths and weaknesses of each MMFM system, an appropriate system should be chosen for the objective of a particular field-testing program. For example, the permanent magnet type is preferred for tasks requiring rapid scans and an overall condition assessment. In contrast, the solenoid type is suitable for accurate damage assessment in critical areas.

Field Evaluations in the Varina-Enon Bridge

The Varina-Enon Bridge was chosen for evaluating the field performance of the MMFM systems because there could still be many tendons that were vulnerable to further deterioration due to poor grout conditions. Also, full support and cooperation could be obtained from VDOT and the FHWA division office.

The main objective of the field evaluations was to determine whether the MMFM systems could be used in the field without affecting the accuracy and performance observed in the laboratory. Therefore, two rounds of field evaluations were made on some external tendons of the bridge.

First Visit With the Second-Generation Solenoid-Type MMFM System

The second-generation solenoid-type MMFM system was tried on some of the Varina-Enon Bridge tendons in 2010. A team of TRM engineers, FHWA researchers, and VDOT personnel evaluated the MMFM system over 4 d.

The second-generation solenoid type was powered by an industrial-grade generator providing three-phase AC at 240-V/30 A.

Figure 29 shows the magnetizer being installed on a test tendon using a motorized wire-wrapping system (figure 29-A) and an operator pulling the magnetizer with a rope during a scan measurement (figure 29-B).

Source: FHWA.

A. Motorized wire-wrapping system.

Source: FHWA.

B. Scan measurement.

Figure 29. Photos. First MMFM testing in the Varina-Enon Bridge.

A small pulley was installed at the test tendon's highest point. The upward scan was made by pulling the other end of a rope attached to the operator-facilitated magnetizer at a constant speed, and the downward scan was done by gravity while releasing the rope.

Before each scan measurement, a group of short wires was attached to the tendon bottom near the scan's starting and ending points. The extra mass added by these wires introduced the flux spikes in the magnetic flux chart, which served as the measurement reference points.

In most cases, two consecutive scans were made before completing the scan measurement per tendon. The first scan magnetized the tendon, and the second scan collected MMFM data. Operators learned that maintaining a constant speed and smooth glide over an HDPE duct manually was difficult to execute in the field. Neoprene couplers and hose clamps on the duct frequently impeded the smooth magnetizer movement. These obstacles contributed to variable magnetizer moving speed and jerky motion that resulted in unstable MMFM data. For these reasons, the in situ MMFM testing was more challenging for the operators than the laboratory testing. If suspicious areas were identified, the magnetizer was parked at each of those areas and performed a point measurement.

After the MMFM testing was completed, some of the suspected corrosion areas and intact control areas were excavated to verify actual physical conditions against the MMFM data. If good quality grout covered an excavated area without exhibiting rust stains or cracks, the strands in the grout were assumed to be in good condition, and no further excavation was made. If an excavated area exhibited an uncertain condition, the grout was removed for inspecting strand condition. As the final step, the excavated sections were restored with the original duct pieces, followed by wrapping them with heat-shrinkable tape or sheets.

Second Visit With the Permanent Magnet-Type MMFM System

Soon after developing the first permanent magnet-type MMFM system, a second visit to the Varina-Enon Bridge was made in 2015 to try the new system. In less than 3 d, 22 tendons were

scanned due to its much quicker installation and removal process than the solenoid-type magnetizer. It was estimated that the solenoid-type magnetizer could have taken nearly 2 w to cover the same number of tendons. Based on the MMFM data, five sections were opened to verify their conditions. The sixth one was already opened during the previous corrosion investigations conducted by VDOT.

Figure 30 shows a closeup view of the magnetizer installed on an external tendon (figure 30-A) and a scan measurement in progress using a pulley and rope (figure 30-B).

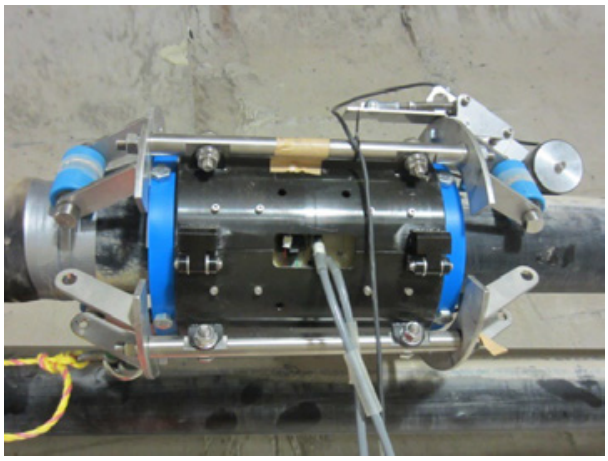

Source: FHWA.

A. Closeup view.

Source: FHWA.

B. Scan measurement.

Figure 30. Photos. Second MMFM testing in the Varina-Enon Bridge.

TEST RESULTS AND DISCUSSION

This section presents test results from the laboratory and field evaluations, followed by an in-depth discussion.

Laboratory Evaluations

Figure 31 shows photographs of artificial damage introduced into the tendon A specimen, and figure 32 shows a matching graph of magnetic flux versus scan distance data.

Source: FHWA.

A. R1 artificial damage in the tendon A sample.

Source: FHWA.

B. R2 artificial damage in the tendon A sample.

Source: FHWA.

C. R3 artificial damage in the tendon A sample.

Figure 31. Photos. Artificial damage conditions of tendon A specimen.

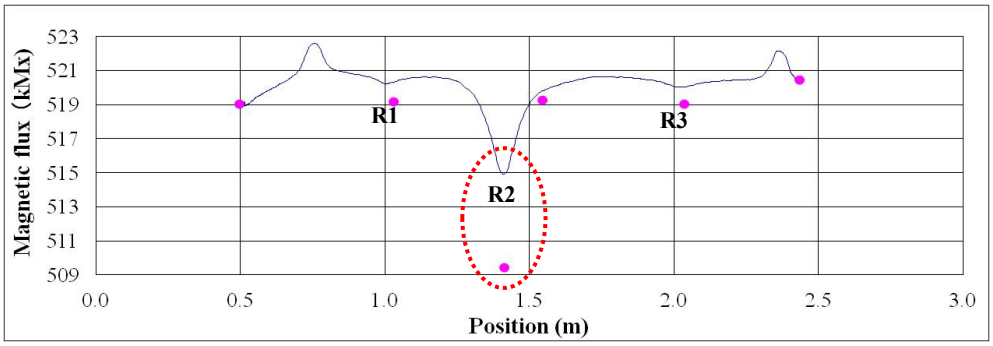

Source: FHWA.
1 m = 3.28 ft.

Figure 32. Graph. Scan measurement data from tendon A specimen.

As listed in table 1, artificial damages at R1 and R3 were introduced with the impressed current method, and the other damage at R2 was introduced by three saw cuts. Figure 32 contains two sets of magnetic flux data by scan measurement (curve) and point measurement (dots). The dots labeled R1, R2, and R3 correspond to the point measurement locations for artificial damage shown in figure 31. The remaining three dots indicate the point measurement locations at intact locations, that is, no artificial damage.

While both the scan and point measurement data at R1 and R3 showed reasonably good agreements, a large discrepancy was observed at the middle damage location (R2). The actual number of wires cut at this location was 16.5, but the MMFM estimated only a 2.7-wire cut, which is equivalent to a 2.0-percent section loss.

After discovering a noticeable discrepancy between the scan measurement data and point measurement data at R2, TRM carried out a small-scale laboratory study to investigate the effect of cut length on the MMFM data's accuracy. The TRM engineers fabricated a laboratory specimen by using the same number (19) of 0.6-inch seven-wire strands as the Varina-Enon tendon A specimen. Then, one strand was completely cut (equivalent to 5.3-percent section loss) to have different cut lengths ranging from 0.4 inches to 15.7 inches at eight locations. Repeated

point and scan measurements were made with the specimen. The following section summarizes the study findings.

Figure 33 shows two examples of the scan measurement data and point measurement data superimposed at three locations for a 0.4-inch cut (figure 33-A) and a 7.9-inch cut (figure 33-B). The middle points correspond to the cut locations and the left and right points for intact areas.

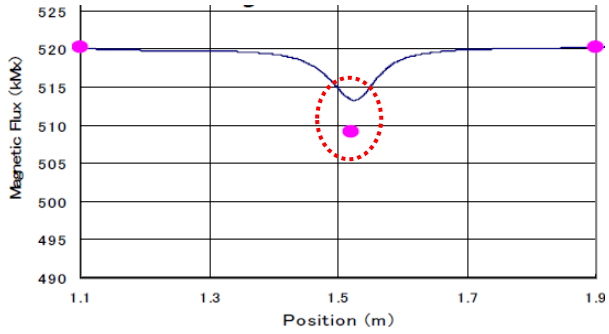

Source: FHWA.

A. Magnetic flux chart for defect length of 0.4 inches.

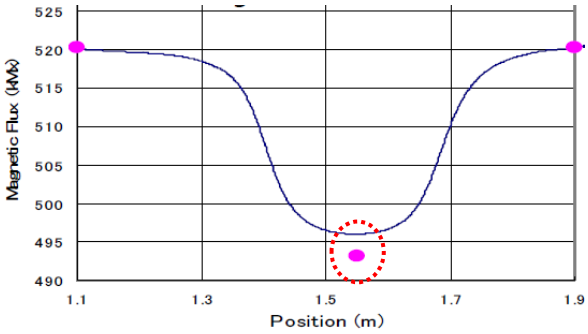

Source: FHWA.

B. Magnetic flux chart for defect length of 7.9 inches.

Figure 33. Graphs. Magnetic flux versus defect length data.

As expected, scan measurement data and point measurement data collected at the intact areas showed a high degree of agreement. The 0.4-inch cut produced a small and narrow magnetic flux reduction (figure 33-A), but the degree of agreement (ratio of two data) between the two sets of data was low. On the other hand, the 7.9-inch cut produced a noticeably deep and wide magnetic flux reduction (figure 33-B) and a higher degree of agreement between the two sets of data than the 0.4-inch case was observed.

Figure 34 summarizes the relationships between the cut length and the reduction of magnetic flux in terms of the magnetic flux rate obtained by the scan and point measurement methods.

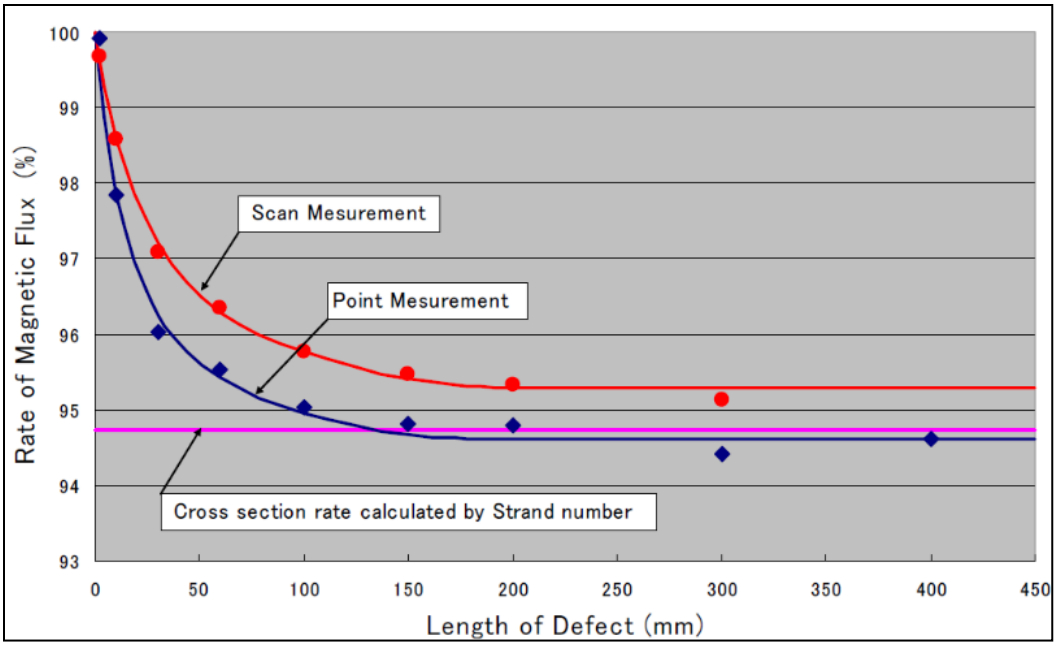

Source: FHWA.
1 mm = 0.039 inches.

Figure 34. Graph. Relationships between cut length and reduction of magnetic flux.

A horizontal line indicates an actual section loss of 5.3-percent, equivalent to one strand removed out of 19 strands and can serve as the reference to judge the estimates' accuracy against the actual section loss. The point measurement method yielded more accurate estimates than the scan measurement method in all cases. The latter underestimated the section losses by 0.6-percent. The most accurate estimation was made by the point measurement method when the cut length was 6 inches or longer. Therefore, it was confirmed that the discrepancy observed at R2 in figure 32 was caused when magnetic flux jumped over the narrow saw cuts.

Figure 35 presents the change of magnetic flux and the search coil signal of the permanent magnet-type magnetizer versus scan distance data from the tendon D specimen. The other two datasets, that is, the radial and H_{Gx} signals, are omitted here.

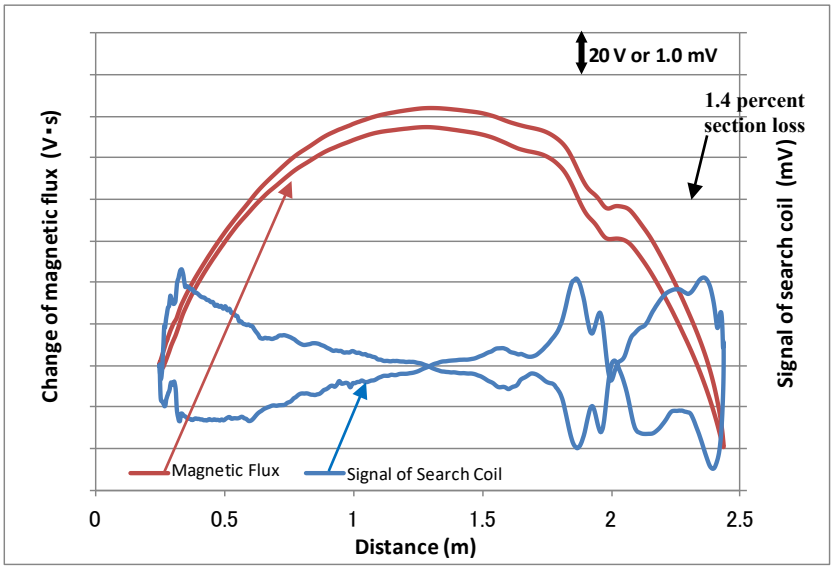

Source: FHWA.
1 m = 3.28 ft; V·s= volt-second.

Figure 35. Graph. Permanent magnet-type data from the tendon D specimen.

The permanent magnet type missed the 0.4-percent section loss (figure 26-A) but detected the 1.4-percent section loss (figure 26-B). Although the permanent magnet type's change of magnetic flux data is a good indicator for locating the suspected corrosion areas, it is not as accurate as the solenoid type.

Discussion on Laboratory Data

The first round of laboratory evaluation employed the first-generation solenoid-type system on the Varina-Enon Bridge's three tendon specimens. The magnetic field strength of 55 kA/m was used for the magnetizer. Table 3 summarizes the point measurement data, which were divided into intact and damaged areas. The mean magnetic flux value of each tendon's intact areas was calculated. Also, the overall mean magnetic flux value of all three tendons' intact areas was calculated to approximate the true magnetic flux of the undamaged tendons.

Table 3. Summary of the first point measurement dataset collected with the first-generation solenoid-type magnetizer.

Specimen ID	Intact Area ID	Magnetic Flux at an Intact Area (kMx)	Damaged Area ID (Degree of Damage)	Magnetic Flux at a Damaged Area (kMx)	Magnetic Flux at a Damaged Area as a Percentage of Mean Magnetic Flux at Intact Areas of the Tendon (Estimated Section Loss, Percent)
Tendon A	S1	519.07	R1 (minor corrosion)	519.02	99.89 (0.11)
Tendon A	M1	519.30	R2 (3 saw cuts)	509.45	98.04 (1.96)
Tendon A	E1	520.47	R3 (minor corrosion)	519.05	99.89 (0.11)
Tendon A	Mean	519.61	—	—	—
Tendon B	S1	519.19	R1 (1 saw cut)	515.65	99.24 (0.76)
Tendon B	M1	519.61	R2 (2 saw cuts)	514.13	98.95 (1.05)
Tendon B	M2	519.97	R3 (1 saw cut)	518.98	99.88 (0.12)
Tendon B	E1	519.61	—	—	—
Tendon B	Mean	519.60	—	—	—
Tendon C	S1	520.58	R1 (1 saw cut)	520.21	99.92 (0.08)
Tendon C	M1	520.54	R2 (1 saw cut)	514.74	98.86 (1.14)
Tendon C	M2	520.91	R3 (2 saw cuts)	495.99	95.26 (4.74)
Tendon C	E1	520.55	R3′ (5 wires removed from R3)	497.76	95.60 (4.40)
Tendon C	Mean	520.65	—	—	—
Overall mean	—	519.98	—	—	—

— No data.
ID = identifier; kMx = kilomaxwell.

As expected, the latter group (damaged areas) exhibited less magnetic flux than the former (intact areas). In each damaged area, a section loss was estimated by subtracting the magnetic flux percentage at the location with respect to the tendon's intact areas' mean magnetic flux from 100-percent. As listed in table 3, the estimated section losses ranged from 0.11 to 4.7-percent.

The second round of laboratory evaluation employed the second-generation solenoid-type magnetizer on the Varina-Enon Bridge's tendons A and C. No measurements were made on the tendon B specimen. Magnetic field strength was decreased from 55 kA/m with the first-generation magnetizer to 38 kA/m. As a result, the overall mean magnetic flux in the intact areas decreased from 519.98 to 510.67 kMx.

Table 4 summarizes the second round of point measurement data. Because the artificial damage was introduced in two steps, the table divides the magnetic flux data into three groups: the intact area group, the initial damage group, and the final damage group.

Table 4. Summary of the second point measurement dataset collected with the second-generation solenoid-type magnetizer.

Specimen ID (Tendon)	Intact Area ID	Magnetic Flux at an Intact Area (kMx)	Initial Damaged Area ID (Damage Level)	Magnetic Flux at an Initial Damaged Area (kMx)	Initial Damaged Area Magnetic Flux % of Intact Areas' Mean Magnetic Flux (estimated section loss, percent)	Final damaged area Area ID (Damage Level)	Magnetic Flux at a Final Damaged Area (kMx)	Magnetic Flux at a Final Damaged Area as % of Mean Magnetic Flux at Intact Areas (Estimated Section Loss, %)
A	S1	510.10	R1 (minor corrosion)	505.30	99.37 (0.63)	R1′ (1 wire removed)	500.70	98.47 (1.53)
A	M1	508.70	R3 (minor corrosion)	501.20	98.57 (1.43)	—	—	—
A	M2	506.20	—	—	—	R2″ (14 wires removed)	452.07	88.91 (11.09)
A	E1	508.90	—	—	—	R3′ (1 wire removed)	502.40	98.80 (1.20)
A	M	508.48	—	—	—	—	—	—
B	S1	511.50	—	—	—	—	—	—
B	M1	511.80	—	—	—	—	—	—
B	M2	512.20	—	—	—	—	—	—
B	E1	511.80	—	—	—	—	—	—
B	M	511.83	—	—	—	—	—	—
C	S1	512.00	—	—	—	—	—	—
C	M1	511.10	—	—	—	R2′ (1 wire removed)	508.70	99.41 (0.59)
C	M2	511.80	—	—	—	—	—	—
C	E1	511.90	R1 (1 saw cut)	507.80	99.24 (0.76)	R3″ (7 wires removed)	485.10	94.80 (5.20)
C	M	511.70	—	—	—	—	—	—

— No data.
ID = identifier; M = middle point; E = ending point; S = starting point.

Figure 36 shows linear regression analysis results of the first and second point measurement datasets listed in table 3 and table 4 to determine the relationship between estimated section losses and the corresponding magnetic flux data.

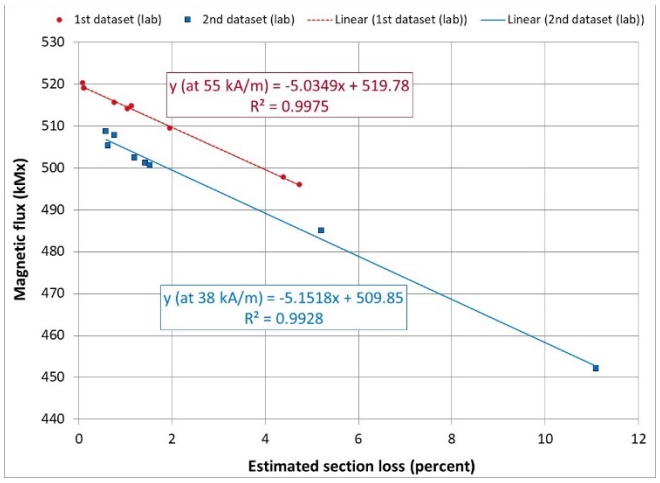

Source: FHWA.

Figure 36. Graph. Linear correlation between magnetic flux data and estimated section losses of the laboratory data.

Both datasets exhibited almost perfect one-to-one relationships with a coefficient of determination (R^2) greater than 0.99: as the section loss increased, the magnetic flux decreased linearly. There was a difference of approximately 10 kMx between the parallel regression fit lines because two datasets were collected with two different magnetic field strengths, 519.98 and 510.67 kMx.

Figure 37 shows a direct relationship between estimated section losses in table 4 and the actual section losses, which were determined based on the ratio of the number of physically removed wires to the total number of wires in the tendon.

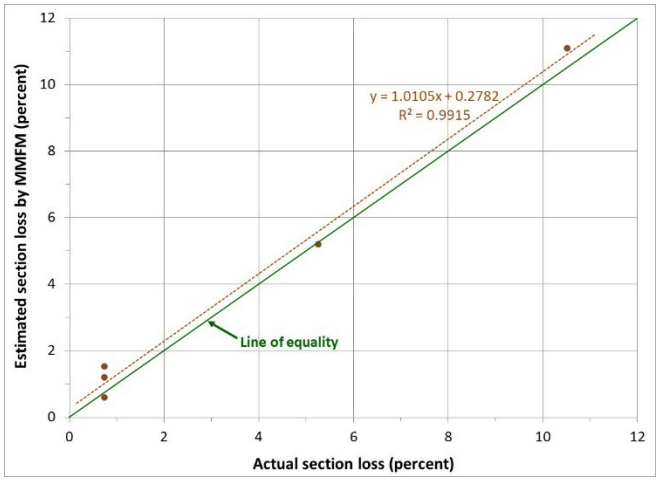

Source: FHWA.

Figure 37. Graph. Linear correlation between actual section losses and estimated section losses based on the second point measurement dataset.

The linear regression line falls close to the line of equality such that the second-generation solenoid-type overestimated section losses up to 0.27-percent. Conservatively speaking, this

level of overestimation should be better than an underestimation, considering typical corrosion damage observed in real PT bridges.

With these linear relationships established for the solenoid-type MMFM system, comparing the magnetic flux values measured at the suspected areas to a known intact area's mean magnetic flux of a specific tendon can estimate the section losses in the suspected areas.

Even though the solenoid-type MMFM system could detect section loss as low as 0.2-percent based on the regression equation for the flux data associated with 55 kA/m in figure 36, a 0.4-percent section loss would be considered the lowest detection limit for the point measurement method. This limit is equivalent to losing about 50-percent of a wire among 133 wires in 19 strands. As discussed with the data presented in figure 34, the scan measurement method produced up to a 0.6-percent error compared with the point measurement method. Therefore, a 1.0-percent section loss (0.4-percent plus a margin of error of 0.6-percent) would be considered the lowest detection limit for the scan measurement method.

Field Evaluations

The first round of field MMFM testing was conducted with five external tendons. One of them, labeled P12S12TW-3, was chosen because MFL testing in 2007 revealed that it suffered from severe corrosion damage. Because the tendon's corroded strands were already exposed without a duct, the magnetizer wheels could not roll smoothly over the exposed bare strands, and operators had to vigorously push and pull the magnetizer. Figure 38 shows the second-generation solenoid-type magnetizer on the exposed section of the tendon.

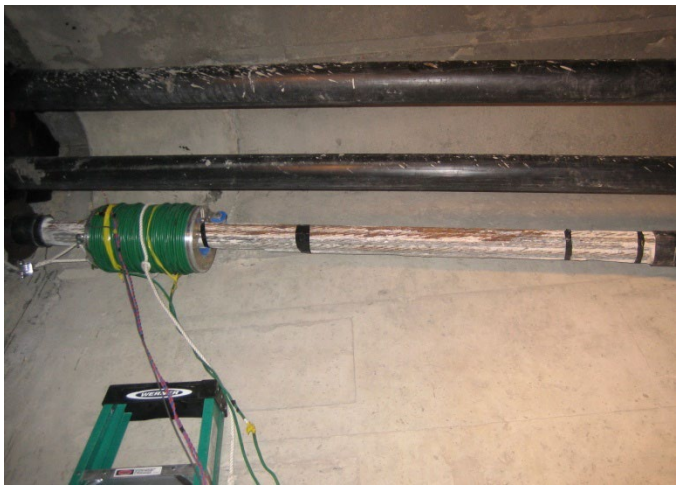

Source: FHWA.

Figure 38. Photo. MMFM testing of the P12S12TW-3 tendon.

Figure 39 shows the scan measurement data of the tendon, including the exposed bare strand section.

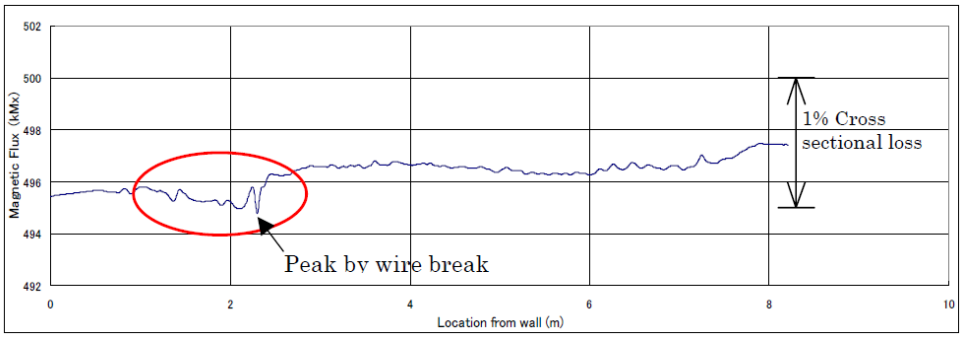

Source: FHWA.
1 m = 3.28 ft.

Figure 39. Graph. Scan measurement data from the P12S12TW-3 tendon.

The MMFM data exhibited reduced magnetic flux over the exposed bare strand section, indicated by the solid red ellipse. The recognizable corrosion damages were also visually confirmed in the section. Figure 40 shows two closeup photographs of the observed corrosion damages.

Source: FHWA.

A. Corroded strands.

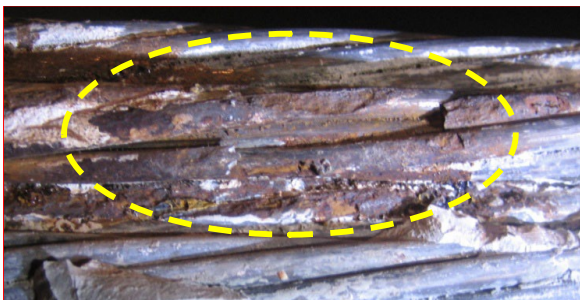

Source: FHWA.

B. Another area of corroded strands.

Figure 40. Photos. Closeup views of corroded strands.

Table 5 summarizes the point measurement data collected from the Varina-Enon Bridge tendons. As shown in this table, the scanned tendons did not contain any recognizable corrosion-damaged areas except for the most severely corroded tendon (P12S12TW-3), which produced four-point measurement data.

Table 5. Summary of point measurement data from the Varina-Enon Bridge tendons.

Tendon ID	Intact Area ID	Magnetic Flux at 38 kA/m at Intact Areas (kMx)	Magnetic Flux at 55 kA/m at Intact Areas (kMx)	Damage Area ID (Physical Condition)	Magnetic Flux at 38 kA/m at Damaged Area (kMx)	Magnetic Flux at 55 kA/m at Damaged Area (kMx)	Magnetic Flux at a Damaged Area as a % of Overall Mean Magnetic Flux at Intact Areas: 38 kA/m (Estimated Section Loss, %)	Magnetic Flux at a Damaged Area as % of Overall Mean Magnetic Flux at Intact Areas: 55 kA/m (Estimated Section Loss, %)
P14S13TE-1	U	471	499	—	—	—	—	—
P14S13TE-1	M	471	499	—	—	—	—	—
P14S13TE-1	D	472	500	—	—	—	—	—
P14S13TE-1	M	471	499	—	—	—	—	—
P14S13TE-2	U	470	496	—	—	—	—	—
P14S13TE-2	M1	471	497	—	—	—	—	—
P14S13TE-2	M2	470	496	—	—	—	—	—
P14S13TE-2	M3	470	496	—	—	—	—	—
P14S13TE-2	D	472	498	—	—	—	—	—
P14S13TE-2	M	471	497	—	—	—	—	—
P14S13TE-3	U	473	497	—	—	—	—	—
P14S13TE-3	M	472	498	—	—	—	—	—
P14S13TE-3	D	472	495	—	—	—	—	—
P14S13TE-3	M	472	497	—	—	—	—	—
P12S11TE-2	U	472	500	—	—	—	—	—
P12S11TE-2	M	473	501	—	—	—	—	—
P12S11TE-2	D	471	500	—	—	—	—	—
P12S11TE-2	M	472	500	—	—	—	—	—
P12S12TW-3	M1	472	498	U (minor corrosion)	469	496	99.50 (0.50)	99.61 (0.39)
P12S12TW-3	M2	470	497	M3 (minor corrosion)	469	496	99.50 (0.50)	99.61 (0.39)
P12S12TW-3	D	470	497	M4 (wire break)	462	488	98.02 (1.98)	98.00 (2.00)
P12S12TW-3	—	—	—	M5 (minor corrosion)	468	495	99.29 (0.71)	99.41 (0.59)
P12S12TW-3	M	471	497	Mean	467	494	—	—
Overall mean	—	471.35	497.95	—	467.00	493.75	—	—

— No data.
D = downward point; ID = identifier; M = middle point; U = upward point.

The estimated section losses observed on the P12S12TW-3 tendon varied between 0.39 and 2.0-percent, roughly equivalent to the loss of 0.5 to 2.5 wires. Because the tendon was active under significant stress, actual section losses could not be measured accurately after acid cleaning of the corroded wires, followed by pit depth measurements using a digital pit gauge. However, the MMFM data seemed to quantify the section losses reasonably well compared with the visual appearance of the corroded areas.

Figure 41 shows linear regression analysis results of the P12S12TW-3 tendon to determine a relationship between estimated section loss and the corresponding magnetic flux. For comparison purposes, the laboratory datasets shown in figure 36 were overlapped in the same graph.

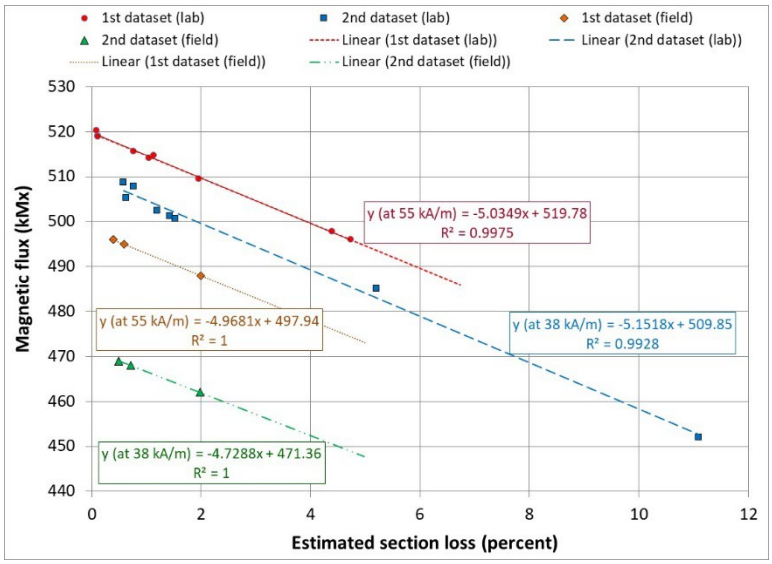

Source: FHWA.

Figure 41. Graph. Linear regression fits between magnetic flux and estimated section losses of the P12S12TW-3 tendon in relation to the laboratory datasets.

The field MMFM data of the P12S12TW-3 exhibited perfect fits with an R^2 of 1. The regression analysis results suggested that a specific one-to-one relationship between magnetic flux data and the section losses could be established to estimate any section loss in the field PT tendons having the same tendon configuration (i.e., strand size and the number of strands), provided that their mean magnetic flux value at the verified intact areas was determined in advance.

Another potential benefit of the MMFM methods is to estimate tensile stress being exerted in the tendons and stay cables qualitatively. This possibility is based on the fact that magnetic flux decreases as stress in the metallic object increases because stress induces physical deformation of a metal, that is, a strain that changes the metal's magnetization property. For example, the P12S12TW-3 tendon in service showed the field mean magnetic flux values of 498.0 kMx at 55 kA/m and 471.4 kMx at 38 kA/m at the intact areas. These values were 95.5-percent (versus 520.0 kMx at 55 kA/m) and 92.3-percent (versus 510.7 kMx at 38 kA/m) of the mean flux values measured in the "no-stress" laboratory tendon specimens retrieved from the same bridge. Figure 42 shows unpublished data from an internal research study that TRM conducted.

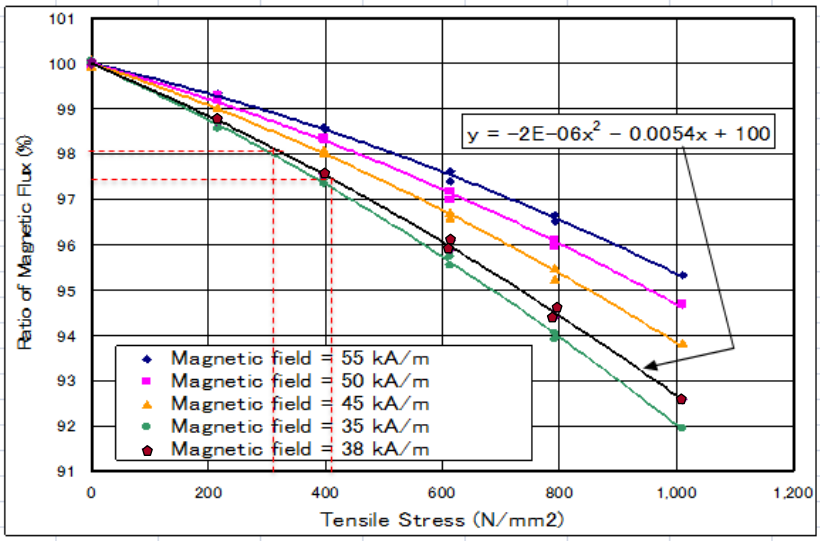

N/mm^2 = Newton per square millimeter; 1 N/mm^2 = 145.04 psi.

Figure 42. Graph. Influence of stress on the reduction of magnetic flux.

Even though direct comparisons between the flux data presented in figure 42 and the Varina-Enon Bridge's MMFM data cannot be made due to different test conditions, it is still interesting to see a unique relationship between increasing tensile stress and decreasing magnetic flux, as a function of the magnetic field. Therefore, the solenoid-type MMFM system may be able to monitor stress variations at a tendon's target locations by measuring the change in magnetic flux over time.

The permanent magnet-type MMFM system did not yield clear indications that any of the 22 scanned tendon sections contained apparent corrosion damage. To be sure, five sections exhibiting unusual or uncertain MMFM responses, such as reduced magnetic flux and disturbed signals from Hall effect sensors, were chosen for excavation. When the selected areas were opened, large gout voids and partially exposed strands existed along the length of the tendon. Figure 43 shows a typical tendon condition upon excavation.

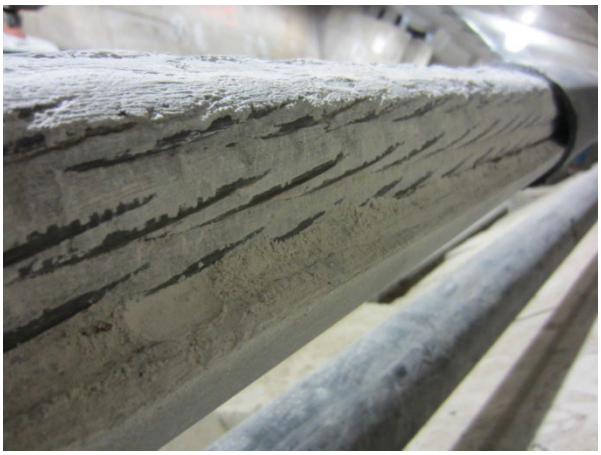

Source: FHWA.

Figure 43. Photo. Uncovered condition of a tendon exhibiting grout deficiencies.

While the tendons' bottom portion was filled with normally hardened grout, the grout in the top appeared weaker than the bottom grout, and white grout powder covered the exposed surfaces of grout void and strands. These conditions were likely caused by the grout segregation when excessive water could be mixed with cement during the grout operation. However, no recognizable corrosion damage was found on the exposed strand surface.

Figure 44 shows an example of uncertain MMFM data in terms of magnetic flux and search coil data obtained from a tendon section (SP12T10) that was later opened to examine its interior condition.

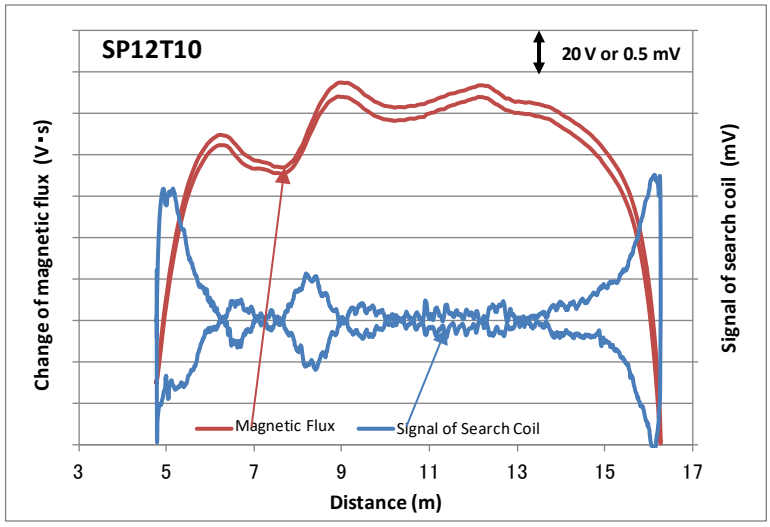

Source: FHWA.
V·s = volt-second.

A. Magnetic flux and search coil data.

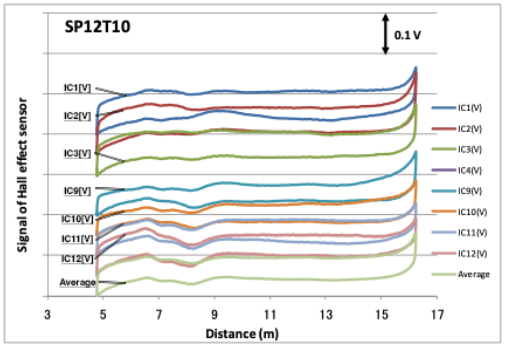

Source: FHWA.
1 m = 3.28 ft.

B. Axial Hall effect sensor (H_{Gx}) data.

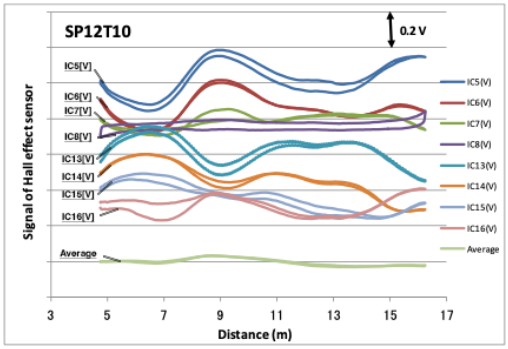

Source: FHWA.
IC = integrated circuit.

C. Radial Hall effect sensor (H_{Gy}) data.

Figure 44. Graphs. Permanent magnet-type MMFM data of a tendon.

Although there was a low probability of finding corrosion-damaged strands buried in the grout, the grout could not be removed for inspection because the tendons carried the live load. Thus, the damage detection capability of the permanent magnet-type MMFM system could not be determined.

More improvements were made to the permanent magnet-type MMFM system's hardware and the data analysis methodology based on the field experience. Since then, a couple of field projects—unrelated to the present study—established a 3.0-percent section loss as a conservative damage detection limit for the latest version of the permanent magnet-type MMFM system.[24,25]

Discussion of MMFM Systems' Field Performance

The field MMFM evaluations did not yield information as quantitative as the laboratory data for several reasons. First, the tendons tested in the Varina-Enon Bridge—except for one tendon—did not contain naturally occurring corrosion damages that exceeded the detection limits of the MMFM systems: 0.4-percent section loss by solenoid types' point measurement method, 1.0-percent section loss by solenoid type's scan measurement method, and 3.0-percent section loss for permanent magnet type. Secondly, the PT tendons were in service with tremendous stress, and only exposed strands were visually inspected. As a result, the strands buried in the grout could not be examined by invasive methods. Lastly, the magnetizer's inconsistent moving speed and extruded obstacles on the tendon surface caused signal distortions and disagreements between actual corrosion damage locations and those that appeared in the MMFM data.

Nonetheless, field evaluations of the MMFM systems demonstrated that they could be used in the field as an effective in situ NDE tool if corrosion damage in assessable sections of external PT tendons exceeded the detection thresholds established for the MMFM systems.

Some areas for improvement were identified to build efficient and practical MMFM systems readily available for field applications. For example, an autonomous scanning capability would be desirable to climb and descend the inclined tendons (and stay cables) at a constant speed. A commercially available motorized self-propelling system equipped with a synchronized digital distance encoder would be a good place to begin. A more challenging design feature for an ideal MMFM system may be the flexibility and adaptability designed for the ducts that have different diameters and extruded objects such as joint couplers, hose clamps, and air vents.

CHAPTER 4. RFM FOR INTERNAL TENDONS

This chapter describes the second FHWA study to develop and validate a laboratory prototype for internal PT tendons using the RFM. This in-house NDE study was launched after completing the MMFM systems developed for physically accessible metallic objects such as external PT tendons and stay cables.

PREVIOUS RESEARCH EFFORTS

The literature search of NDE technologies applicable to internal PT tendons identified research work performed by FIU and the University of Toledo. Since their studies explored the same concept of no-contact testing of the physically separated tendons as the RFM, their key findings are presented to understand what has been achieved before the RFM system is discussed.

FIU Studies

FIU explored two NDE systems by using MFL and inductance methods as described in the following sections.

MFL System

The FIU researchers developed two MFL systems powered by permanent magnets for internal tendons.[15,16] The later version—also a more sophisticated MFL system—was tested on a laboratory mockup and a decommissioned precast box girder segment retrieved from Ramp D, which was located near Fort Lauderdale-Hollywood International Airport. The laboratory mockup was built with a 4-inch-diameter plastic duct using PVC pipe and number 3 transverse rebars. Figure 45 shows the laboratory testing setup.

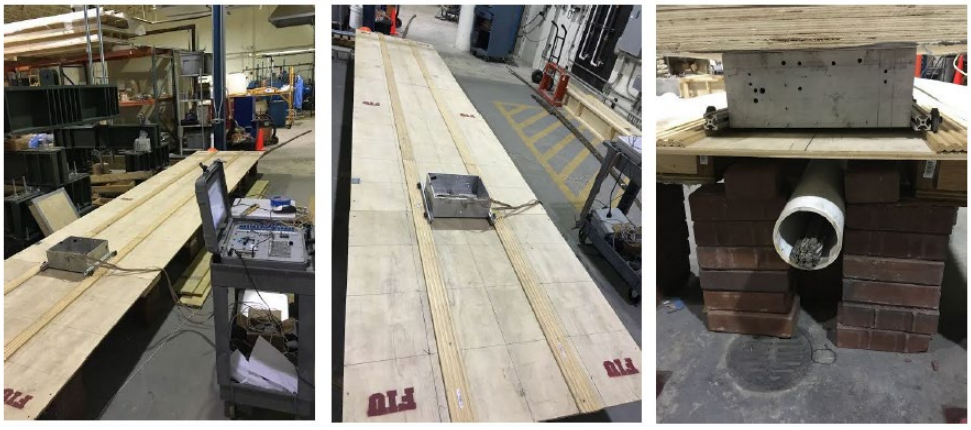

© 2017 FDOT. © 2017 FDOT. © 2017 FDOT.

A. Overview. B. Plywood platform. C. Cross section.

Figure 45. Photos. Laboratory setup for MFL testing.[16]

A 20-ft-long plywood platform was constructed, and rails were installed to guide the MFL carriage along with the platform (figure 45-A and figure 45-B). The clear cover between the platform and the duct was 2 inches (figure 45-C). The duct housed 10 0.6-inch strands containing three section losses of 14-, 50-, and 100-percent. The strands were magnetized by moving the permanent magnet over the strands in one direction several times. Figure 46 shows some laboratory test results: ND2 (active MFL test with undamaged strands), D2 (active MFL test with damaged strands), and D2−ND2 (difference of the two datasets).

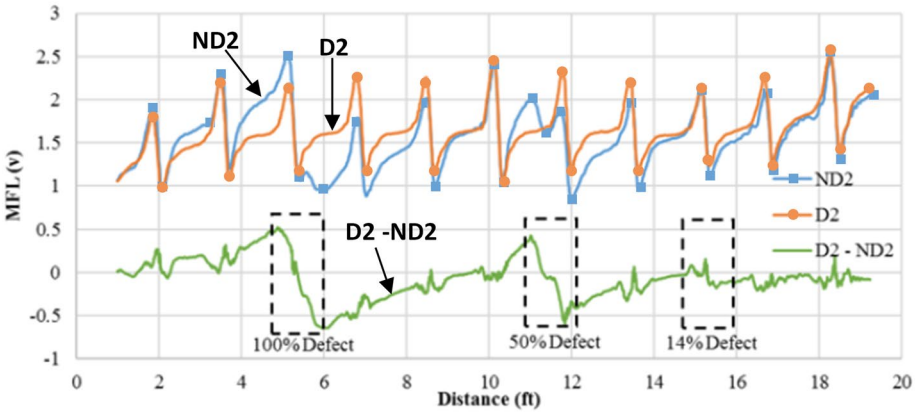

Figure 46. Graph. Laboratory test results obtained with the mockup.[16]

The Hall effect sensors detected disturbances of the magnetic field at the damage locations, as shown in figure 46. The D2−ND2 obtained with the active magnetic field method took the shape of a peak and valley at the defects. The observed inflection could be ascribed to many factors, including the defect size, magnetic strength, the distance between the Hall effect sensors and strands, and so on.[16] The researchers reported that their MFL system detected 50- and 100-percent section losses, but missed the 14-percent section loss. A wide transverse rebar spacing (~18 inches estimated by signal peaks in the graph) might help detect the 50-percent section loss by avoiding magnetic interference between the transverse rebars and the strands.

Figure 47 shows the schematic of the decommissioned box girder segment that was used to test the MFL system in a manner similar to the laboratory experiments.

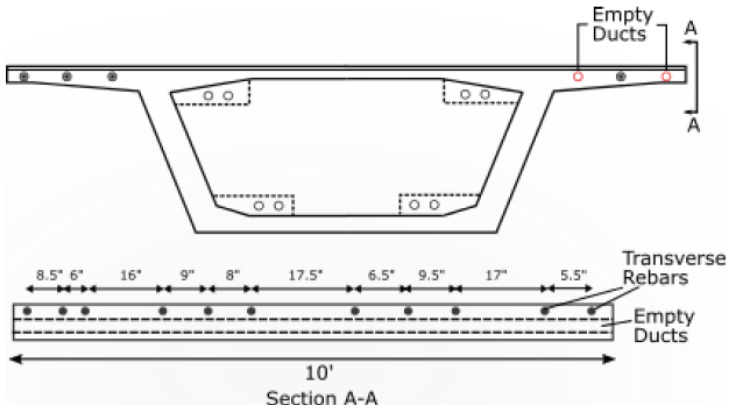

Figure 47. Illustration. Details of the decommissioned box girder segment.[16]

Galvanized 3-inch-diameter metal ducts were buried in the cantilever section of the top slab beneath approximately 3.5 to 4 inches of concrete cover and number 3 transverse rebars. The existing strands in the ducts were removed and replaced with seven new 0.6-inch strands for the MFL testing. Three cases of no damage (designated as SND), 100-percent section loss (SD), and no strands (SN) were tested with the active magnetic field method. The test strands prepared for the SD case were completely cut for 4 inches in the midlength to simulate complete metal loss. Figure 48 shows three MFL datasets and the transverse rebar locations.

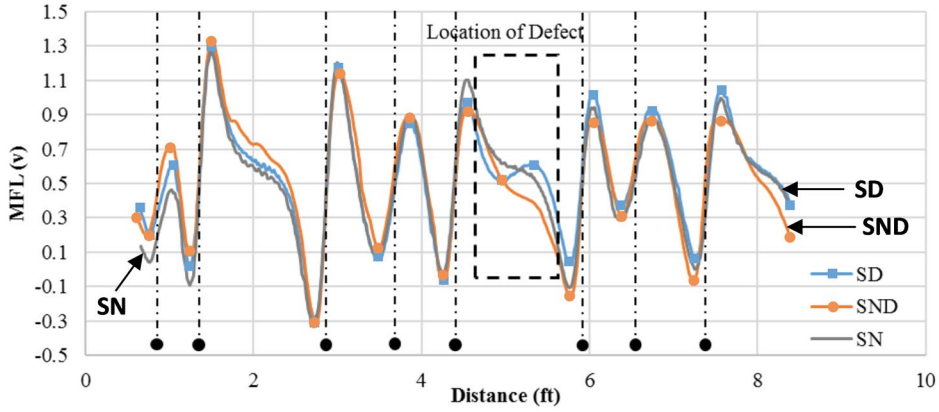

Figure 48. Graph. MFL test results of a bridge segment.[16]

The active MFL method identified the location of the 100-percent cut in this particular setup, where there was no transverse rebar at the defect location. The researchers speculated that the presence of a secondary ferromagnetic source (transverse rebars) could have affected the amplitude of signals at a smaller section loss due to incomplete magnetic saturation by the low magnetizing capability of the permanent magnet. In other words, disturbances and masking effects caused by the transverse rebars could yield complicated MFL signals that make it difficult to detect corrosion damage in real situations.

However, the researchers also indicated that data analysis techniques could reduce the effect of mild reinforcement observed in the laboratory test data, and the postprocessing of the segment test data could identify the damage. A numerical study validated the laboratory test data. Also, the detailed finite-element simulation could be used to improve the MFL system by determining sensor positions and choosing an appropriate magnetic field to achieve saturation. The researchers concluded that using an electromagnet was a more practical approach to improve defect detection capabilities. There was also a need to develop MFL testing protocols specifically designed for PSC bridges.[16]

Inductance Measurement Method

Another laboratory study was conducted with another mockup to determine the effectiveness of an electromagnetic-based inductance method. The laboratory setup consisted of a 20-ft-long tendon mockup made with multiple strands encased in a 4-inch PVC pipe. The strands had three section losses along the length: a 100-percent cut at 2.5-ft, a 50-percent cut at 10-ft, and a 14-percent cut at 16-ft. Since the penetration depth of the magnetic field around the inductor coil increased with the diameter of the coil, multiple inductor coil configurations were tested to find the best combination of penetration depth and resolution. A sheet of plywood was placed 3 inches above the mockup tendon to support the testing equipment. Inductance measurements were made at uniform intervals along the strand length, as shown in figure 49.

A. Overview.

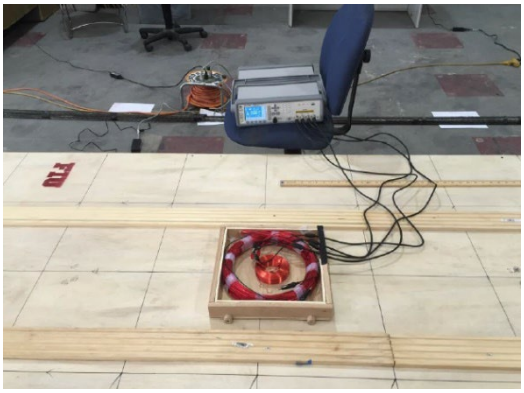

B. Induction measurement system.

Figure 49. Photos. Laboratory setup for induction measurement method.[16]

When inductance measurements were made in the vicinity of the defect (low inductance), a larger diameter coil picked up additional inductance from the undamaged section of the strands (high inductance). Therefore, the resolution of the inductance readings at a section loss decreased as the coil diameter increased. Multiple tests led to a good balance of penetration depth and resolution. A high-precision inductance meter produced the necessary test signal to generate the fluctuating magnetic field through the coil. Inductance measurement data collected at equally spaced points along the mockup strands matched well with the corresponding section losses, as shown in figure 50.

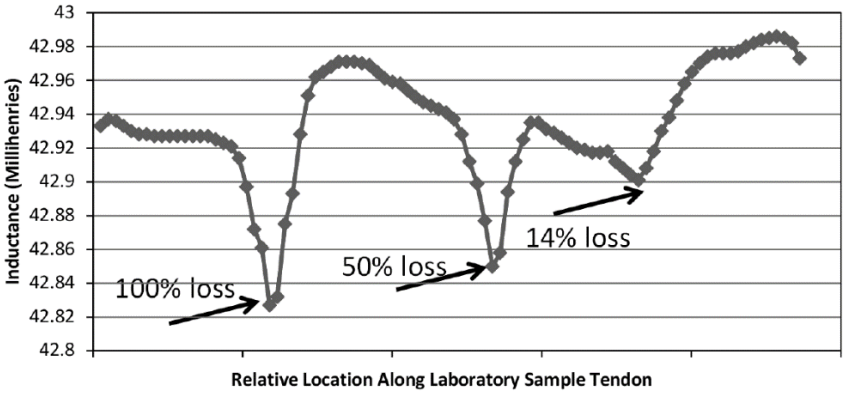

Figure 50. Graph. Inductance measurement data from the laboratory mockup.[16]

Figure 51 shows an inductance measurement in progress on the decommissioned box girder segment.

Figure 51. Photo. Modified second prototype elliptical coil used for inductance testing on the top slab of a precast segment.

The in situ measurements were difficult to make due to the variable clear cover and interference from steel components above the strands. Therefore, the coil dimensions were changed to have an elliptical shape such that the narrow dimension was parallel to the longitudinal axis of the strands, as shown in figure 51. To factor in these nonideal testing conditions, baseline inductance measurements were made at 107 equally spaced points along the 10-ft segment while adding one to six strands in the duct. The inductance measurement results are shown in figure 52.

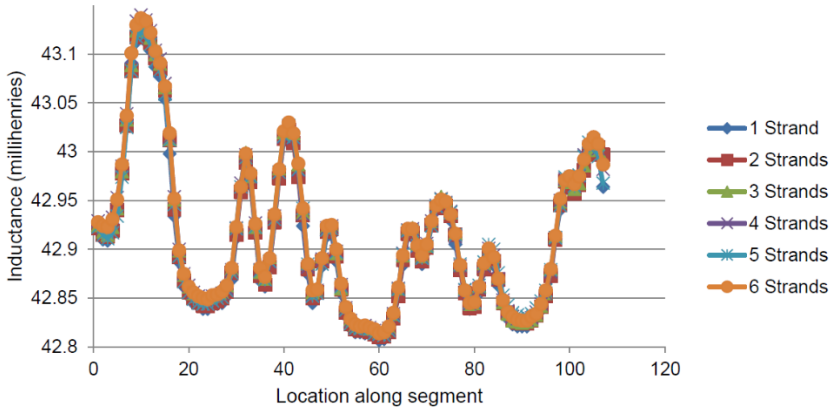

Figure 52. Graph. Inductance readings along the length of the segment for an increasing number of strands.[16]

The spikes in inductance in figure 52 were due to transverse rebars and transverse prestressing strands. The decreasing inductance from left to right was caused by the increasing distance between the inductor probe and the strands as the metal duct slopes down (increasing clear concrete cover) relative to the top of the concrete. The data showed there was an increased inductance for the larger (more strand) samples and an increased inductance at transverse rebar locations. This trend suggested that if a calibration dataset were made for future numerical comparisons, the location of a section loss could be detected even under transverse rebars.

The major factors affecting the inductance readings included the quality of the inductance meter, coil geometry, number of turns of the coil, test signal frequency, concrete cover over the tendon, and the metal duct's wall thickness. More importantly, the inductance method was very sensitive to magnetic interference (shielding) from secondary transverse rebars. Future potential improvements to the inductance method include the following**:**

- Modifying inductor coil geometry to sharpen (localize) the inductance reading.
- Modifying the coil turns and wrapping method to increase the penetration depth of the test field.
- Using a more precise inductance meter with a larger voltage test signal.
- Collecting and processing datasets is also an important issue to be investigated because averaging several datasets may provide a better-quality dataset to cancel the data outliers caused by electromagnetic noise.[16]

The University of Toledo Study—Induced Magnetic Field Detection (IMFD) Method

The University of Toledo published several documents related to the IMFD method in 2010 and 2011.[26,27,28] The researchers investigated how the magnetic properties of the prestressing strands were affected by the onset of corrosion when the strands were magnetized using an externally placed electromagnet. An IMFD method field trial was also conducted using a prototype the University of Toledo developed as part of another concurrent project.

The researchers developed an IMFD system using a yoke-shaped electromagnet and accompanying Hall effect sensors. The IMFD method used the principle that when a metallic object is magnetized externally by using an electromagnet, the change in magnetic properties is reflected in the amount of magnetic flux induced in the object (figure 53 illustrates imaginary magnetic flux lines passing through a steel specimen induced by a yoke-shaped electromagnet).

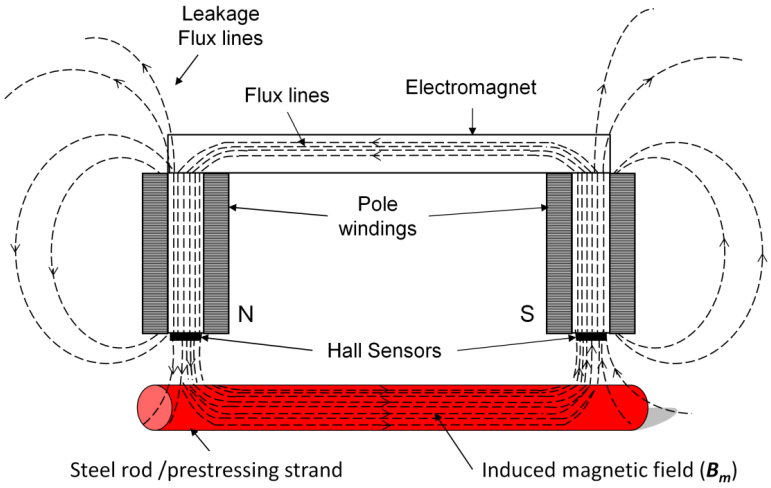

Figure 53. Illustration. Magnetic flux lines passing through the steel specimen induced by a yoke-shaped electromagnet.[26]

Hall effect sensors were mounted on the pole faces of the electromagnet to measure the axial component of the induced magnetic field accurately at a particular point on the steel.

For the laboratory study, the researchers used the AISI 1018 steel rods that had 11 cross-sectional areas (diameter 1/16–3/4 inches; length 18–24 inches), new seven-wire strands that had four cross-sectional areas (diameters 1/16~3/4 inches) and corroded seven-wire strands that were obtained from a demolished bridge (original diameter was 0.5 inches). Tests were conducted to study the magnetic reluctance of concrete by using different airgaps and concrete thicknesses for all the specimens. Hollow wooden blocks and concrete blocks were used to create physical separations of different sizes between the pole face and the steel specimens. Figure 54 shows the IMFD data from AISI 1018 steel rods and new seven-wire strand steel with different cross-sectional areas as a function of airgap from 0.75 to 2.0 inches.

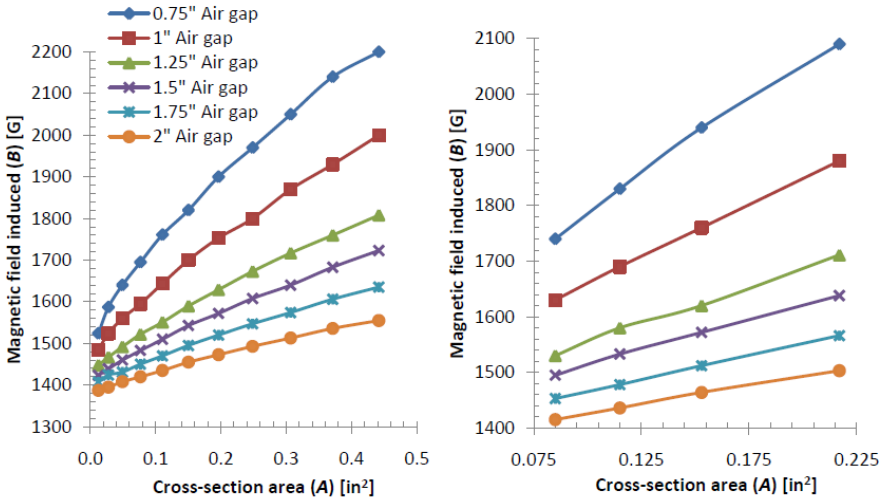

A. AISI 1018 steel rods. B. New seven-wire steel strands.

Figure 54. Graphs. Induced magnetic field versus cross-sectional area of steel specimens as a function of airgap.[26]

The induced magnetic field was proportional to the cross-sectional areas of both types of specimens. Also, the new seven-wire steel strands exhibited a higher degree of magnetization than the AISI 1018 steel rods. The researchers attributed this to the higher carbon content in the seven-wire steel strands and suggested that the metallurgy affected the amount of magnetic field induced in the steel specimens. Similar data obtained from five different thicknesses of concrete blocks are plotted in figure 55.

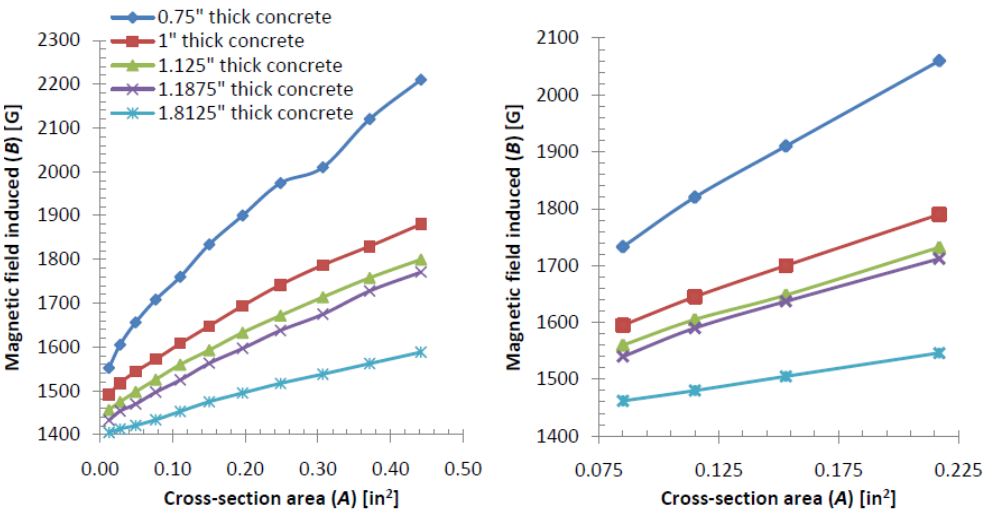

A. AISI 1018 steel rods. B. New seven-wire steel strands.

Figure 55. Graphs. Induced magnetic field versus cross-sectional area of steel specimens as a function of concrete thickness.[26]

A comparison between the induced magnetic field data presented in figure 54 and figure 55 showed that concrete had a slight damping effect on the magnetization for both types of steel specimens. Also, the seven-wire steel strands had a higher amount of induced magnetic flux in concrete. Finally, the magnetic field induced in the steel specimens could be related to the corresponding cross-sectional area, regardless of airgaps and concrete block sizes.

Figure 56 shows a corroded seven-wire strand specimen's estimated cross-sectional areas determined by the IMFD method and actual cross-sectional areas measured along its length.

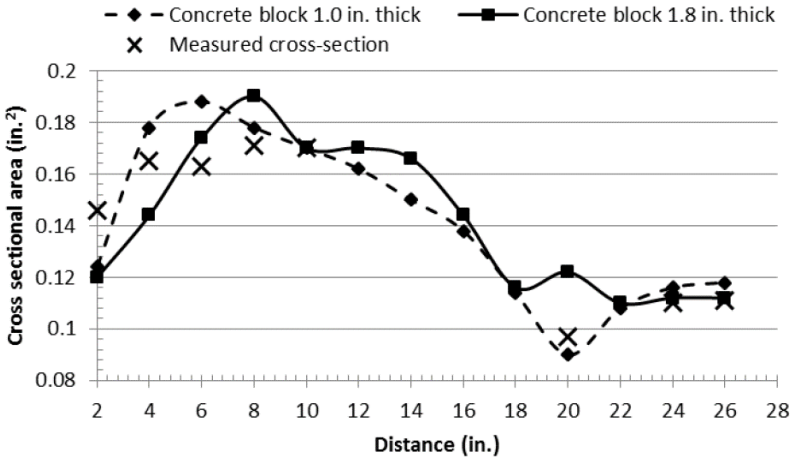

Figure 56. Graph. Estimated cross-sectional areas of the corroded seven-wire strand versus actually measured cross-sectional areas.[27]

Two curves representing variations of remaining cross-sectional areas estimated by the IMFD method using two concrete blocks (1.0 and 1.8 inches thick) overlapped closely with each other in many measurement locations. Furthermore, the degree of agreement between the estimated and actually measured cross-sectional areas was reasonably high.

After the successful development of the IMFD prototype in the laboratory, a field trial of the prototype was conducted to validate the prototype's performance on the soon-to-be-demolished Washington Waterloo Road Bridge in 2010. After the bridge was demolished, the strands were extracted and visually assessed for their effective cross-sectional areas. A commercially available MFL system was also employed for comparison. Figure 57 shows both types of equipment being used under the PSC box beams.

A. IMFD prototype.

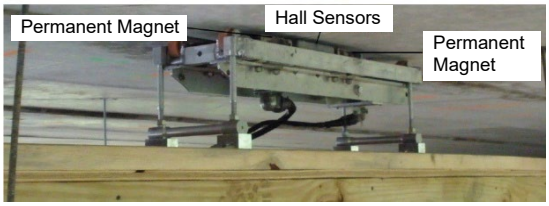

B. MFL equipment.

Figure 57. Photos. Field trial of two NDE systems.[28]

When the field IMFD data and actual section losses were compared, it was apparent that the IMFD method needed to improve accuracy (in the laboratory, it could be accurate within ±7-percent of the cross-sectional area). Even though the researchers had advanced the IMFD method to a level where theoretical ability had been proven, further refinement would be necessary to improve its accuracy of estimating section loss. On the other hand, the MFL system could detect hidden corrosion damage and strand breaks with sufficient accuracy.

The researchers identified the following areas for improvement to obtain accurate readings and upgrade physical features:

- It is necessary to locate the strands as closely as possible, and the distance between the strands and the Hall effect sensors mounted on the electromagnet pole faces should be known accurately.
- It would be desirable to have stronger magnetization, even though it would require a heavier electromagnet.
- It is recommended to use a thermocouple to monitor the temperature and determine the magnet's ultimate strength for specific test scans. This step is recommended because when the sensor system was turned on for a considerable amount of time, the electromagnet's self-heating caused an observed drift in the measured values and variable strength of the electromagnet.
- It is recommended to suspend a good support system under the bridge to enable the IMFD system to move along the length of the box beam in a controlled manner, magnetize the strands, and take measurements. Its heavy weight was a problem in the field when performing a scan under the bridge.

PRINCIPLE OF RFM

When a solenoid-type magnetizer for RFM is placed in the air over a metal object and is energized, a closed magnetic loop is formed around the metal object. Figure 58 illustrates this situation with a hypothetical case of an internal tendon containing the damage.

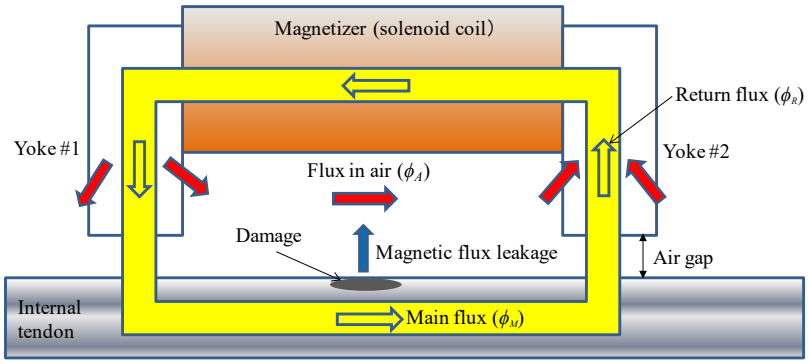

Source: FHWA.

Figure 58. Illustration. Principle of RFM.

The airgap between a pair of yokes and the tendon can be replaced with a clear concrete cover in real PT structures. The magnetic flux passes through yoke number 1, enters the internal tendon via an airgap or concrete as the main flux (ϕ_M), and then returns to yoke number 2 through the other airgap or concrete. A portion of the magnetic flux leaks into the air (ϕ_A), travels in the air, and enters back to yoke number 2. Also, some of the ϕ_M can leak at the tendon damage into the air, and its magnitude depends on the size of the damage. The sum of ϕ_M and ϕ_A constitutes the return flux (ϕ_R). If the gap is very small and ϕ_A is negligible, ϕ_M and ϕ_R become equal.

To compare ϕ_M and ϕ_R as a function of section loss, a small experiment was carried out with four seven-wire strands containing 0-, 25-, 50-, and 75-percent section losses via a fixed airgap of 0.8 inches. Figure 59 shows the results graphically.

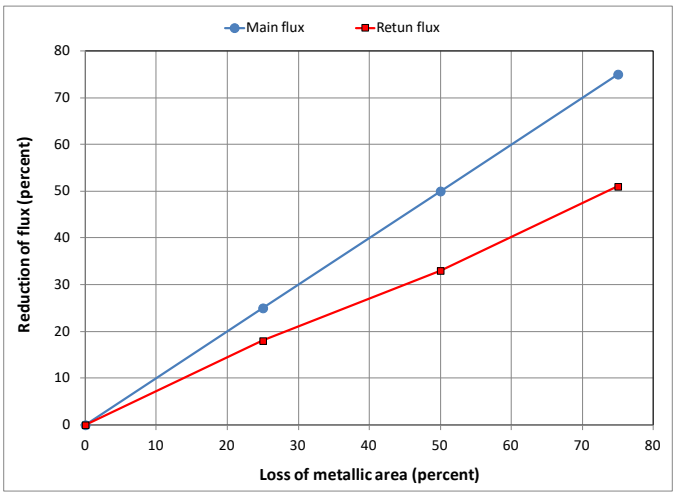

Source: FHWA.

Figure 59. Graph. Relationship between magnetic flux and cross-sectional area.

If section loss increased, reduction of main flux ($\Delta\phi_M$) increased proportionally. A similar proportionality was observed for the reduction of return flux ($\Delta\phi_R$), but a lesser degree, due to increasing amount of air leaked flux ($\Delta\phi_A$). As a result, the difference between $\Delta\phi_M$ and $\Delta\phi_R$ grew proportionally as the section loss increased. Therefore, the size of the corrosion damage affects the accuracy of the RFM at a fixed airgap unless there is a measure to minimize the ϕ_A.

DEVELOPMENT OF RFM PROTOTYPES

TRM was responsible for designing, fabricating, and testing four prototypes during the study. The engineers built two identical units of each prototype: one for the TRM laboratory in Japan and the other for the FHWA NDE laboratory. As the study progressed, the units kept in the FHWA NDE laboratory were constantly updated whenever any changes and improvements were made to the units left in Japan. TRM research staff visited the FHWA NDE laboratory six times to update the prototypes and perform necessary tests during the 21-mo contract period.

Soon after the study began, the first RFM magnetizer prototype was built to determine the optimum configuration of solenoid coils and yokes. The magnetizer had two core configurations: a single coil between two 2-inch-thick rectangular-shaped yokes and two identical solenoid coils in parallel between two 2-inch-thick inverted-Y-shaped yokes. Figure 60 shows the core configurations schematically.

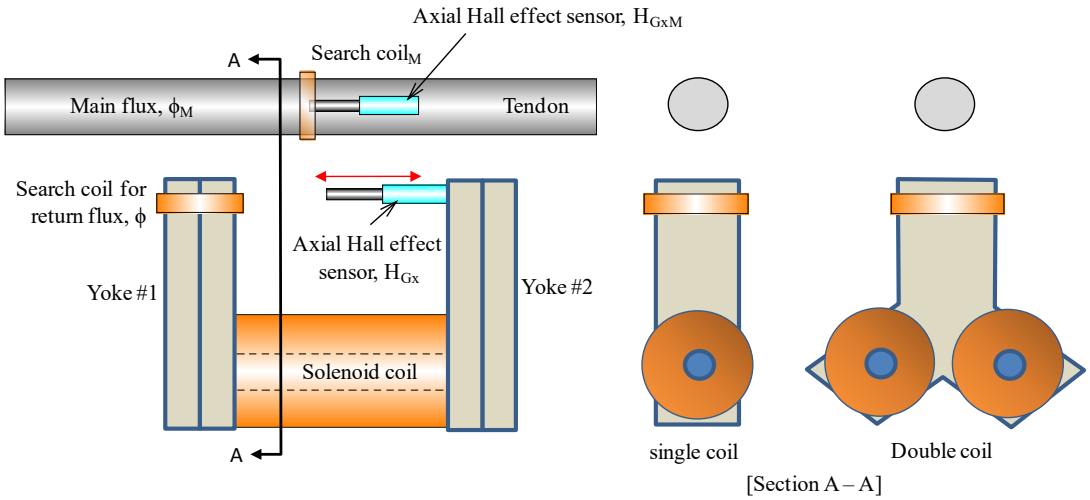

Source: FHWA.

Figure 60. Illustration. Schematic of the first two prototypes.

The prototypes were designed for yoke number 1 to send magnetic flux into a metallic object (tendon) through the air and yoke number 2 to receive magnetic flux through the air. The overall dimensions of the coil were 4.0 inches in diameter and 10.2 inches in length. A search coil was wrapped around the tip of yoke number 1, and an H_{Gx} was mounted on yoke number 2. A search coil (search coil$_M$, where "M" is "main flux") and an H_{Gx} (H_{GxM}) were also installed on the surface of a mockup internal tendon made with a 4-inch plastic pipe containing a varying number of steel strands. Different airgaps between the tips of the yokes and the mockup were tried using 2- by 4-inch wooden pieces. Even though this arrangement was not realistic for an NDE system intended for internal PT tendons, changes in the sensor location, steel mass, and the airgap helped the researchers understand how magnetic flux flew in the noncontact metal object under the given experimental setups.

Preliminary test results obtained with both configurations indicated that most of the magnetic flux bypassed the mockup tendon and transmitted from yoke number 1 to yoke number 2 through the air, irrespective of coil configuration. From these findings, it was concluded that the coil length was too short to minimize magnetic flow through the air.

The second magnetizer prototype was fabricated with a pair of 2.95-inch-thick rectangular-shaped yokes and two 4-inch-diameter solenoid coils in series between the yokes. This configuration elongated the coil length to 20.6 inches to minimize the ϕ_A by increasing resistance in the air between the yokes. A stainless-steel rod was also added between the yokes to mount an H_{Gx} in the middle of the magnetizer. Also, a new H_{Gy} (H_{Gy1}) was added close to the search coil installed on yoke number 1.

Based on the test results obtained with the second prototype, the third prototype was made with the following additional changes:

- The diameter of the solenoid coils was increased to 4.7 inches.
- The second search coil was added to the tip of yoke number 2.

- The third Hall effect sensor (H_{Gy}) for measuring MFL was added in the middle of the magnetizer.

After repeating the experiments on the tendon mockup, the fourth and final magnetizer prototype was developed. The diameter and length of the solenoid coils in series remained the same as the third prototype, that is, 4.7 and 20.6 inches, respectively. Each yoke consisted of three stacked steel plates. The clearance between the bottom of the solenoid coils and the tip of the yoke was 3.3 inches. The weight of the assembled prototype was 218 lb. Figure 61 shows the following individual components and their functionalities schematically:

- Yoke number 1 and yoke number 2 was for incoming and returning magnetic flux, respectively.
- Search coil number 1 on the tip of yoke 1 was to measure return magnetic flux, ϕ_1.
- Search coil number 2 on the tip of yoke 2 was to measure return magnetic flux, ϕ_2.
- H_{Gy} near search coil number 1 was to measure vertical magnetic intensity, H_{Gy1}.
- H_{Gy} near search coil number 2 was to measure vertical magnetic intensity, H_{Gy2}.
- H_{Gy} in the middle of the crossbar was to measure MFL, H_{Gy}.
- An H_{Gx} in the middle of the crossbar was to measure horizontal magnetic intensity, H_{Gx}.
- An encoder distance meter was to measure and record the traveled distance of the magnetizer.

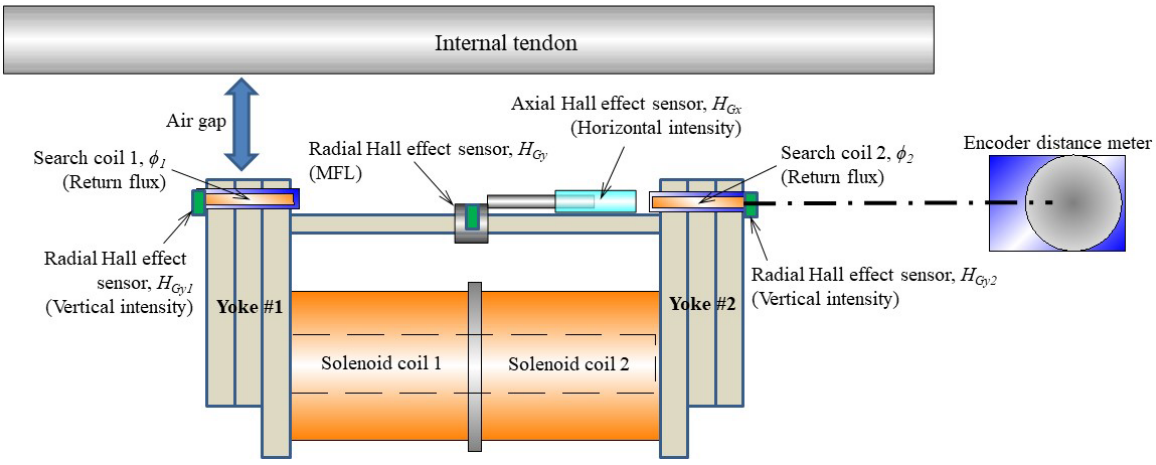

Source: FHWA.

Figure 61. Illustration. Schematic of the fourth prototype and its functionality.

EXPERIMENTAL PROCEDURE

During the development of the prototypes, three specimen types were employed: a laboratory mockup to mimic a web section of a segmental box girder, a real precast box girder segment, and a grouted external tendon specimen. This section describes the experimental work.

Test Specimens

First Laboratory Mockup

A simulated concrete web mockup was designed and built with lumbers and sheets of plywood to avoid interference with the electromagnetic field coming from the magnetizer. Its overall dimensions were 16-ft (length) by 4-ft (height) by 19.0-inches (web width). It was supported by a 16- by 5-ft wooden floor. Six 6-inch heavy-duty wheels were attached under the floor.

The design of the mockup included the following key features of a typical segmental box girder containing internal tendons:

- Two duct materials: metal and plastic.
- A changeable separation (clear cover) between the internal tendons and the magnetizer.
- A slightly draped tendon profile.
- Vertical and horizontal mild rebars.
- A realistic number (18) of 0.6-inch seven-wire strands.
- A real anchorage system, including a wedge plate, a bearing plate, a transition tube, and spiral confinement reinforcement.

Figure 62 shows a bird's-eye view of the mockup with vertical rebars sticking out of the web wall and a magnetizer on a height-adjustable cart, a pair of aluminum guiding rails on the wooden floor, and testing equipment (figure 62-A), an interior view of the mockup (figure 62-B), and the anchorage zone (figure 62-C). Figure 63 shows schematics of the laboratory mockup.

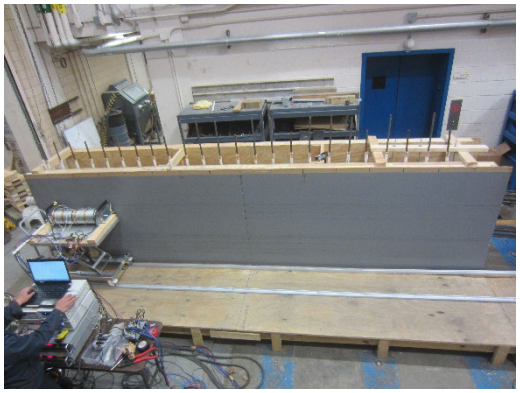

Source: FHWA.

A. Exterior view.

Source: FHWA.

B. Interior view.

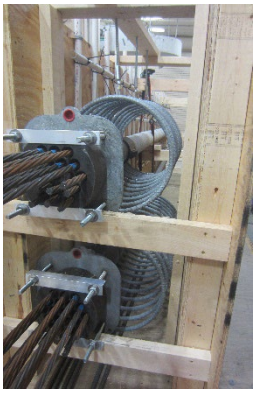

Source: FHWA.

C. Anchorage view.

Figure 62. Photos. First laboratory mockup.

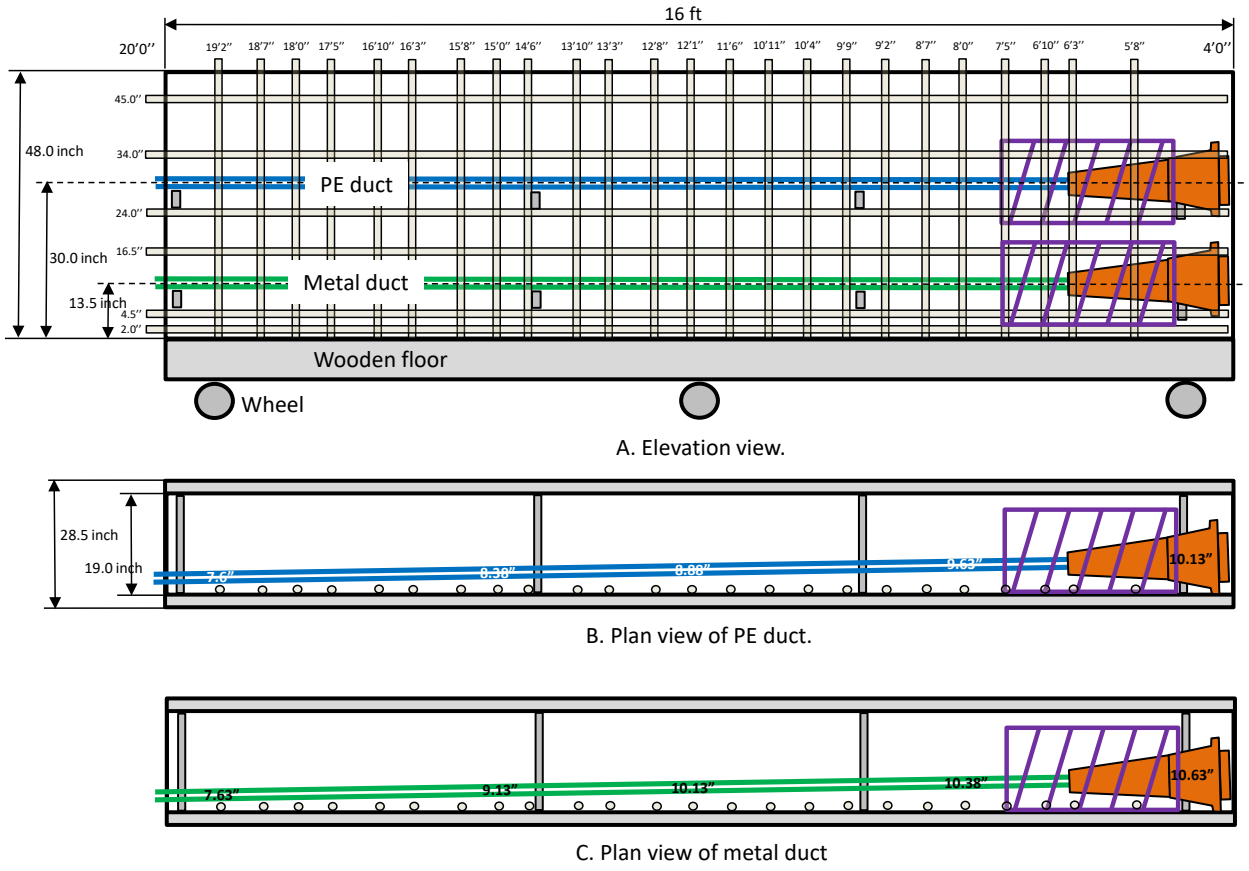

Source: FHWA.

Figure 63. Illustration. Schematics of first laboratory mockup (not to scale).

As shown in figure 62 and figure 63, two internal tendons were installed inside the web. The upper tendon used a 4-inch-diameter corrugated polyethylene (PE) duct, and the lower one used a 3.5-inch-diameter galvanized metal duct. Each tendon was approximately 21-ft long and was rested on four crossbeams. A bulky bearing plate and spiral confinement reinforcement resulted in an increasing distance between the magnetizer and a tendon section in the anchorage zone. Therefore, the distance from the ducts to the vertical wall's exterior face was adjusted by sliding the tendons laterally over the crossbeams. Actual distances at several tendon locations are included in the plan views in figure 63. In addition, the cart heights were fixed at 30.0 inches for the upper tendon and 13.5 inches for the lower tendon to make the centers of the magnetizer's yoke plates and the tendons aligned.

A network of 3/4-inch-diameter PVC pipe was used to add and remove number 5 rebars as vertical and horizontal rebars in the mockup. The PVC pipe network allowed the quick transformation of the rebar configuration during the RFM measurements.

Each mockup tendon contained 18 strands without grout. Seven levels of artificial section loss (27.6-, 18.4-, 16.0-, 12.3-, 9.2-, 6.1-, and 3.1-percent) were introduced in the free length zone to simulate a wide range of corrosion damage encountered in real PT tendons. The same damages

are also introduced in the anchorage zone. Each artificial damage was 6.0 inches long, and the center-to-center distance between two adjacent damage locations was 18 inches.

Second Laboratory Mockup

In 2019, additional laboratory testing was performed at TRM's research center in Tsuchiura, Japan, after two more Hall effect sensors (H_{Gy3}, H_{Gy4}) were added to the latest RFM magnetizer prototype. Figure 64 shows the locations of the added Hall effect sensors.

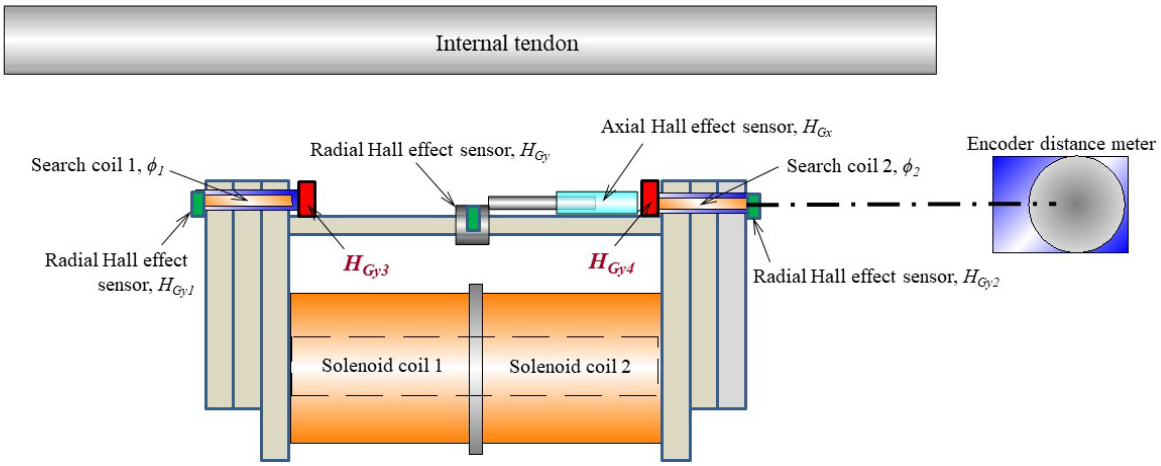

Source: FHWA.

Figure 64. Illustration. Schematic of the modified RFM magnetizer.

The modified magnetizer was evaluated on a second laboratory mockup that simulated a 16-ft-long section of a box girder bridge deck. It was constructed with two 4- by 8-inch sheets of plywood, 20 number 6 transverse rebars, a 3.25-inch galvanized metal duct, supporting plastic blocks and aluminum bars, and three bundles of 0.6-inch-diameter strands. A pair of aluminum rails and an electrical winch allowed the magnetizer to travel straight over the metal duct. An encoder distance meter registered the magnetizer's precise travel distance into the RFM data. Figure 65 shows the schematic of the second laboratory mockup testing.

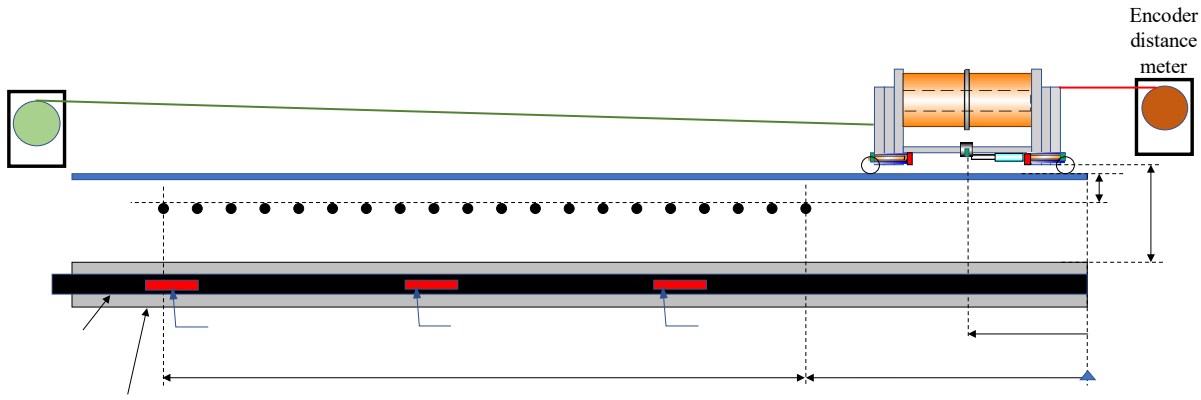

Source: FHWA.

Figure 65. Illustration. Schematic of the second laboratory testing setup.

The following test variables were included:

1. Duct material: galvanized 3.25-inch-diameter metal duct.
2. Number of seven-wire strands in three bundles: 5, 10, 15.
3. Number and spacing of ordinary rebars in the transverse direction (perpendicular to the duct): 20 at 4-inch spacing.
4. Clear cover (airgap) to the transverse rebars: 2.0, 4.0, 6.0 inches.
5. Clear cover from the top of the duct to the bottom of the yokes: 7.0 inches.
6. Clear cover from the top of the strands to the bottom of the yokes: approximately 8.5 inches.
7. Artificial damage level: 6.7-, 10.0-, 20.0-percent section loss.

Three identical artificial damages were introduced by cutting one strand completely in each bundle. Such a damage scheme introduced different damage levels in the strand bundles: 6.7-percent section loss for the 15-strand bundle; 10.0-percent section loss for the 10-strand bundle; and 20.0-percent section loss for the five-strand bundle. In addition, extra measurements were made for 13.3- and 40.0-percent section losses in some cases. The cut length of each damage was 6 inches, and segmented strand pieces were held together with electrical tape. Some of the transverse rebars intersected with the artificial damage. Figure 66 shows photographs of the experimental setup (figure 66-A) and a closeup view of one artificial damage location (figure 66-B).

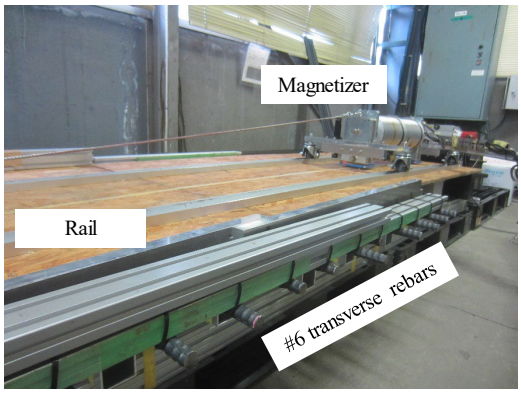

Source: FHWA.

A. RFM testing setup.

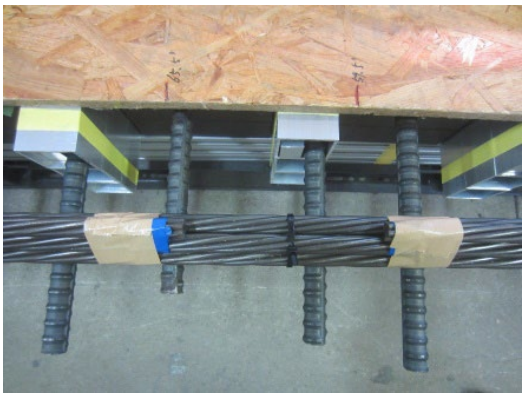
Source: FHWA.

B. Artificial damage.

Figure 66. Photos. Second laboratory mockup.

Once the mockup was constructed, a series of RFM testing was conducted in sequence by changing the rebar cover and the number of the strands/section loss. Final RFM testing was performed without the strands (i.e., the metal duct only).

Grouted Field Tendon Specimen

The tendon C specimen was employed again as a simulated grouted internal tendon. It was placed in the original position of the metal duct after the latter was pushed aside to the other vertical wall. The gap between the specimen's center and the vertical wall's exterior surface was 8.0 inches (clear cover 6.0 inches). Arrows in figure 67 indicate the tendon specimen.

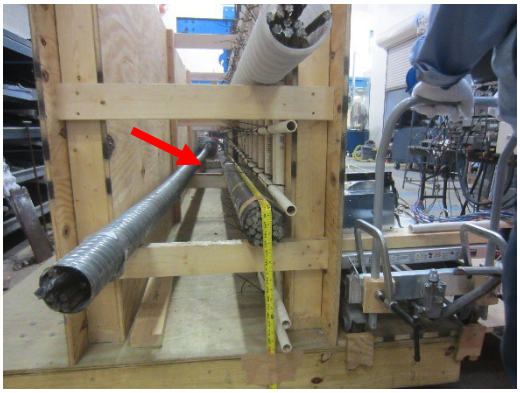
Source: FHWA.

A. End view.

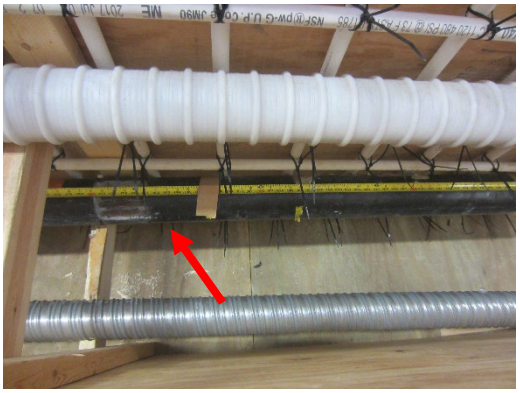
Source: FHWA.

B. Plan view from the top of the mockup.

Figure 67. Photos. Tendon C specimen installed inside the mockup.

The specimen's previously introduced saw cut damages—12-wire cut (9.0-percent section loss), 7-wire cut (5.3-percent section loss), 1-wire cut (0.8-percent section loss), and 1 shallow saw cut (unknown section loss)—were positioned at 32.0 to 35.0, 35.0 to 43.5, 59.0 to 64.0, and

85.5 inches, respectively. The distance was measured from the end of the free length zone. The tendon specimen was scanned first without vertical rebars and then with them at 6-inch spacing.

Precast Concrete Box Girder

After the first round of experiments was completed in the FHWA NDE laboratory, the prototypes were taken to a full-size precast box girder segment stored in the TFHRC's backyard. Initially, all internal tendons were empty. In preparation for the RFM testing, four 3.5-inch internal metal ducts were chosen. The clear concrete cover was 6.0 inches. Each duct was inserted with three to six 0.6-inch seven-wire strands. Each strand bundle received one of four damage levels: no damage (0-percent), minor damage (1-percent section loss), moderate damage (10-percent section loss), and severe damage (30-percent section loss). Figure 68 shows a front view of the box girder specimen (figure 68-A) and damage information (figure 68-B).

Source: FHWA.

A. Front view.

Source: FHWA.

B. Damage information.

Figure 68. Photo and illustration. Precast box girder specimen.

After installing the strands, the ducts were either ungrouted or partially grouted. Artificial grout voids were also introduced in two of four ducts by wrapping strands with different sizes of styrene foam. In addition, several damaged strands were installed in two interior blisters and then filled with grout.

Experimental Setup and Testing

The RFM system requires a more complicated measurement system than the MMFM systems. Figure 69 illustrates an overview of the RFM system components.

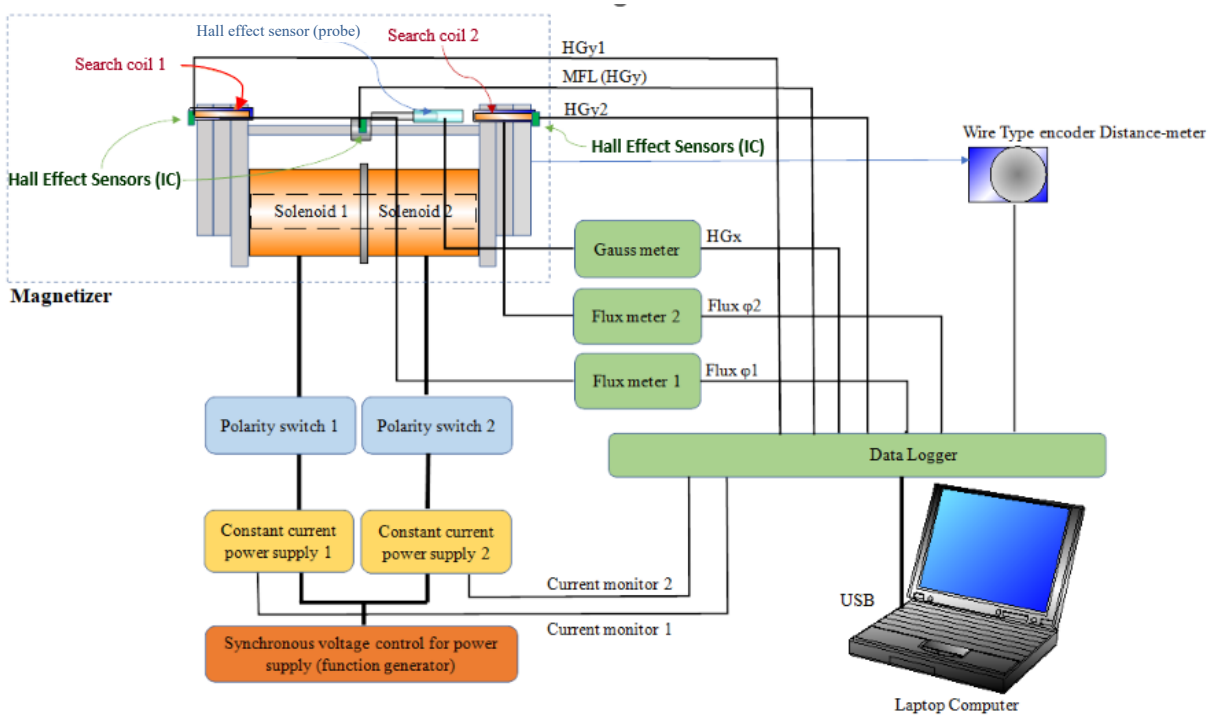

Source: FHWA.

Figure 69. Illustration. Schematic of the RFM system components.

Each solenoid coil had its own power supply and polarity switch. These power supplies were connected to a function generator. Their current monitor outputs were connected to a data logger, and three homemade sensors (H_{Gy}, H_{Gy1}, H_{Gy2}) were connected directly to the data logger. A commercial Hall effect probe (H_{Gx}) and two search coils (ϕ_1, ϕ_2) were also connected to the same data logger through a gauss meter and flux meters, respectively. Then, the data logger was connected to a laptop computer for real-time data collection and subsequent data analysis. The last component of the RFM system was a wire-type encoder distance meter that allowed accurate recording of the magnetizer movement.

At the beginning of the first laboratory mockup testing, researchers investigated the effect of the six horizontal rebars running parallel to the PE and metal ducts. The RFM data obtained with and without the horizontal rebars were not much different. This test result suggested that adding the small mass of the horizontal rebars did not contribute significantly to the original magnetic field. On the other hand, the preliminary test results clearly showed the strong influence of vertical rebars. Based on these results, the first RFM testing was performed without vertical rebars, followed by the second testing after adding vertical rebars at 6-inch spacing. The horizontal rebars were always kept in their positions. For each test condition, two consecutive scans were made to obtain duplicate RFM data.

Figure 70 shows the RFM magnetizer parked at the starting position of the first laboratory mockup before scanning the PE duct (figure 70-A) and a scan measurement in progress near the anchorage zone (figure 70-B).

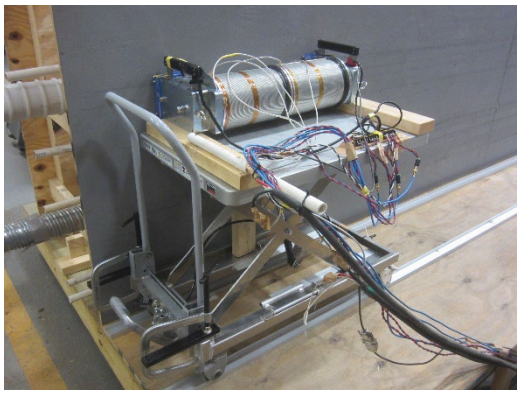

Source: FHWA.

A. Starting position.

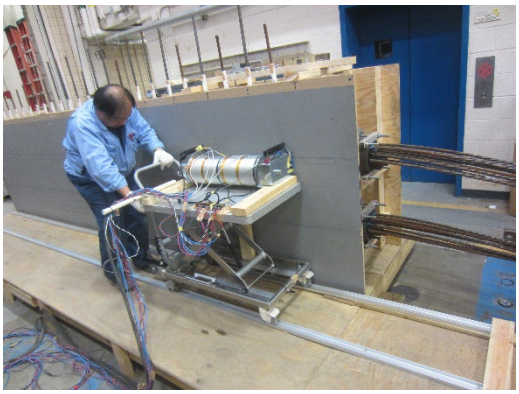

Source: FHWA.

B. Scan measurement in progress.

Figure 70. Photos. RFM testing on the first laboratory mockup.

Figure 71 shows a scan measurement over blister number 1 (figure 71-A) inside the box girder and another scan measurement over an internal duct embedded in the box girder's deck section (figure 71-B).

Source: FHWA.

A. Scanning over blister number 1.

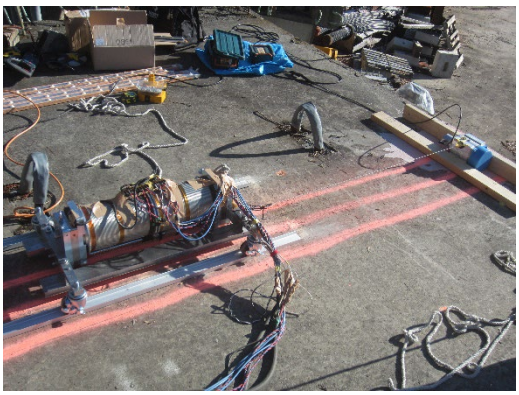

Source: FHWA.

B. Scanning over an internal tendon.

Figure 71. Photos. RFM testing on the box girder specimen.

To scan the ducts smoothly, detachable fittings, such as crossbars and casters, were added to the magnetizer, as shown in figure 71-B. These added fittings increased the magnetizer's weight to 250 lb. The clearance between the bottom of the yokes and the concrete surface was 0.35 inches, including the rail thickness of 0.08 inches.

TEST RESULTS AND DISCUSSION

With four RFM magnetizer prototypes being developed, more than 200 test data were collected over 18 mo. Most of the data were collected primarily for validating the performance of the progressively improved prototypes. Thus, this section presents key findings of the latest RFM data obtained with the final prototype. The RFM data consist of six graphs showing variations of H_{Gx}, MFL, ϕ_1, H_{Gy1}, H_{Gy2}, and ϕ_2 as a function of scan distance.

First Laboratory Mockup

The analysis of the RFM data indicated that four graphs (H_{Gx}, MFL, ϕ_1, and ϕ_2) provided more conspicuous changes than the others (H_{Gy1} and H_{Gy2}) when the RFM detected the damage. The following section discusses some of the representative RFM data obtained from the first laboratory mockup. (Note: whenever damage was detected in the RFM data, a red ellipse was placed at the identified location on the graphs.)

The RFM data from the PE duct and metal duct in the free length zone without vertical rebars are shown in figure 72 and figure 73, respectively.

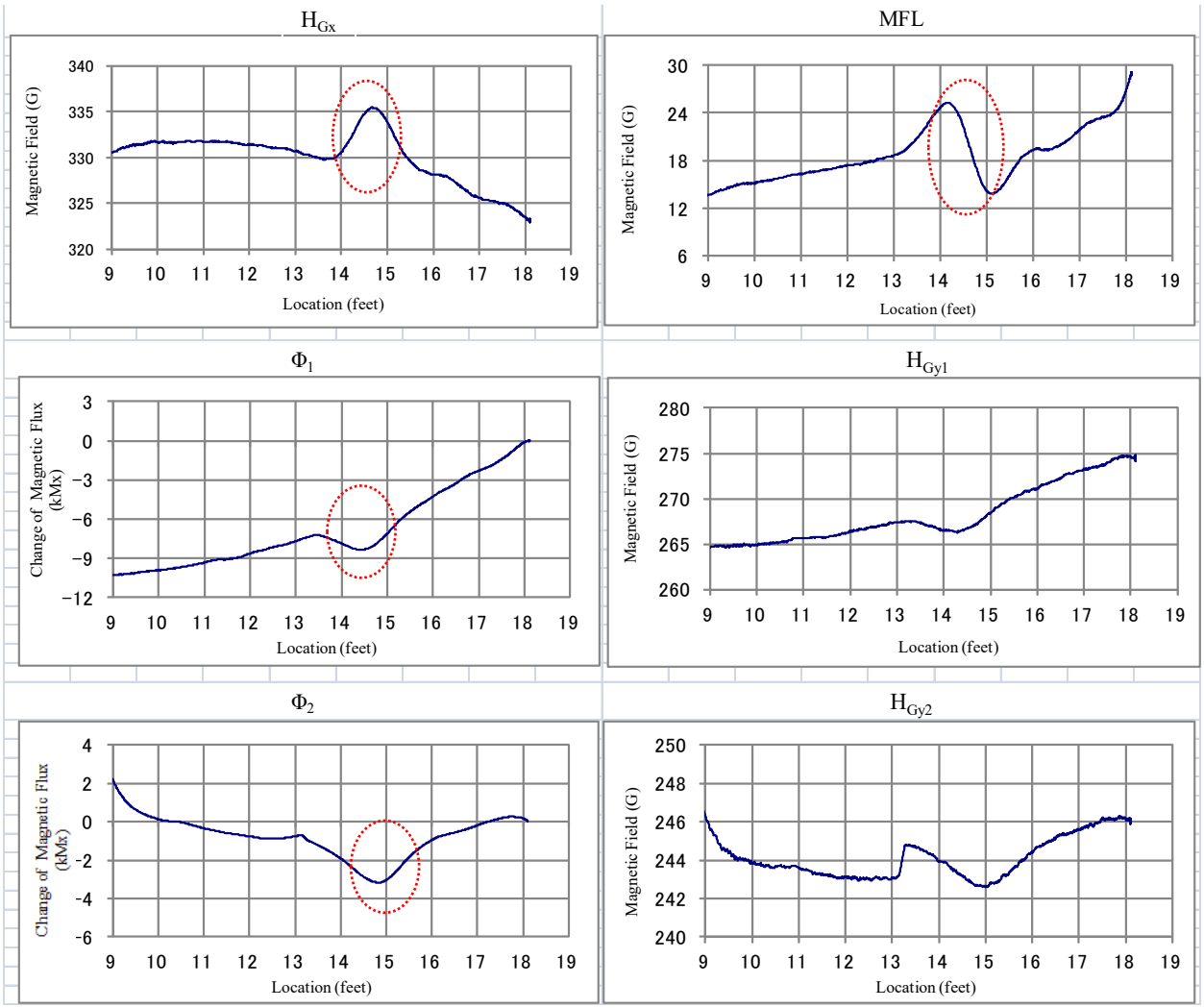

Source: FHWA.

Figure 72. Graphs. RFM data from the PE duct in free length zone with no vertical rebars: 27.6-percent at 14.5-ft was detected.

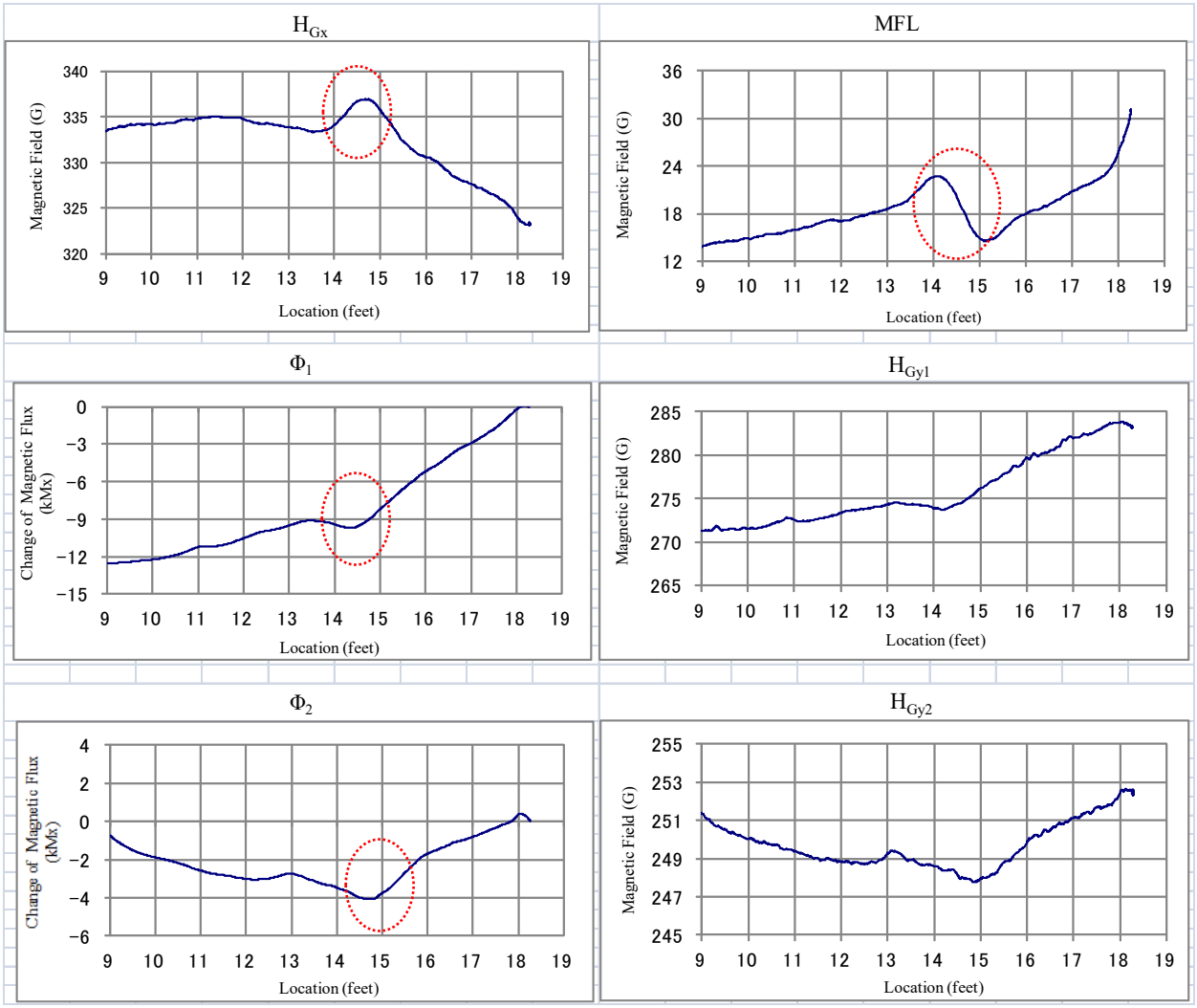

Source: FHWA.

Figure 73. Graphs. RFM data from the metal duct in the free length zone with no vertical rebars: 27.6-percent at 14.5-ft was detected.

Among three damage levels (27.6-percent at 14.5-ft, 6.1-percent at 16.0-ft, and 3.1-percent at 17.5-ft), the largest damage could be detected in both cases. Red ellipses indicate the damage appeared in H_{Gx}, MFL, ϕ_1, and ϕ_2 graphs. Interestingly, there was a lapse of 0.5-ft between ϕ_1 and ϕ_2 due to the separation of yoke number 1 and yoke number 2 to pick up the magnetic flux.

Similar RFM data from the PE duct and metal duct containing four damages (15.3-percent at 14.5-ft, 12.3-percent at 17.5-ft, 6.1-percent at 19.0-ft, and 3.1-percent at 20.5-ft) are shown in figure 74 and figure 75, respectively.

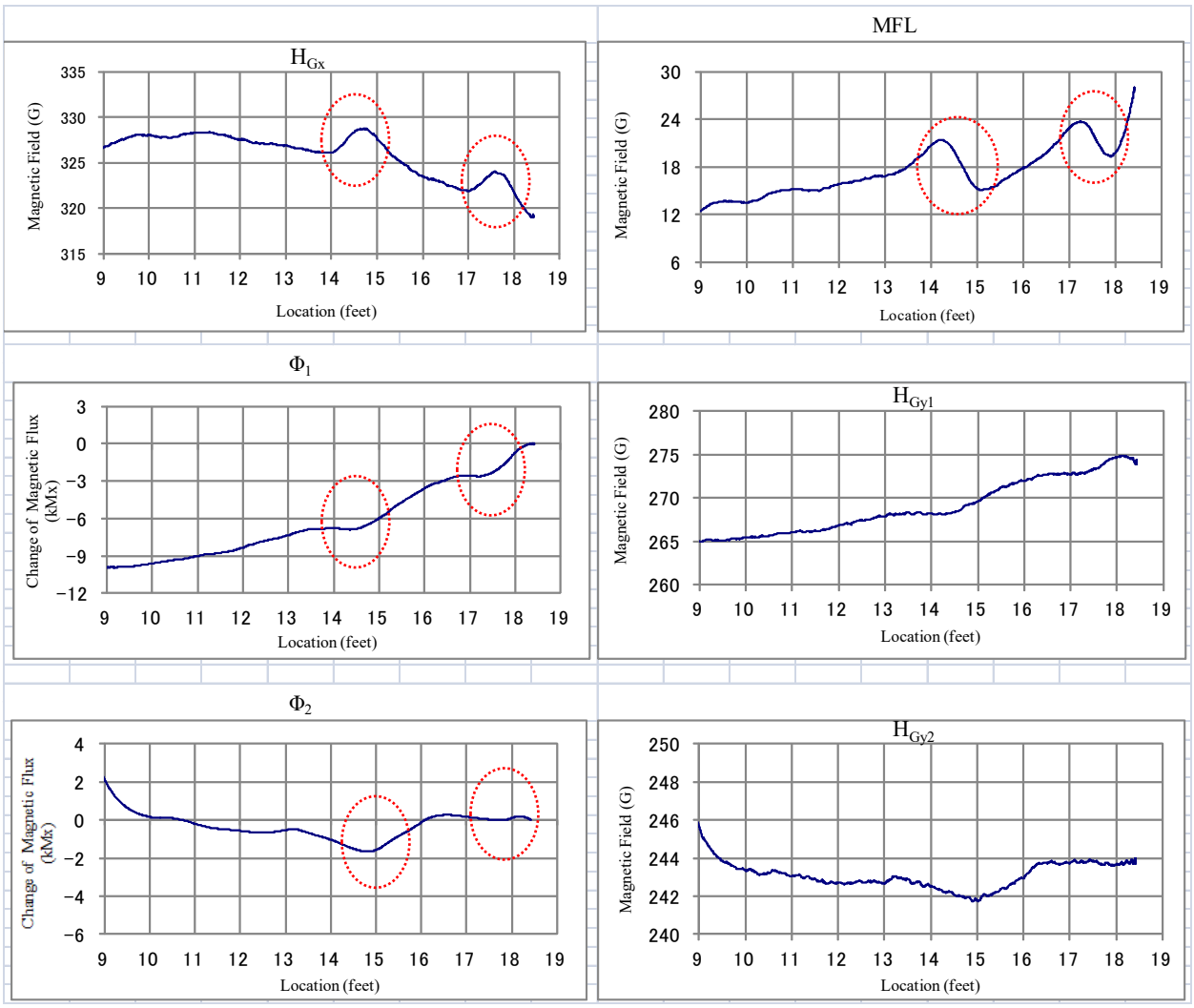

Source: FHWA.

Figure 74. Graphs. RFM data from PE duct in the free length zone with no vertical rebars: 15.3-percent at 14.5-ft and 12.3-percent at 17.5-ft were detected.

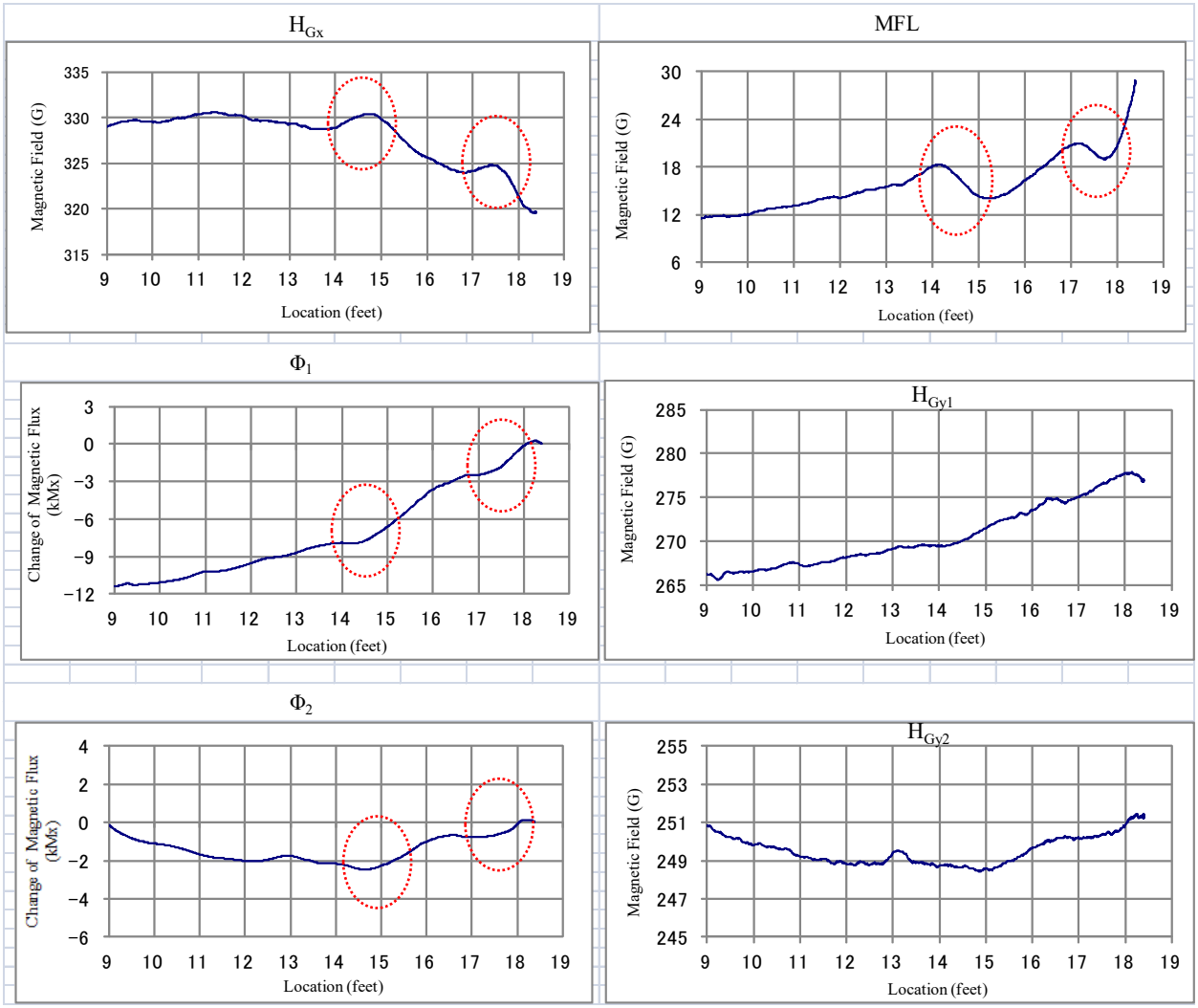

Source: FHWA.

Figure 75. Graphs. RFM data from the metal duct in the free length zone with no vertical rebars: 15.3-percent at 14.5-ft and 12.3-percent at 17.5-ft were detected.

The two largest damage levels (15.3- and 12.3-percent) were detected in both cases, as indicated by red ellipses in the H_{Gx}, MFL, ϕ_1, and ϕ_2 graphs. Again, there was a lapse of 0.5-ft between ϕ_1 and ϕ_2.

After adding vertical rebars at a 6-inch spacing, the follow-up experiments were conducted to see how the RFM data would change. The RFM data of the PE duct and metal duct in the free length zone with vertical rebars containing the same damage levels, such as the one shown in figure 72 and figure 73 (27.6-percent at 14.5-ft, 6.1-percent at 16.0-ft, and 3.1-percent at 17.5-ft), are shown in figure 76 and figure 77, respectively.

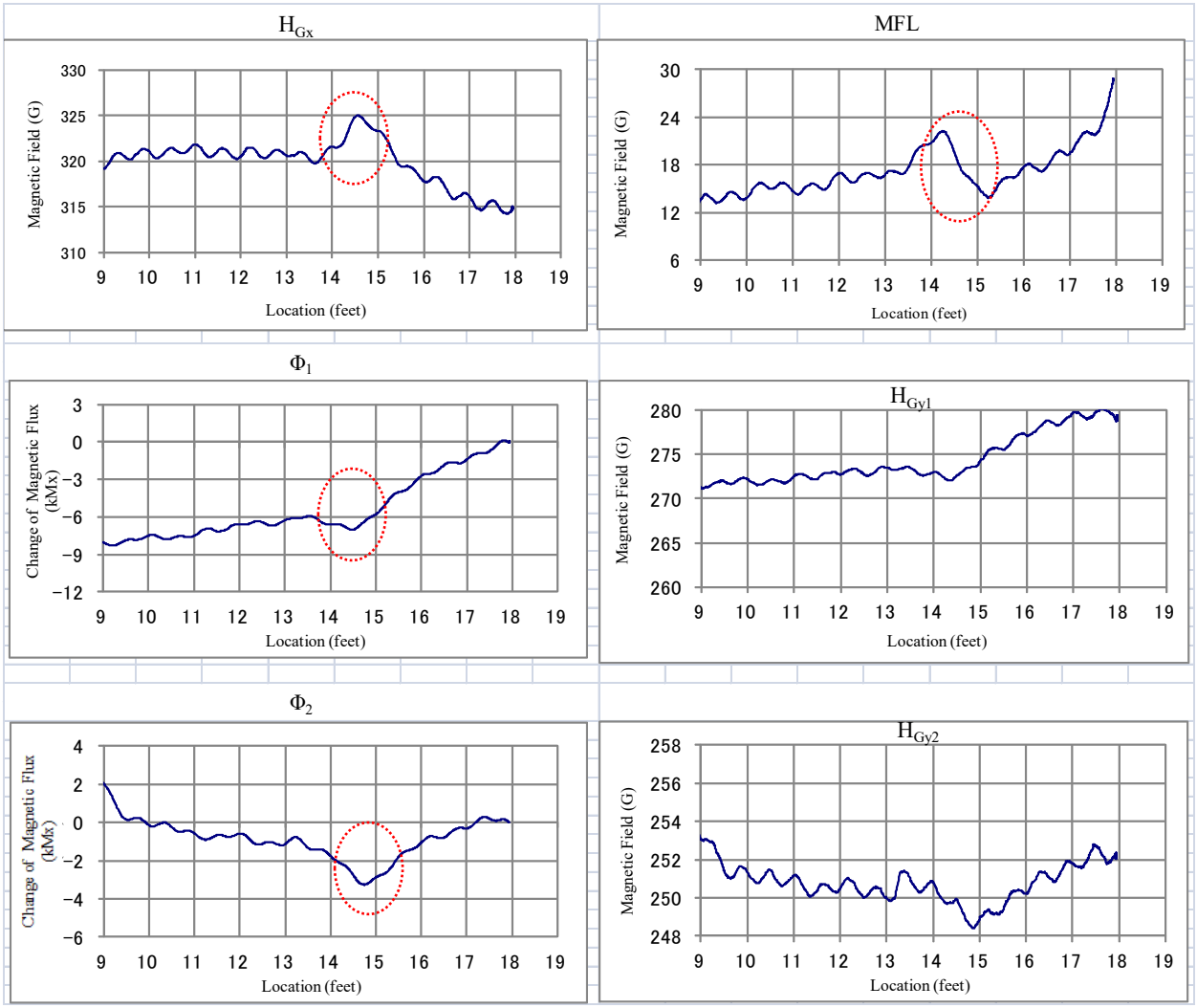

Source: FHWA.

Figure 76. Graphs. RFM data from the PE duct in free length zone with vertical rebars at 6-inch spacing: 27.6-percent damage was detected at 14.5-ft.

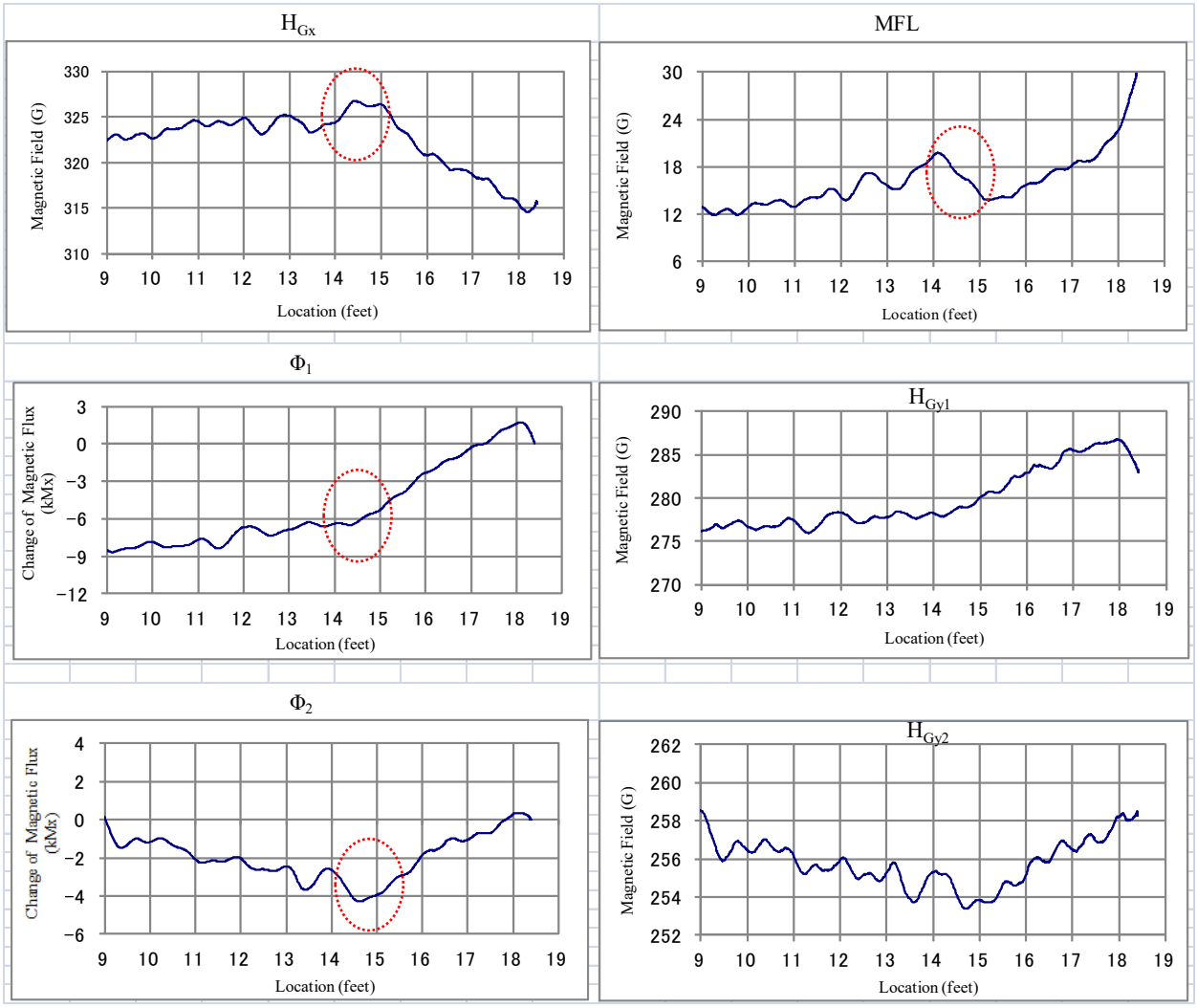

Source: FHWA.

Figure 77. Graphs. RFM data from the metal duct in the free length zone with vertical rebars at 6-inch spacing: 27.6-percent damage was detected at 14.5-ft.

Despite wavy data signals due to electromagnetic interference at each of intersecting vertical rebar locations, the largest damage, 27.6-percent, could still be detected at 14.5-ft in both cases. The distance between ϕ_1 and ϕ_2 was somewhat reduced to less than 0.5-ft in the presence of vertical rebars.

The RFM data from the PE duct and metal duct in the free length zone with vertical rebars containing the same damage levels as the ducts without the rebars shown in figure 74 and figure 75 (15.3-percent at 14.5-ft, 12.3-percent at 17.5-ft, 6.1-percent at 19.0-ft, and 3.1-percent at 20.5-ft) are shown in figure 78 and figure 79, respectively. When the vertical rebars are present, 15.3-percent could still be detected, but missed the lower damage levels (i.e., 12.3-, 6.1-, and 3.1-percent). Although the 12.3-percent section loss was detected in H_{Gx} and MFL graphs, their outputs were small. A distance of approximately 0.5-ft appeared again between ϕ_1 and ϕ_2.

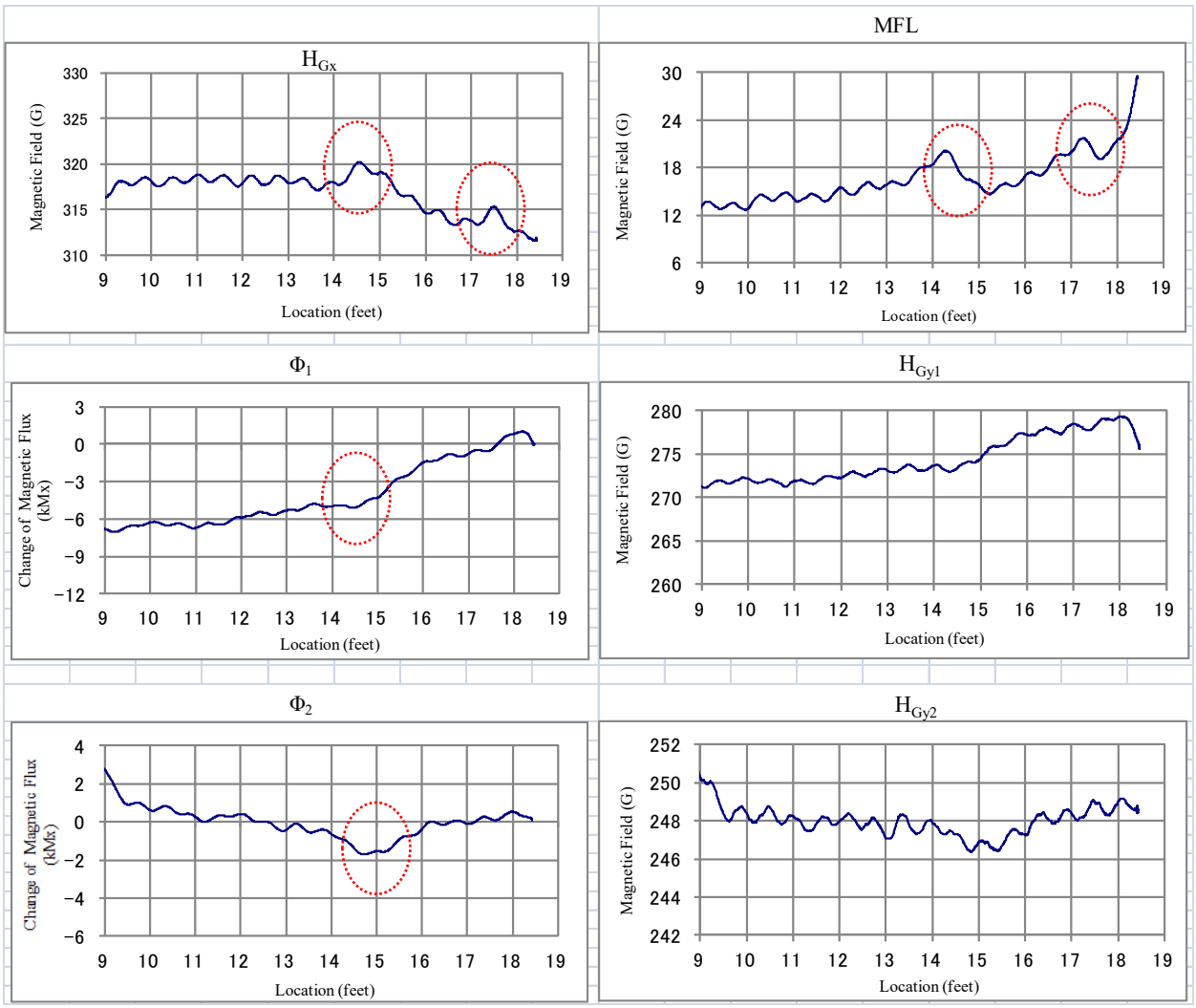

Source: FHWA.

Figure 78. Graphs. RFM data from the PE duct in the free length zone with vertical rebars at 6-inch spacing: 15.3-percent at 14.5-ft was detected.

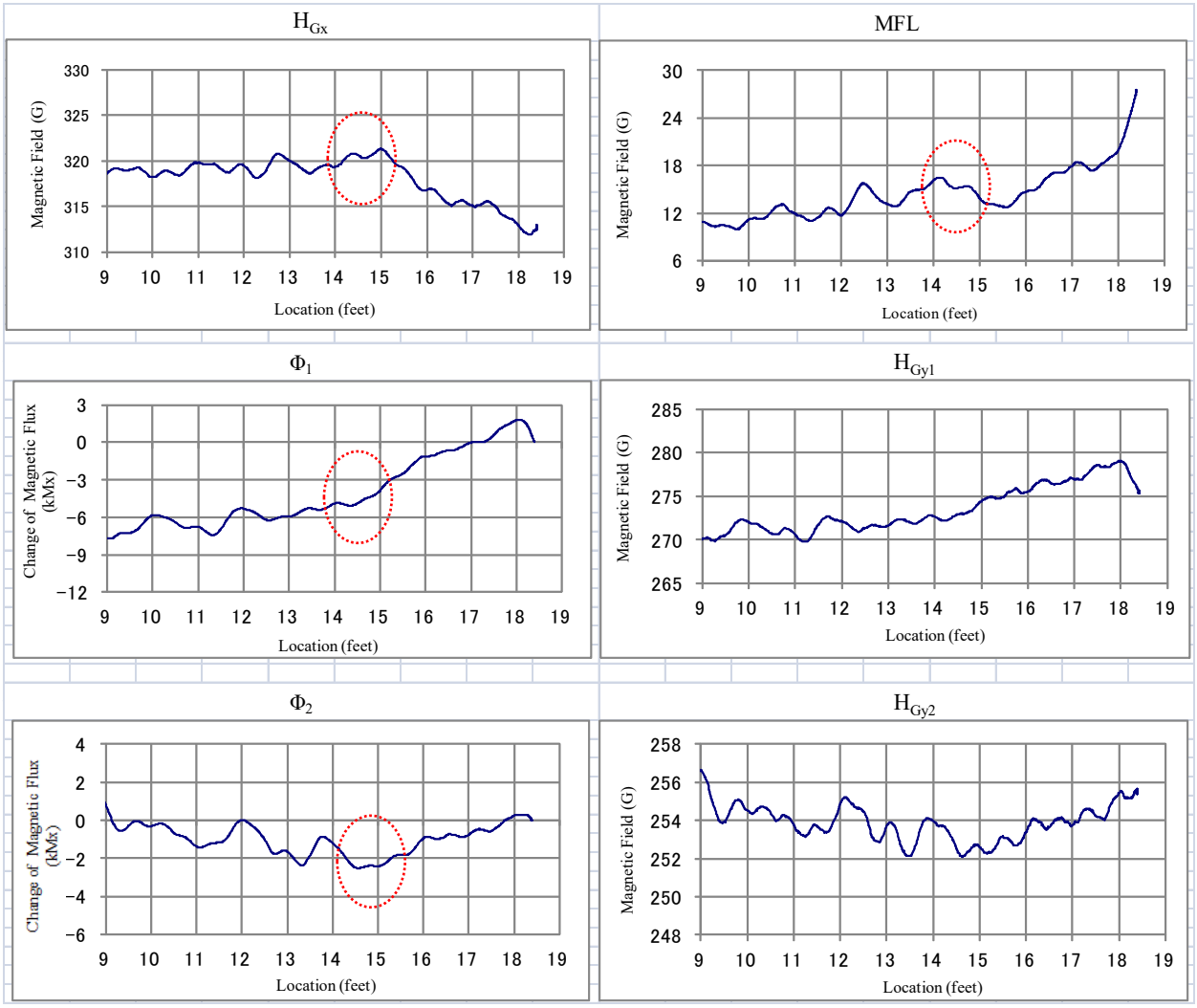

Source: FHWA.

Figure 79. Graphs. RFM data from the metal duct in the free length zone with vertical rebars at 6-inch spacing: 15.3-percent at 14.5-ft was detected.

It was obvious that the presence of vertical rebars affected the RFM data in two ways. The first change was wavy data signals due to electromagnetic interference at each of intersecting vertical rebar locations. The second change was the decreased detection capability, contrary to the insignificant effect of the horizontal rebars.

Figure 80 shows the RFM data from the metal duct in the anchorage zone as having three damage levels with vertical rebars at 6-inch spacing. Although H_{Gx}, ϕ_1, and MFL graphs indicated a possible detection of 27.6-percent section loss at 5.0-ft, it was not conclusive.

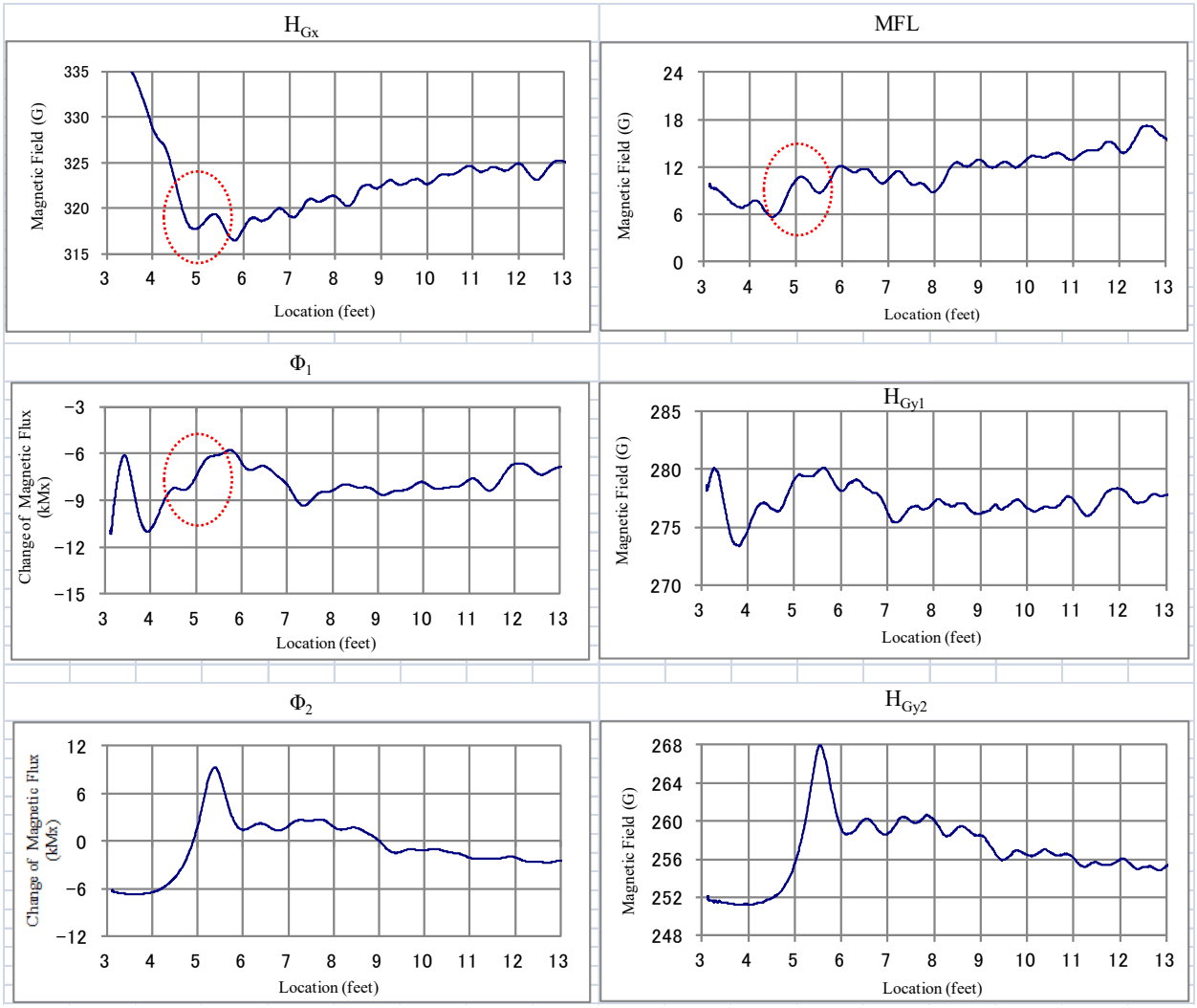

Source: FHWA.

Figure 80. Graphs. RFM data of the metal duct in the anchorage zone with vertical rebars at 6-inch spacing.

The RFM data collected in the anchorage zone could not detect artificial damage, regardless of damage level or adding vertical rebars. This observation was somewhat predicted even before this study began. Consequently, test results pertaining to the anchorage zone are not discussed further in this report.

Second Laboratory Mockup

Figure 81 shows the center magnetic field (H_{Gx}) data of the second mockup without any strands in the duct.

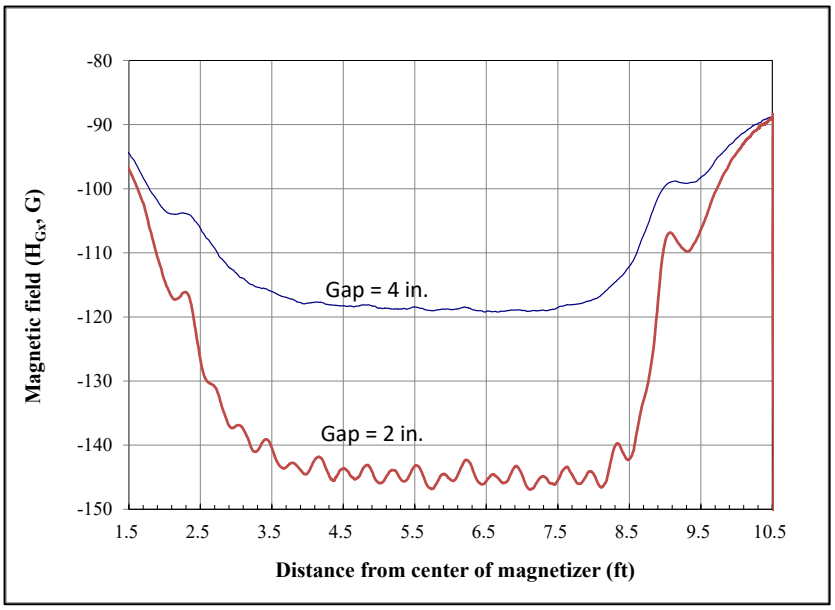

Source: FHWA.

Figure 81. Graph. H_{Gx} graph for the metal duct without any strands under two gaps.

When the metal duct did not contain any strands and the airgap (clear cover) between the transverse rebars and the bottom of the yokes was 2 inches, the presence of the transverse rebars could be seen clearly. As the airgap increased to 4 inches while the other conditions remained the same, the transverse rebars were nearly unrecognizable. Figure 82 shows other H_{Gx} data of the mockup when the five-strand bundle containing three 20-percent section losses was present in the duct. The columns in figure 82 represent the length and location of the damages.

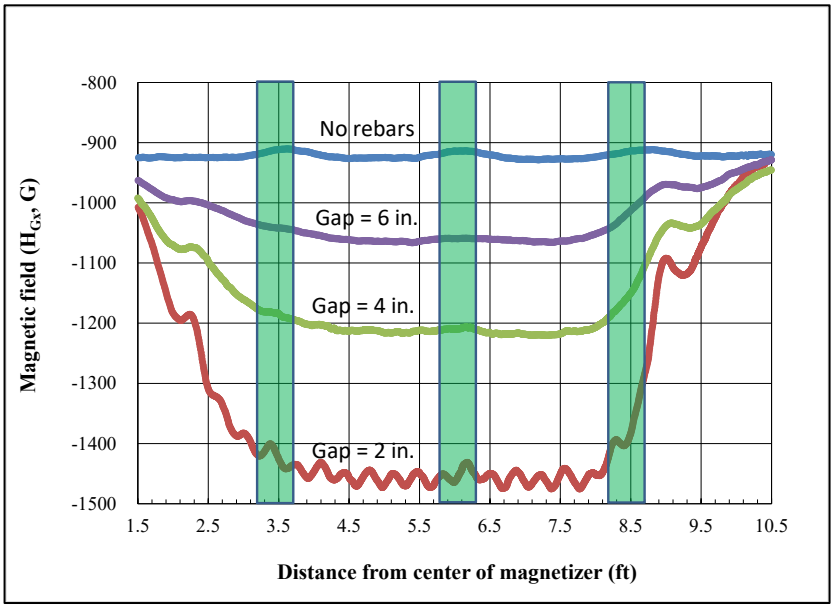

Source: FHWA.

Figure 82. Graph. H_{Gx} graph for the five-strand bundle containing three 20-percent section losses under different rebar covers.

When the transverse rebars were absent, all three 20-percent damages were detected, even though the strands were 8.5 inches beneath the magnetizer. Conversely, when the rebars were present, electromagnetic interference hid some of the damages. This trend was more apparent when the rebars were closer to the magnetizer (smaller gap). As observed in figure 81, the 2-inch gap data showed a clear pattern of the transverse rebar array picked up by the RFM, but the electromagnetic interference created by the transverse rebars obscured the artificial section losses. It was particularly apparent when the rebars were close to the magnetizer (e.g., when the gap was 2 inches) and the damage level was small.

Researchers learned that the change of ϕ_1 measured at the tip of the yoke number 1 and H_{Gx} measured between the yokes were the critical parameters for detecting a section loss. For example, if a section loss exceeding 13-percent was present in the 15-strand bundle, the H_{Gx} could identify it, regardless of the airgap. However, the ϕ_1 could identify the same level of damage only if the airgap exceeded 4 inches.

Figure 83 shows the polynomial regression analysis results of the relationship between the number of strands and airgap for H_{Gx}. The R^2 was nearly 1.0 in every case, indicating a high degree of agreement between the variables.

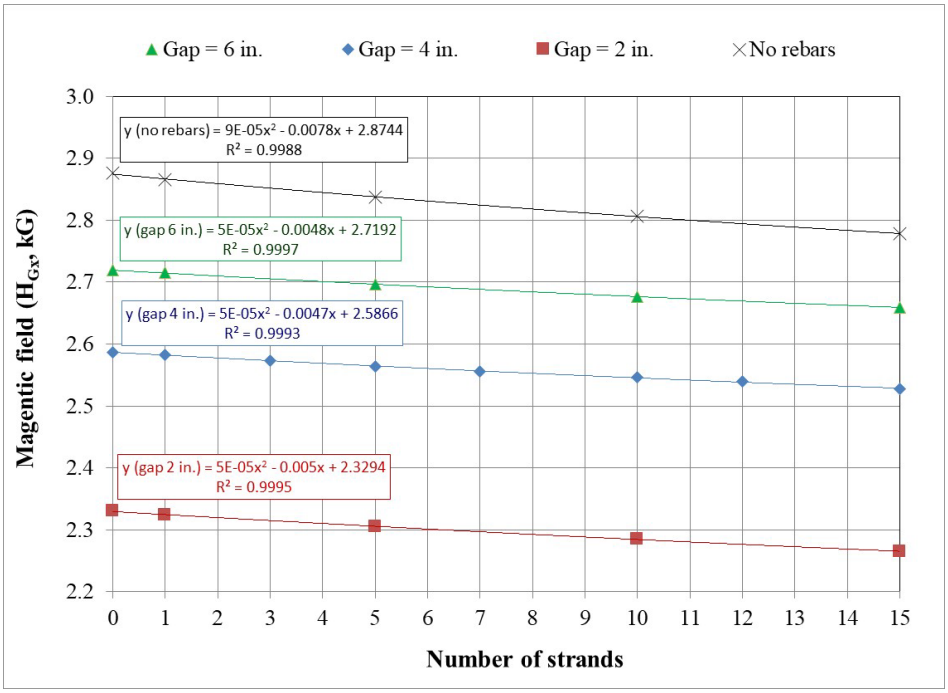

Source: FHWA.

Figure 83. Graph. Polynomial regression analysis results for H_{Gx}.

For the 15-strand case, the most substantial reduction (18.3-percent) of the magnetic field occurred for the 2-inch gap compared with 9.0 percent (4-inch gap) and 4.3-percent (6-inch gap). If the number of strands decreased to 10, these numbers slightly increased to 18.5-percent (2-inch gap), 9.3-percent (4-inch gap), and 4.6-percent (6-inch gap), respectively. These relationships suggested that the magnetic field does not change proportionally to different airgaps.

Grouted Field Tendon Specimen

Figure 84 shows the RFM data from the Varina-Enon Bridge tendon specimen with no vertical rebars. The actual distance from the mockup's exterior wall to the specimen center was 8.0 inches (or a clear cover of 6.0 inches).

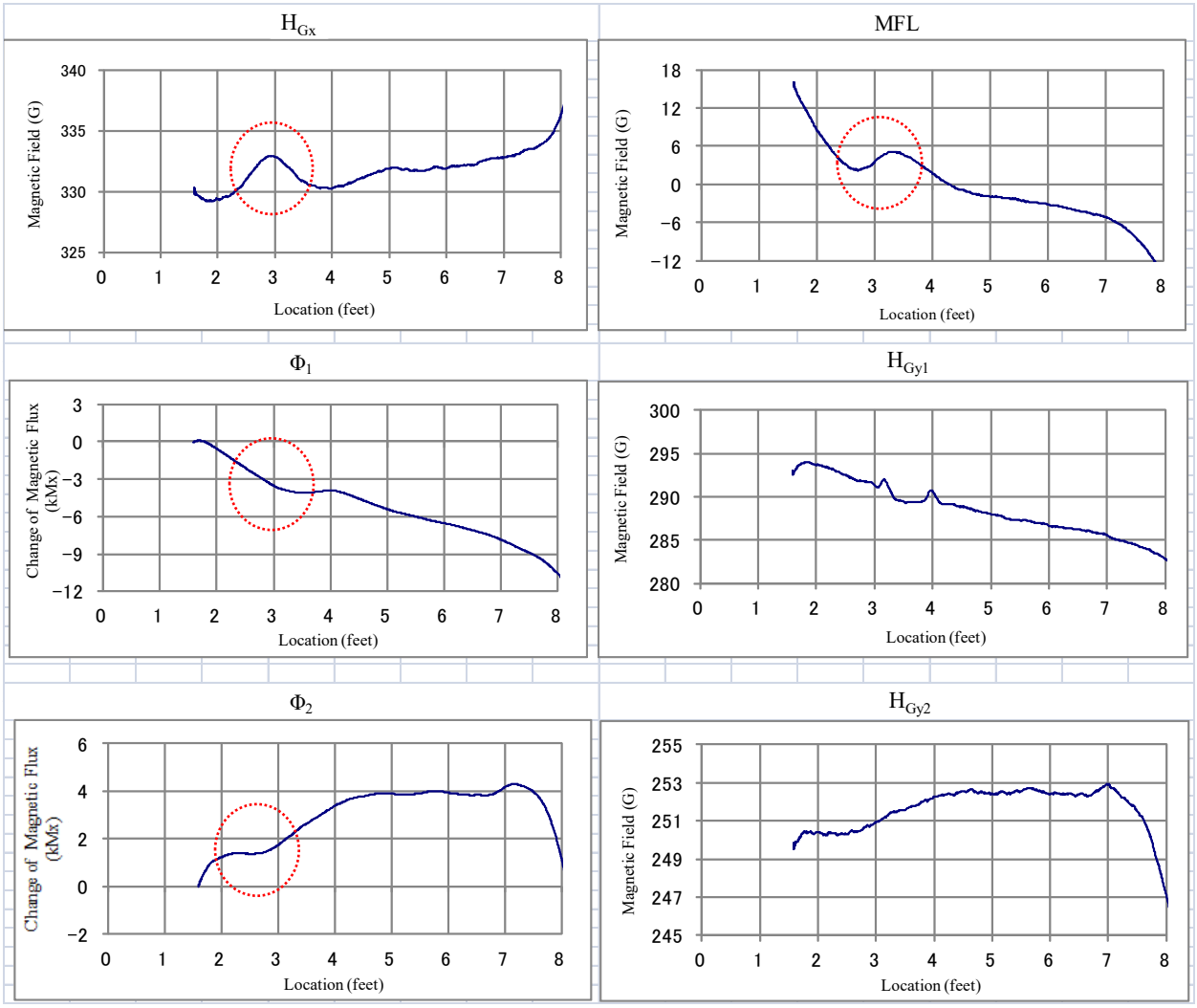

Source: FHWA.

Figure 84. Graphs. RFM data from the Varina-Enon Bridge tendon specimen with no rebars.

The location of a detected section loss is indicated with red ellipses at around 3-ft. This damage corresponded to two adjoining section losses of 5.3- and 9.0-percent if the larger section loss was assumed to dominate the output. The 0.8-percent section loss and saw-cut damage could not be detected.

The RFM data from the same specimen with vertical rebars at 6-inch spacing showed wavy signals compared with those in figure 84 and did not detect all section losses.

Precast Concrete Box Girder

The RFM data did not show any artificial damage hidden in two blisters and four internal ducts of the box girder. Figure 85 shows an example of the poor-quality RFM data, which missed the largest damage of 27.6-percent section loss in duct number 4.

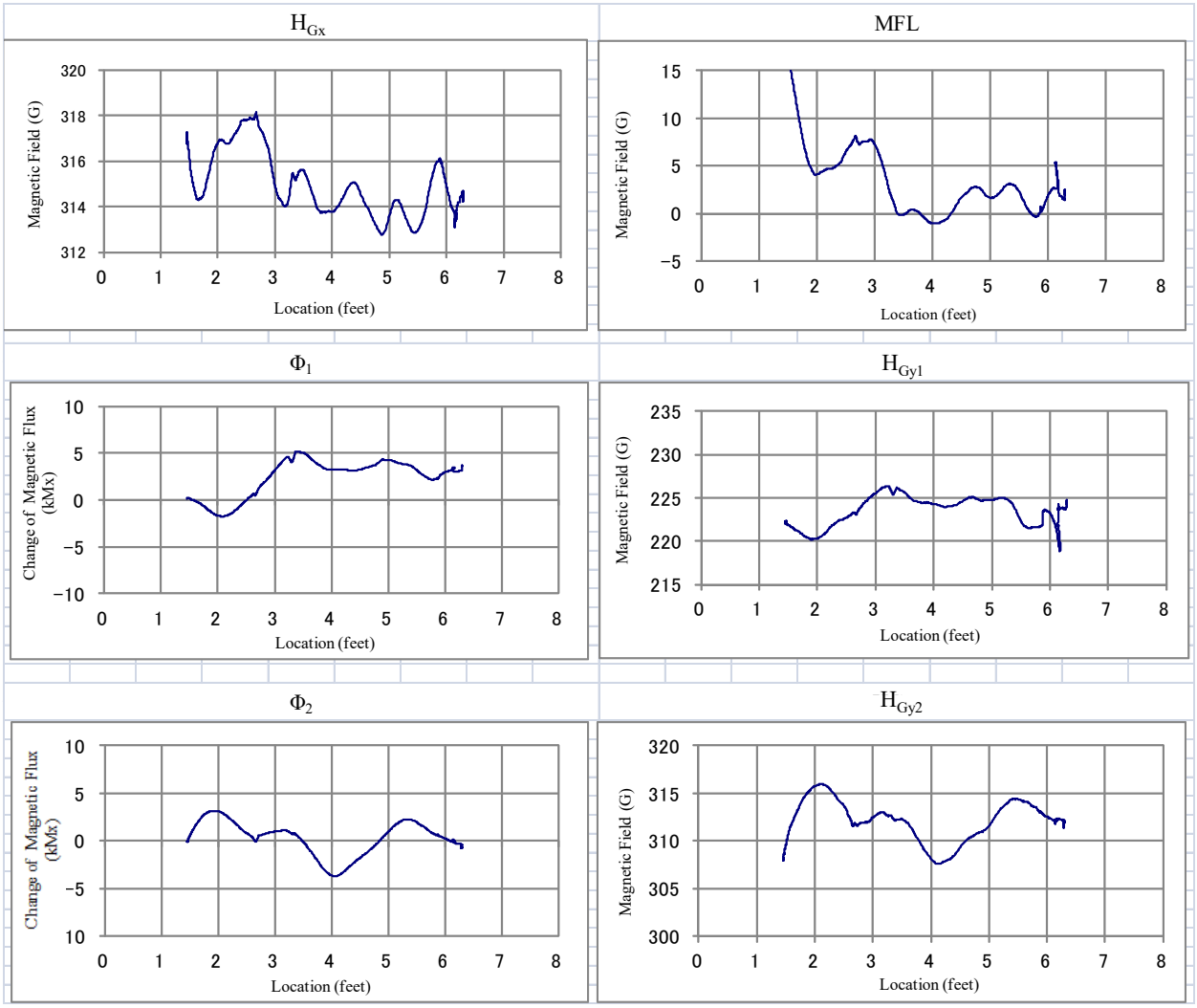

Source: FHWA.

Figure 85. Graphs. RFM data from duct number 4 in the box girder.

There were possible causes of the inability to locate even the largest artificial damage embedded in the precast box girder. The apparent cause was the electromagnetic interference from the ordinary transverse rebars. According to the rebar mapping done with GPR, the blisters also contained many rebars around the concrete surface, and the box girder deck slab contained fifteen number 6 transverse rebars perpendicular to the ducts and eight number 5 longitudinal rebars running parallel to the ducts. Moreover, these identified rebars were not equally spaced. Therefore, some tightly spaced transverse rebars intersecting the ducts must have impeded the damage detection capability of the RFM.

Also, the number of strands (i.e., steel mass) installed in the box girder might have been too small. A small-scale experiment was performed to investigate the effects of the airgap and the number of 0.6-inch seven-wire strands on the RFM data. Figure 86 presents the test results: The RFM parameters (H_{Gx}, MFL, ϕ_1, ϕ_2) were greatly influenced by the airgap between the strands and the magnetizer.

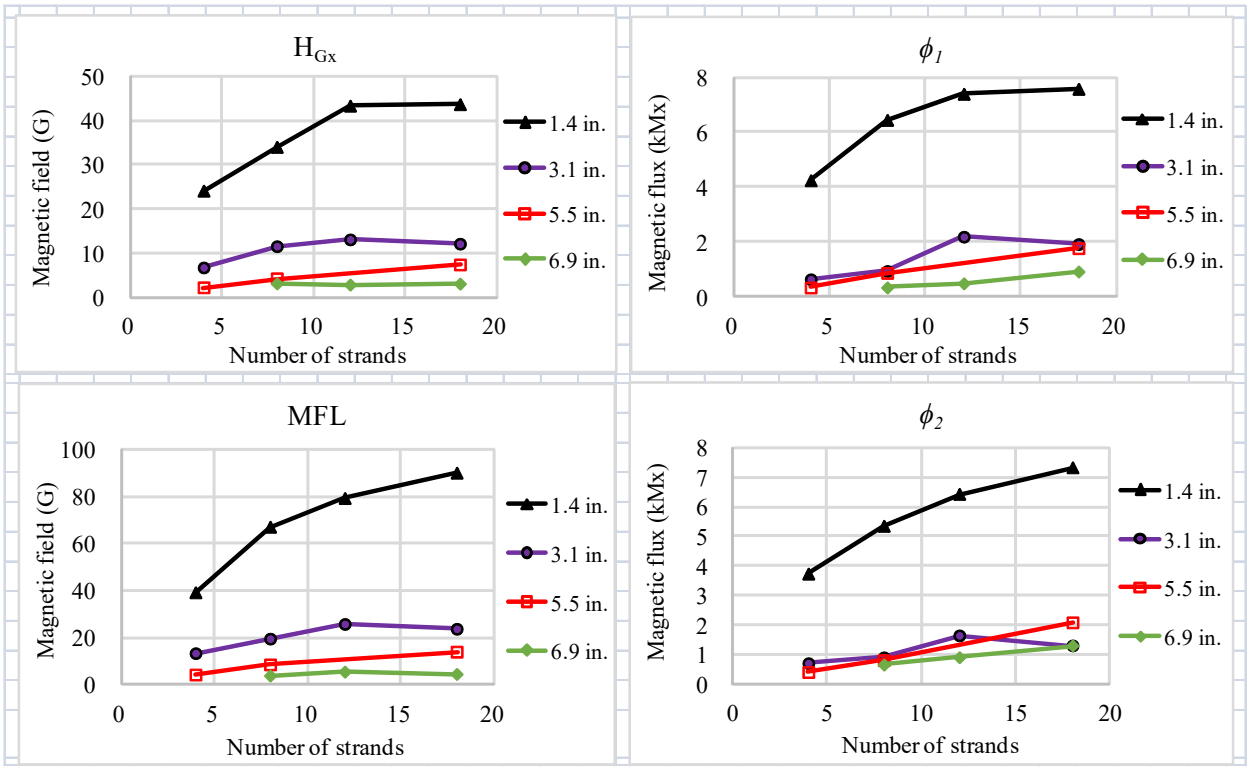

Source: FHWA.

Figure 86. Graphs. Relationship between RFM parameters and number of strands as a function of the airgap.

When the gap exceeded 1.4 inches, the magnetic field and flux decreased significantly, regardless of the number of strands. However, it was still possible to get the identifiable outputs except for one case of the four-strand (the smallest mass) at the largest gap of 6.9 inches. According to the data presented in figure 86, the RFM may require a minimum steel mass equivalent to eight 0.6-inch seven-wire strands and an airgap less than 7.0 inches to be a working NDE system for internal tendons.

In summary, the RFM data from the PE duct and the metal duct were nearly identical under the same testing condition in the free length zone of the first laboratory mockup. Therefore, the same lowest detection limits were set for both duct materials: 9.0-percent section loss without vertical rebars and 15.3-percent section loss with vertical rebars spaced at 6 inches or wider. These limits were valid as long as the clear concrete cover (or airgap) was less than 6.5 inches for the PE duct and 7.5 inches for the metal duct. When similar tests were conducted with 3-inch spaced vertical rebars for the PE duct, only the largest damage level, 27.6-percent, could be identified in the free length zone.

Table 6 and Table 7 summarize the detection capabilities for the first laboratory mockup and Varina-Enon Bridge tendon sample, respectively.

Table 6. Summary of detection capabilities for the first laboratory mockup.

Duct Material	Zone	Vertical Rebar Spacing	27.6% SL	18.4% SL	15.3% SL	12.3% SL	6.1% SL	3.1% SL
PE	Free length	No rebars	Detected	Detected	Detected	Detected	UND	UND
PE	Free length	6 inches	Detected	Detected	Detected	UND	UND	UND
PE	Free length	3 inches	Detected	Not tested	Not tested	Not tested	UND	UND
PE	ANC	No rebars	UNC	UNC	UNC	UND	UND	UND
PE	ANC	6 inches	UND	UND	UND	UND	UND	UND
PE	ANC	3 inches	UND	Not tested	Not tested	Not tested	Not tested	Not tested
Metal	Free length	No rebars	Detected	Detected	Detected	Detected	UND	UND
Metal	Free length	6 inches	Detected	Detected	Detected	UND	UND	UND
Metal	Free length	3 inches	Detected	Not tested	Not tested	Not tested	Not tested	Not tested
Metal	ANC	No rebars	UND	UND	UND	UND	UND	UND
Metal	ANC	6 inches	UNC	UNC	UNC	UND	UND	UND
Metal	ANC	3 inches	UNC	Not tested	Not tested	Not tested	Not tested	Not tested

SL = section loss; ANC = anchorage; UNC = uncertain; UND = undetected.

Table 7. Summary of detection capability for the Varina-Enon Bridge tendon specimen.

Duct Material	Zone	Vertical Rebar Spacing	9.0% SL	0.8% SL	Note
PE	Free length	No rebars	Detected	UND	5.3% SL next to 9.0% SL
PE	Free length	6 inches	UND	UND	—

— No data.
SL = section loss; UND = undetected.

Even though the RFM could not detect damage in the anchorage zone in any of the investigated conditions, the laboratory test results obtained with the final prototype magnetizer in the free length zone should be considered successful compared with the research outcomes from similar previous studies. All the magnetic-based NDE methods that were tried for internal PT tendons are still in an early stage regarding field applicability. Still, available laboratory data supported the hypothesis that the RFM system was superior to the MFL and inductance method (FIU) and IMFM (University of Toledo).

CHAPTER 5. CONCLUSIONS

The solenoid-type MMFM system was the most accurate NDE system for external PT tendons despite the time-consuming preparation work in the field. Considering potential irregularities in the field, the conservative damage detection limits would be 0.4-percent section loss for the point measurement method and 1.0-percent section loss for the scan measurement method.

On the other hand, the permanent type MMFM system was suitable for locating potential problem areas containing more than 3.0-percent section loss in external PT tendons. Ideally, both MMFM systems can be employed in sequence during the field investigations: The permanent magnet type identifies potentially problematic areas by quickly scanning all suspected tendons, followed by the point measurements in the suspicious areas with the solenoid type.

An RFM prototype was developed for the internal tendons. It reached the immediate goal of detecting relatively small section losses hidden in internal tendons in laboratory environments and successfully proved its feasibility. Specifically, the prototype could detect a section loss larger than 15.3-percent in internal mockup tendons surrounded by vertical rebars at 6-inch or wider spacing when the clear concrete cover was less than 7.5 inches for metal ducts and 6.5 inches for PE ducts. Without interference from the vertical rebars, as little as 9.0-percent section loss can be identified under identical testing conditions. When similar tests were conducted with 3-inch spaced vertical rebars for the PE duct, only the largest damage level, 27.6-percent, could be identified in the free length zone. However, poor results were obtained from the anchorage zone of the laboratory mockup and the box girder specimen.

It is recommended that the present RFM prototype be further improved to make it a field-deployable NDE system by reducing the weight and size of the magnetizer. Apart from hardware improvements, new data analysis methodologies should also be developed to identify electromagnetic interference from surrounding rebars.

REFERENCES

1. ACI Committee 222. 2014. *Report on Corrosion of Prestressing Steels*. ACI 222.2R-14. Farmington Hills, MI: American Concrete Institute.

2. Corven, J. A., and Moreton, A. J. 2002. *New Directions for Florida Post-Tensioned Bridges Vol. 1: Post-Tensioning in Florida Bridges*. Tallahassee, FL: Florida Department of Transportation Report, Corven Engineering, Inc.

3. Lee, S.-K. 2022. *Corrosion-Induced Durability Issues and Maintenance Strategies for Post-Tensioned Concrete Bridges*. Report No. FHWA-HRT-22-090. Washington, DC: Federal Highway Administration. https://doi.org/10.21949/1521873, last accessed December 6, 2022.

4. Theryo, T. 2014. "Selected Post-Tensioned Bridges Investigations in the Last 15 Years." Presented at the FHWA/FDOT Grout Meeting. Gainesville, FL: Federal Highway Administration.

5. Florida Department of Transportation. n.d. "Roosevelt Bridge Updates and FAQ" (web page). https://www.fdot.gov/info/roosevelt, last accessed on June 13, 2022.

6. Brenkus, N., G. Tatum, and I. Kreitzer. 2021. *Repair and Maintenance of Post-Tensioned Concrete Bridges*. NCHRP Synthesis Report 562. Washington DC: Transportation Research Board of the National Academies of Sciences, Engineering, and Medicine.

7. Lee, S.-K. 2012. "Bridge Deterioration: Part 2—Bridge Deterioration Caused by Corrosion." *Materials Performance Journal* 51, no. 2: 2–7.

8. Poston, R.W., and J. P. Wouters. 1998. *Durability of Precast Segmental Bridges: Final Report*. Final Report, NCHRP Web Document 15, Project 20-7/Task 92. Washington, DC: National Cooperative Highway Research Program, Transportation Research Board of the National Academies of Sciences, Engineering, and Medicine.

9. FHWA. 2008. "Transportation System Preservation Research, Development, and Implementation Roadmap" (web page). Washington, DC: Federal Highway Administration. https://rosap.ntl.bts.gov/view/dot/36559, last accessed June 9, 2022.

10. Cercone, C., C. Naito, J. Corven, S. Pessiki, W. Keller, and S. Pakzad. 2015. *Designing and Detailing Post-Tensioned Bridges to Accommodate Non-Destructive Evaluation: Subtask 11.1: Literature Review*. ATLSS Report No. 14-01. Bethlehem, PA: Lehigh University Advanced Technology for Large Structural Systems.

11. Corven, J., C. Naito, and S. Pessiki. 2018. *Designing and Detailing Post-Tensioned Bridges to Accommodate Non-Destructive Evaluation*. TechBrief No. FHWA-HIF-18-029. Washington, DC: Federal Highway Administration.

12. Hurlebaus, S., M. B. D. Hueste, M. M. Karthik, and T. Terzioglu. 2017. *Inspection Guidelines for Bridge Post-Tensioning and Stay Cable Systems Using NDE Methods*. NCHRP Research Report 848. Washington, DC: Transportation Research Board of the National Academies of Sciences, Engineering, and Medicine.

13. Florida Department of Transportation Central Structures Office. 2003. *Test and Assessment of NDT Methods for Post-Tensioning Systems in Segmental Balanced Cantilever Concrete Bridges*, Tallahassee, FL: Florida Department of Transportation Central Structures Office.

14. Muszynski, L. C., A. R. Chini, and E. G. Andary. 2003. *Nondestructive Testing Methods to Detect Voids in Bonded Post-Tensioned Ducts*. Washington, DC: Transportation Research Board of the National Academies of Sciences, Engineering, and Medicine.

15. Azizinamini, A. and J. Gull. 2012. *Improved Inspection Techniques for Steel Prestressing/Post-Tensioning Strand: Volume 1*. Tallahassee, FL: Florida Department of Transportation. https://fdotwww.blob.core.windows.net/sitefinity/docs/default-source/research/reports/fdot-bdk80-977-13-rptvol1.pdf, last accessed June 14, 2022.

16. Azizinamini, A. 2017. "Non-Destructive Testing (NDT) of a Segmental Concrete Bridge Scheduled for Demolition, with a Focus on Condition Assessment and Corrosion Detection of Internal Tendons" (web page). https://rosap.ntl.bts.gov/view/dot/32365, last accessed June 9, 2022.

17. Lee, S.-K. 2018. *A Comparative Laboratory Study of Metallic Reinforcing Steels for Corrosion Protection of Reinforced Concrete Bridge Structures*. Report No. FHWA-HRT-15-078. Washington, DC: Federal Highway Administration.

18. Olson Engineering, Inc. n.d. "Sonic Echo/Impulse Response" (web page). https://olsonengineering.com/methods/foundation-depth-integrity-methods/sonic-echo/, last accessed May 16, 2021.

19. Kwun, H. "Back in Style: Magnetostrictive Sensors—Mindful of the Past, SwRI Scientists Find Fitting Solutions to Some of Today's High-Tech Problems." 1991. *Technology Today* Southwest Research Institute, San Antonio, TX.

20. Hillemeier, B., and A. Walther. (unpublished). *The Remanent Magnetization Method (RM Method) Applied to the Localization of Strand Fractures in External PT Tendons*. Consultant report to Federal Highway Administration.

21. J. W. M. Spicer, J. R. Oslander, Y. Chang, and R. Hildebrand. 1995. "Time-Resolved Microwave Thermoreflectometry for Infrastructure Inspection." In: *Progress in Quantitative Nondestructive Evaluation*. Vol. 15. Edited by D. O. Thompson and D. E. Chimenti. New York, NY: Plenum Press. https://dr.lib.iastate.edu/server/api/core/bitstreams/493be843-55b2-4263-937f-b0e33b854453/content, last accessed June 9, 2022.

22. Betti, R., D. Khazem, M. Carlos, R. Gostautas, and Y. P. Virmani. 2014. *Corrosion Monitoring Research for City of New York Bridges*. Report No. FHWA-HRT-14-023. https://www.fhwa.dot.gov/publications/research/infrastructure/structures/bridge/14023/14023.pdf, last accessed May 16, 2021.

23. Sugahara, M. 2010. "Non-Destructive Evaluation of Bridge Cables and Strands Using the Magnetic Main Flux Method (MMFM)." Presented at the 2010 Federal Highway Administration (FHWA) Bridge Engineering Conference: Highways for LIFE and Accelerated Bridge Construction in Orlando, FL.

24. Korea Institute of Construction Technology. 2017. *Tendon Failure Investigation and Follow-up Research Studies*. Seoul, South Korea: Seoul Metropolitan Facilities Management Corp.

25. Rehmat, S., K. Lau, and A. Azizinamini. 2018. *Development of Quality Assurance and Quality Control System for Post Tensioned Segmental Bridges in Florida: Case of Ringling Bridge – Phase II*. Washington, DC: Transportation Research Board of the National Academies of Sciences, Engineering, and Medicine.

26. Fernandes, B. 2010. "Nondestructive Evaluation of Deteriorated Prestressing Strands Using Magnetic Field Induction." Master's thesis. Toledo, Ohio: University of Toledo.

27. Nims, D. K., and V. Devabhaktuni. 2011. *Magnetic Sensor for Nondestructive Evaluation of Deteriorated Prestressing Strand – Phase II*. Toledo, Ohio: University of Toledo University Transportation Center.

28. Titus, M. D. 2011. "Development of Induced Magnetic Field Procedure for Nondestructive Evaluation of Deteriorated Prestressing Strand." Master's thesis. Toledo, OH: University of Toledo.

Recycled
Recyclable

HRDI-20/12-22(WEB)E